Green Synthesized Titanium Dioxide-Based Copper Oxide and Zinc Oxide Nanocomposites for Photocatalytic Degradation of Methylene Blue and Solar Cell/Photoelectrochemical Energy Conversion Applications

Getye Behailu Yitagesu

`

A Dissertation Submitted to the Department of Applied Chemistry, College of Applied Natural Science

School of Graduate Studies

Adama Science and Technology University

March, 2025

Adama, Ethiopia

Green Synthesized Titanium Dioxide-Based Copper Oxide and Zinc Oxide Nanocomposites for Photocatalytic Degradation of Methylene Blue and Solar Cell/Photoelectrochemical Energy Conversion Applications

Getye Behailu Yitagesu

Supervisors

Dr. Getachew Adam, Associate Professor of Physical Chemistry

Dr. Dereje Tsegaye, Associate Professor of Analytical Chemistry

A Dissertation Submitted to the Department of Applied Chemistry, College of Applied Natural Science

Presented in Partial Fulfillment of the Requirement for the Degree of Doctor of Philosophy in Applied Chemistry (Materials Chemistry)

School of Graduate Studies

Adama Science and Technology University

March, 2025

Adama, Ethiopia

Declaration and Recommendation

Declaration

This dissertation, entitled “Green Synthesized Titanium Dioxide-Based Copper Oxide and Zinc Oxide Nanocomposites for Photocatalytic Degradation of Methylene Blue and Solar Cell/Photoelectrochemical Energy Conversion Applications,” is my original work and has not been submitted to any university for a similar purpose. Proper citations duly recognize the references used in this work.

Getye Behailu Yitagesu	_____	_____
Name of Student	Signature	Date

Recommendation

We, the supervisors of this dissertation, hereby certify that we have read and revised the dissertation entitled **"**Green Synthesized Titanium Dioxide-Based Copper Oxide and Zinc Oxide Nanocomposites for Photocatalytic Degradation of Methylene Blue and Solar Cell/Photoelectrochemical Energy Conversion Applications**"** prepared under our guidance by Getye Behailu Yitagesu submitted in partial fulfilment of the requirements for the degree of Doctor of Philosophy in Applied Chemistry (Materials Chemistry). Therefore, we recommend the submission of the dissertation to the Department for further review and defense.

_____	_____	_____
Major Supervisor	Signature	Date
_____	_____	_____
Co-supervisor	Signature	Date

Approval Page

We hereby certify that the recommendations and suggestions made by the Board of Examiners are appropriately incorporated into the final version of the dissertation entitled "Green Synthesized Titanium Dioxide-Based Copper Oxide and Zinc Oxide Nanocomposites for Photocatalytic Degradation of Methylene Blue and Solar Cell/Photoelectrochemical Energy Conversion Applications" by Getye Behailu Yitagesu.

Dr. Getachew Adam		04/15/2025
Major Supervisor	Signature	Date
Dr. Dereje Tsegaye		04/15/2025
Co-supervisor	Signature	Date

We, the undersigned, members of the Board of Examiners of the dissertation open defense by Getye Behailu Yitagesu have read and evaluated the dissertation entitled "Green Synthesized Titanium Dioxide-Based Copper Oxide and Zinc Oxide Nanocomposites for Photocatalytic Degradation of Methylene Blue and Solar Cell/Photoelectrochemical Energy Conversion Applications" and examined the candidate during open defense. This is, therefore, to certify that the dissertation is accepted for partial fulfillment of the degree requirement of Doctor of Philosophy in Applied Chemistry (Materials Chemistry).

Dr Gemechu Deressa		23/04/2025
Chairperson	Signature	Date
Dr. Fedlu Kedir		23/04/2025
Internal Examiner 1	Signature	Date
Bedasa Abdisa, PhD		23/04/2025
Internal Examiner 2	Signature	Date
Prof. Sisay Tadesse		
External Examiner 1	Signature	Date
Dr. Kebede Nigussie		
External Examiner 2	Signature	Date

Finally, approval and acceptance of the dissertation is contingent upon submission of its final copy to the School of Graduate Studies (SGS) through the candidate's Department Graduate Council (DGC) and College Graduate Committee (CGC).

Gemechu Deressa Edossa (PhD) Head, Applied Chemistry Department		23/04/25
Department Head	Signature	Date
ከሮ ጀማል አደም (ዶ/ር) Kero Jemal Adem (PhD)		24/04/2025
College Dean	Signature	Date
School of Graduate Studies, Dean	Signature	Date

ACKNOWLEDGEMENTS

Numerous individuals have participated in completing this research work. First and foremost, I want to sincerely thank my major supervisor, Dr. Getachew Adam, for letting me become his advisee. I appreciate all his help with my study, as well as his patience and inspiration. I would also like to thank him for his friendship and for understanding me all the time. His assistance in scientific advice, psychological treatment, and economic support in purchasing costly materials needed for this work from Germany is much appreciated. Completing this PhD dissertation would not have been possible without his guidance. The past four years have been fantastic, and I consider it an honor to be his student.

Likewise, I thank my Co-supervisor, Dr. Dereje Tsegaye, for his dedicated support. His advice has always been helpful to me in my scientific writing. His deep knowledge, extensive vision, and perceptive remarks helped me develop my insight, enabling me to advance as a researcher. Additionally, I appreciate his friendship, comprehension, and fantastic sense of humor in my scientific research.

I want to acknowledge Adama Science and Technology University for letting me attend all courses and financial support as well as giving me access to all available laboratory facilities. Also, I would like to thank Wachemo University for funding my study and sponsoring the whole coverage of my PhD program.

Also, I would like to sincerely thank Dr. Bedassa Abdissa and Dr. Fedlu Kedir for their critical comments and insightful feedback on my dissertation work. Their rigorous evaluation and constructive criticism, starting from the dissertation proposal, greatly contributed to the overall quality of my work.

I would like to extend my heartfelt gratitude to Dr. Buzuayehu Abebe for his invaluable support and discerning comments regarding my dissertation. His meticulous attention to detail and constructive feedback enhanced the quality of my work. I truly appreciate the time and effort he dedicated to reviewing my findings and his encouragement throughout the process.

I want to express my sincere appreciation to Dr. Zinabu Gashaw for his invaluable assistance in editing my document and providing support with the software used throughout

my research. I appreciate the time and effort he devoted to helping me, which has been crucial in bringing this dissertation to completion.

I would like to extend my sincere thanks to Mr. Demeke Tesfaye for his support and assistance with the XRD, photocatalytic, and UV-Vis measurements during my study. His guidance was invaluable to my research, and I appreciate the time and effort he dedicated to helping me.

I would like to extend my sincere thanks to Dr. Gemechu Deressa for his positive and fast response when I needed his support. Thanks for his commitment and leadership in the department.

I want to extend my heartfelt thanks to Guta Amenu, Lemi Bulto, and Bontu Guta for their invaluable support in my laboratory work. Their dedication has significantly contributed to my success.

I wanted to take a moment to express my warm gratitude to Desta Makebo for his invaluable support in the characterization of my samples. He has significantly contributed to the success of my work.

I would like to express my sincere gratitude to Mekrelawit Wosen for her efforts in the preliminary tests and sample collection. Her hard work and dedication have been essential to my progress, and I truly appreciate everything she has done.

Finally, from the bottom of my heart, I would like to thank my parents for their unfailing support and continuous encouragement throughout my journey.

Table of Contents

List of Figures

List of Tables

Abbreviations and Symbols

ADEKA-1	carbazole/hexyl-functionalized oligothiophene/trimethoxysilyl-anchor dye
AM	Air mass
a-Si	amorphous silicon
BET	Brunauer-Emmett-Teller
BL	Blocking layer
BJH	Barrett-Joyner-Halenda
CPV	Concentrating photovoltaic
CB	Conduction band
CIGS	Copper Indium Gallium Selenide
CE	Counter electrode
DRS	Diffused reflectance spectroscopy
DSSC	Dye-sensitized solar cell
EDX	Energy dispersive X-ray spectroscopy
EIS	Electrochemical impedance spectroscopy
FF	Fill factor
FTIR	Fourier transform infrared
FTO	Fluorine-doped tin oxide
FWHM	Full-width at half-maximum intensity
HOMO	Highest occupied molecular orbital
HTM	Hole transferring material
IHF	*Impatiens rothii Hook.f.* flower
IHR	*Impatiens rothii Hook.f.* root
IL	Ionic Liquids
ITO	Indium-doped tin oxide
λmax	Wavelength of maximum light absorption
LUMO	Lowest unoccupied molecular orbital
MB	Methylene blue
NCs	Nanocomposites
NMs	Nanomaterials

NPs	Nanoparticles
V_{OC}	Open circuit voltage
P_{max}	Maximum power output
PV	Photovoltaics
PSC	Polymer solar cell
QD	Quantum dot
RES	Renewable energy source
RSF	*Rumex nepalensis Spreng Flower*
SEM	Scanning Electron Microscopy
TGA	Thermogravimetric analysis
HRTEM	High-resolution transmission electron microscope
TEM	Transmission electron microscopy
TCO	Transparent conductive oxides
TMO	Transition metal oxide
T/R	Transparent/Reflective paste
TRF	*Thymus schimperi Ronniger flower*
TTIP	Titanium tetra isopropoxide
VB	Valance band

Abstract

Global energy and clean water consumption is increasing with population growth and technological advancement, which has resulted in serious concerns about scarcity. DSSC energy conversion and photocatalytic water purification have emerged as the most promising methods to address these issues. This work utilized natural dyes from economical and ecologically friendly plant extracts of Impatiens rothii Hook.f. flower (IHF), Impatiens rothii Hook.f. root (IHR), Thymus schimperi Ronniger flower *(TRF), and Rumex nepalensis Spreng* Flower *(RSF). Here, pristine TiO_2, TiO_2/CuO NCs, and TiO_2/ZnO NCs were effectively prepared by a green method using Impatiens rothii Hook f. leaf (IHL) extract as a reducing and capping agent. The average crystallite size and particle size from XRD and TEM analysis were 11, 14, 13 nm and 27, 23, and 21 nm for TiO_2 NPs, TiO_2/CuO, and TiO_2/ZnO NCs, respectively. XPS analysis showed the formation of TiO_2, CuO, and ZnO. Based on BET analysis, the specific surface areas were determined to be 65, 94, and 91 m^2/g for TiO_2 NPs, TiO_2/CuO, and TiO_2/ZnO NCs, respectively. PL analysis showed that TiO_2/CuO NCs have the lowest electron-hole recombination rate. The UV-vis-DRS showed the presence of a redshift for TiO_2/CuO (2.91 eV) and TiO_2/ZnO (2.98 eV) NCs, compared to the TiO_2 NPs (3.39 eV). SEM morphological study revealed that all the synthesized nanostructures have spherical shapes. The results of lattice fringes from HRTEM analysis supported the XRD crystal analysis results. MB dye degradation optimized parameters were catalyst dosage (20 mg/L), initial MB dye concentration (15 ppm), pH of the solution (9), and contact time of 80 min. The maximum photodegradation of 99% was obtained at the optimized conditions in the presence of TiO_2/CuO NCs. The scavenger test showed that the reactive radicals* $OH^{\bullet}$, $O_2^{\bullet-}$, and h^+ for *TiO_2 NPs, TiO_2/CuO (1:1) NCs, and TiO_2/ZnO (1:1) NCs, respectively, play important roles in the photodegradation of MB. The reusability test of photocatalysts showed good performance in three cycles with degradation efficiencies of 71%, 95%, and 89% for pristine TiO_2, TiO_2/CuO (1:1) NCs, and TiO_2/ZnO (1:1) NCs, respectively, at the third cycle. The photovoltaic parameters such as J_{sc}, V_{oc}, FF, and overall conversion efficiencies for the fabricated DSSCs were evaluated. Among the synthesized photoanodes and plant-extracted dyes, the one fabricated with TiO_2/CuO (1:1) NCs and IHR (mix) exhibited the highest power conversion efficiency of 1.70%. The IPCE of this device was found to be 56.71 % at its absorption maxima and showed the best stability compared to other synthesized nanomaterials.*

Keywords*: Green synthesis, transition of metal oxide nanomaterials, photocatalysis, natural dyes, DSSC.*

1 INTRODUCTION

1.1 Background of the Study

Energy and environmental issues are quickly rising to the global agenda. An increase in socioeconomic demand is related to the massive ecological repercussions of industrialization, including water contamination, climate change, and the loss of natural resources. The unregulated release of numerous hazardous materials, such as liquid, semi-solid, and solid wastes, is seriously polluting the planet (Al-Musawi *et al.*, 2022; Pavel *et al.*, 2023). Pollutants that can seep into aquatic systems include organic dyes (Ghazy et al., 2022). The rising demand for modern technologies has resulted in a number of contaminants, including these hazardous organic dyes, contaminating water (Alamier et al., 2023). Several studies have connected the ingestion of organic dyes to a number of health issues in humans, such as gastritis, vomiting, chest pain, irregular pulse, and excessive perspiration (Das et al., 2023; Ikram et al., 2023; Ismail et al., 2019; Martins et al., 2022; Vieira et al., 2021).

Many of the cationic dyes are used in the dyeing industry, especially for the dyeing of textiles such as cotton, wool, silk, and paper. Even though they are used extensively, cationic dyes negatively impact the environment more than neutral and anionic dyes. Their exceptionally high tinctorial value has a substantial effect on the visual worth of aquatic ecosystems (Salleh *et al.*, 2011; Tripathi, 2013). Moreover, their cationic characteristics enable them to connect with the negative charges on the cell surface and give them entry, which causes an accumulation in the cytoplasms of the cells in the aquatic ecosystems. methylene blue (MB) is among a water-soluble cationic dye, which non-biodegradable, poisonous, and cancerous derivative of phenothiazine utilized in textile dyeing (Hosseini *et al.*, 2022; Kalaycıoğlu *et al.*, 2023). It also damages septic tanks during wastewater treatment (Kang *et al.*, 2018).

Several approaches, such as adsorption (Hosseini *et al.*, 2022), membrane separation (Ayub & Othman, 2023), ultrafiltration (Shoshaa *et al.*, 2023), ion exchange, reverse osmosis (Ali *et al.*, 2023), coagulation (Solano *et al.*, 2023), and photocatalysis (Rostami *et al.*, 2022; Zhang *et al.*, 2022) have been used to eliminate MB from contaminated water. Among these, photocatalytic degradation using transition metal oxide-based semiconductors is the most promising because it is simple and low-cost related to other

methods mentioned above, which have expensive operation prices, and take an extensive time to eliminate organic pollutants (Bakry *et al.*, 2022).

In addition to the pure water access issue, energy supply is one of the challenges of our globe. Recently, the transmission of energy has emerged as a critical scientific and technological need. People in several nations and urban regions may not always have easy access to alternative energy sources (Rahman *et al.*, 2023). With continued economic development, energy demand has risen significantly in recent years. Currently, global power consumption is about 13 TW and is forecasted to reach about 23 TW in the year 2050 (Hatamvand *et al.*, 2020; Mehmood *et al.*, 2014). Fossil fuels, which used to meet energy demands which provide more than 80% of global energy demands and are the main cause for increased CO_2 concentration in the environment, which is a big problem in terms of climate change and the warming of the planet (Mehmood *et al.*, 2014; Valenzano *et al.*, 2010). The pollutants and greenhouse gas emissions caused by the combustion of these fuels are a major source of concern in today's environmental policy (Ahmad *et al.*, 2017). These concerns have recently prompted scientists to focus their research on renewable energy sources such as wind, solar, thermal, hydro-power, and biomass (Ahmad *et al.*, 2017; Ashok *et al.*, 2024). Solar energy is the most efficient of these renewable energy methods since it is obtained freely from the sun, is clean, and pollution-free (Cheng *et al.*, 2019). The sun's energy is converted into usable types of energy by these photovoltaic systems (Sofyan *et al.*, 2017).

Three different types of solar cell technologies have been developed. Solar cells of the first types are made of silicon crystalline wafers, which supply 93% of the solar cell demand (Mohamed & Selim, 2017). Solar cells of the second generation are made up of non-crystalline silicon (amorphous silicon), cadmium telluride, and copper gallium indium di-selenide. Dye-sensitized solar cells (DSSC), quantum dot (QDs), organic, and perovskite solar cells (PSC) make up the third generation of photovoltaic cells (Bhattacharya & Datta, 2020; Tomar *et al.*, 2020). Among them, the DSSC is one of the ecologically friendly and inexpensive devices with a wide variety of possibilities (Bhattacharya & Datta, 2020).

A significant amount of research has been done in recent years on building high-performance DSSCs with higher efficiency, lower costs, and improved reliability (Zatirostami, 2020). DSSCs use broad bandgap semiconductor sensitization to convert

photon energy into electricity and are part of the thin-film photovoltaic technology group (Najm *et al.*, 2023). Because of their relatively low cost, these devices offer amazing alternatives to silicon-based solar cells. The dye sensitizer absorbs the incident of sunlight energy to drive electron transport. Electron transport from dye to semiconductor occurs in DSSC (Balachandran *et al.*, 2021). During the electron transfer process in DSSC, the active material of the photoanode is critical. Modification of photoanode material for improving DSSC photovoltaic performance has recently been investigated (Hidayat *et al.*, 2021).

Based on their physicochemical properties, nanomaterials have a wide range of applications in domains such as energy conversion and storage (Anigol *et al.*, 2017), medicine, pollution remediation, cosmetics, and pharmaceuticals (Haleem *et al.*, 2023; Verma *et al.*, 2022). The chemical, physical, electrical, and optical properties of nanomaterials are all influenced by particle size, shape, and surface morphology (Annu & Ahmed, 2018).

Transition metal oxide (TMO) nanomaterials have a technologically wide range of applications (Sahoo *et al.*, 2024). TMO nanomaterials, such as ZnO (Y. Sun *et al.*, 2023), Nb_2O_5 (Pawar *et al.*, 2023), SnO_2 (Shabna *et al.*, 2023), CuO (Baral *et al.*, 2024), CeO_2 (Kusmierek, 2020), $BiVO_4$ (Kamble *et al.*, 2023), WO_3 (Liu *et al.*, 2023), Fe_2O_3 (Alp & Borazan, 2023), TiO_2 (Solymos *et al.*, 2024), and In_2O_3 (Devia & Singh, 2020) are used in different applications because of their fascinating thermal, optical, electrical, and magnetic properties.

Due to its several important properties, such as photocatalytic ability, low toxicity, high oxidizing power, biocompatibility, excellent chemical stability, and ease of accessibility, TiO_2 is one of the most effective in photocatalytic hydrogen production, photodegradation of organic pollutants and dyes, as well as good antimicrobial activity (I. Ali *et al.*, 2018; Luthfiah *et al.*, 2021). It is considered environmentally friendly and has been used in numerous industrial applications, including gas sensors (Nunes *et al.*, 2022), corrosion protection (Das *et al.*, 2021), white pigment (Wu, 2021), DSSCs (Jayachithra *et al.*, 2022), remediation of the environment (Arun *et al.*, 2023), for hydrogen gas production (Naldoni *et al.*, 2018), high dielectric, high electrical resistance (Bonkerud *et al.*, 2021), and the reduction of CO_2 (Rehman *et al.*, 2022).

Among numerous semiconductor catalysts, ZnO stands out because of its exceptional properties. It has more positive potential than the redox potential of water and more

negative potential than the redox potential of oxygen (Ali *et al.*, 2024). Applying ZnO in a photocatalytic reaction can reduce oxygen. ZnO has high redox potential, better chemical and thermal stability at high temperatures, good defect chemistry, and a considerable excitonic binding energy of 60 meV (Song *et al.*, 2023). Additionally, ZnO has the widest variety of nano-morphological formations, which is advantageous for a variety of uses. However, ZnO's two primary disadvantages are insufficient absorption of visible light and electron-hole recombination. (Debnath *et al.*, 2024). CuO has a small bandgap (1.2-2 eV) and is a naturally occurring p-type semiconductor, having a conductivity of 10^{-4} S/cm (Sakib *et al.*, 2019). It is crucial in a variety of applications, including gas sensors, high-temperature superconductors, wastewater treatment, and solar energy conversion (Dulta *et al.*, 2022). The monoclinic crystal structure of CuO exhibits excellent physical and chemical properties such as large surface areas, good electrochemical activity, high redox potential, good thermal conductivity, and outstanding stability in solutions (Raizada *et al.*, 2020).

Despite the outstanding advantages of TiO_2, it has limitations due to its wide bandgap and high electron-hole recombination, which results in a low quantum efficiency (Yang *et al.*, 2022). A single metal oxide semiconductor photocatalyst could not accomplish the required performance due to photon-induced electron-hole recombination and surface area drawbacks. As a result, nanocomposites of materials will act as good photocatalysts, due to their charge separation capacity, visible light harvesting tendency, and resistance against photo corrosion (Raizada *et al.*, 2021). The choice of photocatalytic components depends on their valence/conduction band potentials and bandgap energy (Suresh *et al.*, 2023). Forming a heterojunction/interface between metal oxides increases the surface area to volume ratio due to the synergistic effect and minimizes the photon-induced electron/hole recombination due nto charge transfer through the interface and improved light harvesting capabilities (Ortiz-Quiñonez & Pal, 2024). One can use metal oxides with a similar bandgap or different bandgap materials to generate heterojunction-structured (Abebe *et al.*, 2020; Araújo *et al.*, 2023; Kubiak *et al.*, 2019).

So far, there is no scientific report on photocatalytic and solar cell applications of TiO_2, TiO_2/CuO, and TiO_2/ZnO nanomaterials synthesized by IHL extract. Thus, this work aims

to evaluate the photocatalytic removal of MB from an aqueous solution and DSSC energy conversion performances of TiO_2, TiO_2/CuO, and TiO_2/ZnO nanomaterials synthesized using *IHL* extracts. In addition, *Impatiens rothii Hook. f. roots (IHR) and flowers (IHF), Thymus schimperi Ronniger flowers (TRF),* and *Rumex nepalensis Spreng flowers (RSF) were reported as the sensitizers of DSSC conversion devices for the first time.* These plants have a wide range of accessibility and are inexpensive and non-toxic. *Impatiens rothii* Hook. *f.* (Gishilt) is a flora classified under the family of Balsaminaceae (Yohannis *et al.*, 2018). It is a tuberous species native to Ethiopia and is used as a local wound treatment, especially for burnt skin. Additionally, because of its great adhesive qualities and vibrant color, its root extract is utilized to beautify palms and nails. *Rumex nepalensis* Spreng (Tult) has a wide range of therapeutic activities and has been extensively used as a traditional medicine for centuries (Gonfa *et al.,* 2021). Leaves and immature roots of *R. nepalensis* are also reported to be used as a food supplement and dyeing agent. Rumex nepalensis contains anthraquinones such as emodin glycoside, chrysophanol glycoside, emodin, and chrysophanol (Sharma *et al.,* 2021). *Thymus schimperi* Ronniger (Tosign) is an endemic plant in Ethiopia. Traditionally it is used as a food additive and spice for flavoring hot drinks like tea and coffee. It is a well-known medicinal plant used as an antioxidant, anti-inflammatory, anticarcinogenic, antidiabetic, neuroprotective, hypoglycemic cardioprotective, and antimicrobial properties due to the presence of secondary metabolites consisting of alkaloids, flavonoids, Saponins, and terpenoids and tannins (Afonso *et al.*, 2020; Bisrat *et al.*, 2022; Shewasinad *et al.*, 2018; Yikna & Yehualashet, 2021). Desta and his colleagues reported that the major components of *Thymus schimperi* Ronniger include polyphenols like flavones and luteolin (Desta *et al.*, 2017).

1.2 Statement of the Problem

Water contamination is a result of the release of both organic and inorganic contaminants caused by industrialization, which is gradually increasing to meet community demands (Zhang *et al.,* 2019). Nowadays, wastewater contaminated by dyes is one of the biggest environmental issues. Special characteristics of dyes include their great solubility in water, their resilience against light, which can disrupt the flow of sunlight into the water, and their strong carcinogenic, mutagenic, and poisonous effects (Masoudian *et al.,* 2019). Therefore,

removing dyes from wastewater is a significant worldwide issue for protecting the environment and public health. MB dye, one of the hazardous cationic dyes, is used to color wool, silk, and cotton textiles. It can lead to convulsions, methemoglobinemia, dyspnea, tachycardia, eye burn, cyanosis, and skin irritation. It may cause nausea, vomiting, diarrhea, and gastrointestinal irritation (Boukoussa *et al.*, 2018; Yaqoob *et al.*, 2020).

Sustainable and affordable energy is essential to improve human welfare and living conditions. The majority of these energy requirements are now met by carbon-based fuels, which emit gases such as CO_2, which is the principal driver of global warming (S. Abrol *et al.*, 2021; Valenzano *et al.*, 2010).

The DSSC systems use dyes as the light absorber (Hidayat *et al.*, 2021) to produce energy. Ruthenium-based compounds are the most effective sensitizers for DSSC due to their good stability, increased absorption in the wide range of the solar spectrum, excellent electron injection, and efficient metal-to-ligand charge transfer properties. Although ruthenium-based dyes can have good energy conversion efficiency, their complexes are recognized to be costly because of limited resources and their negative environmental effects (Pramananda *et al.*, 2021; Zatirostami, 2020).

Because of their harmless features, natural abundance, inexpensive production costs, and environmental friendliness, natural dyes obtained from fruits, leaves, and roots of plants have therefore gained the attention of researchers (Hidayat *et al.*, 2021). The current study used natural plants as sensitizers to fabricate DSSCs. The root extract of *Impatiens rothii Hook. f.*, a plant native to Ethiopia, traditionally used by girls for decorative purposes for their palms and fingers, has good resistance to temperature and fading. Despite its cultural importance, no study has been conducted on the potential of this plant as a natural dye for solar energy applications.

1.3 Objectives of the Study

1.3.1 General Objective

The general objective of this work is to study the photocatalytic degradation of Methylene blue and DSSC energy conversion efficiencies of TiO_2, TiO_2/CuO, and TiO_2/ZnO synthesized using *Impatiens rothii Hook. f.* leaf extract.

1.3.2 Specific Objectives

The specific objectives of this study are:

- To extract IHL, IHF, IHR, *TRF*, and *RSF and identify their* phytochemicals.
- To synthesize pristine TiO_2, TiO_2/CuO, and TiO_2/ZnO nanocomposites by green synthesis method using *IHL* extract.
- To characterize the synthesized nanomaterials using TGA, XRD, UV-Vis-DRS, PL, XPS, SEM-EDX, TEM/HRTEM, BET, and Raman analytical techniques.
- To evaluate the photocatalytic performance of pristine TiO_2, and TiO_2/CuO, and TiO_2/ZnO nanocomposites against MB dye.
- To study the DSSC energy conversion performance of pristine TiO_2, TiO_2/CuO, and TiO_2/ZnO nanocomposites.

1.4 Significance of the Study

Issues about the cleanup of hazardous waste and similar problems have become national and international priorities. According to literary works, the advanced oxidation process (AOP) is an alternative method of removing unwanted contaminants, including dyes. The green method approach is considered a promising route to control the growth, morphology, and properties of the nanocomposites. The aggregation/agglomeration of metal oxide nanocomposites can be avoided by using *Impatiens rothii Hook. f.* leaves extract as a capping agent, which is eco-friendly and non-toxic. The dye-sensitized solar cell is both cost-effective and environmentally benign since the plants used for this work are readily and abundantly available in Ethiopia. Because the DSSC energy conversion system does not emit CO_2, one of the most common greenhouse gases, this energy source reduces the greenhouse effect. As a result, this work will give starting information to the scientific community to work in-depth on *Impatiens rothii Hook. f.* roots and flowers, *Thymus schimperi Ronniger* flowers, and *Rumex nepalensis Spreng* flowers efficiency. Furthermore, it offers an alternate wastewater treatment route for the dye-releasing industries and governmental and non-governmental organizations dealing with environmental protection.

1.5 Scope of the Study

This work was limited to the evaluation of MB photocatalytic degradation and DSSC energy conversion performance using pristine TiO_2, as well as TiO_2/CuO and TiO_2/ZnO nanocomposites, which were synthesized using the extract of *Impatiens rothii Hook. f.* leaves (IHL) as a reducing and capping agent. The prepared materials were characterized using XRD, FTIR, UV-Vis-DRS, SEM-EDX, BET, Raman, XPS, TEM, HRETM, and PL techniques. The photocatalytic performances of the green synthesized nanomaterials were evaluated using methylene blue as a representative pollutant dye. The reusability of synthesized nanomaterials was investigated. The JV, IPCE, and DSSC conversion efficiency measurements were performed.

2 LITERATURE REVIEW

2.1 Methylene Blue Dye

Methylene Blue is a synthetic cationic dye that finds widespread application in biological staining, the textile industry, and as a redox indicator. However, because of its extensive use, there are concerns about how it may affect the environment, especially in aquatic systems (Fito *et al.*, 2023). There are serious environmental hazards when MB is released into water bodies. For aquatic life, MB can be toxic, resulting in altered behavior, decreased rates of reproduction, and death (Khan *et al.*, 2022). Studies indicate that exposure to MB can adversely affect fish, algae, and other aquatic organisms, disrupting ecosystems. MB is resistant to biodegradation, leading to its accumulation in water bodies. Its stability and solubility contribute to its persistence, necessitating effective removal methods to mitigate environmental impact (Khan *et al.*, 2022). To remove such contaminants using photocatalytic techniques, photocatalyst materials like Transition metal oxides play a great role.

2.2 Transition Metal Oxides

Transition metal oxides (TMOs) have emerged as significant materials in photocatalytic and DSSC applications due to their unique properties, such as tunable band gaps, high stability, and the ability to facilitate redox reactions under light irradiation. TMOs are inorganic compounds that consist of transition metals and oxygen. They exhibit a variety of electronic and optical properties, making them suitable for applications in photocatalysis and DSSC systems. Their ability to absorb light and generate charge carriers (electrons and holes) is crucial for driving chemical reactions (Sahoo *et al.*, 2024).

2.2.1 Synthesis Methods of TMOs

Basic synthesis methods for TMOs nanomaterials include physical, chemical, and biological/green approaches. These synthesis methods can be further divided into bottom-up and top-down approaches. Nanoparticles are initially obtained at the atomic level and then incorporated into the appropriate material via the bottom-up technique. This comprises the creation of NPs from colloidal dispersion and powders from the sol–gel technique, followed by integration (Saleh, 2020). The build-up of material from atoms to clusters to nanoparticles is known as the bottom-up or constructive process. The most prevalent

bottom-up processes for nanoparticle generation are sol-gel, spinning, chemical vapor deposition (CVD), pyrolysis, and biosynthesis (Ealia & Saravanakumar, 2017). Some of the synthesis methods are shown in Figure 1.

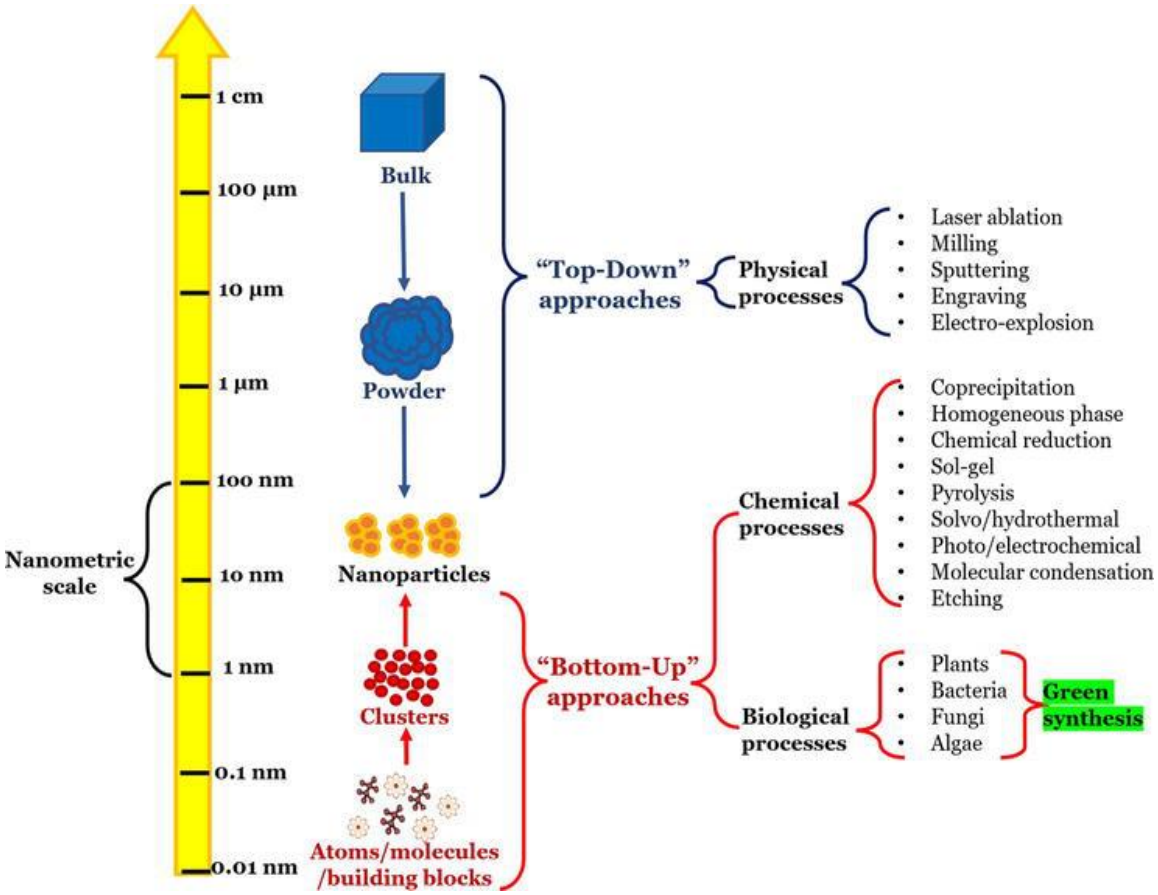

Figure 1. Different nanoparticle synthesis approaches and methods (Álvarez-Chimal & Arenas-Alatorre, 2023).

Microwave Heating

Irradiation with microwaves (MW) is a quick and easy way to produce energy for chemical reactions. Microwave technology is a powerful energy source capable of completing chemical changes in minutes rather than hours or days of high-temperature heating. Microwaves are electromagnetic waves with frequencies ranging from 0.3 to 300 GHz and wavelengths ranging from 1 mm to 1 m that are used in microwave-assisted procedures. The two major methods of microwave heating are dipolar polarization and ionic conduction (Nyamukamba *et al.*, 2018). Microwave heating may have various advantages over traditional heating, including faster reaction times, higher heating rates, and better product

uniformity (Machut *et al.*, 2020). Table 1 shows examples of nanomaterials synthesized through the microwave method.

Table 1. Nanomaterials synthesized by microwave and their applications.

Nanomaterials	application	References
TiO_2/CuO	photocatalysis	(Kubiak *et al.*, 2020)
TiO_2/CuO	photocatalysis	(Kannan *et al.*, 2021)
TiO_2/Au	photocatalysis	(May-Masnou *et al.*, 2018)
CuO/CoO	photocatalysis	(Gouasmia *et al.*, 2022)

Sol-Gel Method

The sol-gel method of material synthesis is a straightforward, low-cost, and low-temperature procedure. The early development of a gel ensures great homogeneity and eliminates the requirement for atomic diffusion during solid-state calculations. Furthermore, metal alkoxides are frequently used as precursors, as many of them are liquids or volatile solids that may be easily filtered, resulting in exceptionally pure oxide precursors. This component is crucial in the production of electroceramics. The comparatively high costs of metal alkoxides, on the other hand, may be prohibitive for some applications, and the release of considerable volumes of alcohol during the calcination stage necessitates specific safety precautions. After forming a solution containing the suitable precursors, hydrolysis and condensation are used to convert the solution into homogenous oxide (gel). The oxide product is obtained by drying the gel and then calcining it. Alkoxides are usually combined with alcohol to make multi-component oxides. Acetates and other components for which no alkoxides are available are introduced as salts. The temperature, pH, and concentration of alkoxides, as well as the addition of water and alcohol, are all controlled during the hydrolysis process (Srivastava, 2012). Table 2 shows some examples of nanomaterials synthesized by sol-gel methods.

Table 2. Nanomaterials synthesized by sol-gel methods.

Nanomaterial	application	References
TiO_2/CuO	photocatalysis	(Khoroshko *et al.*, 2023)
TiO_2/CuO	photocatalysis	(Chi & Wang, 2022)
TiO_2/CuO	photocatalysis	(YILDIRIM *et al.*, 2010)
TiO_2/CuO	photocatalysis	(Muzakki *et al.*, 2016)
TiO_2/CuO	photocatalysis	(Celik *et al.*, 2006)
TiO_2/CuO	Photocatalysis	(Roy, 2022)

Green Synthesis of TMOs

The use of physical and chemical processes to make nanoparticles produces hazardous byproducts that are harmful to the environment. As a result, the green synthesis approach is thought to be a promising alternative for producing biocompatible and stable nanoparticles (Patra & Baek, 2014). Green synthesis methods are needed to avoid the formation of toxic byproducts by developing dependable, long-lasting, and environmentally friendly synthesis procedures. The synthesis of nanoparticles by fungi, bacteria, algae, and plants is a common green synthesis approach (Singh *et al.*, 2018). Plant-derived nanoparticles are more long-lasting, cost-effective, and quite innovative. Plant extracts have the advantage of being dual-purpose, working as both reducing and stabilizing agents to aid in the creation of nanoparticles (El Shafey, 2020; Gnanasangeetha & Suresh, 2020). Examples of TMOs synthesized by green methods using plant extract are listed in Table 3.

Table 3. Examples of green synthesized TiO_2/CuO nanocomposites and their photocatalytic application.

Plant	References
Rubus ellipticus	(Bisht *et al.,* 2023)
C. benghalensis	(Bopape *et al.*, 2023)
A. carambola	(Etape *et al.*, 2017)
Moringa Oleifera	(Solano *et al.*, 2023)
Eichhornia crassipes	(Lu *et al.*, 2019)

2.3 Photocatalysis for the Removal of Pollutants

The removal of contaminants is the main goal of several wastewater treatment techniques. These consist of advanced oxidation techniques such as photocatalysis, biological processes, adsorption processes, electrochemical oxidation, and physicochemical procedures (Rezaei *et al.*, 2023; Salem *et al.*, 2023). When it comes to removing organic contaminants from water, photocatalytic degradation is the most promising approach due to its ease of use, speed, cleanliness, and affordability when compared to other methods that require large running expenses and take a long time (Rezaei *et al.*, 2023). The application of photon energy to start a specific reaction process is known as photocatalysis. Consequence to their ability to eliminate various organic contaminants present in water through a sequence of redox processes, semiconductor materials have gained more attention in the photocatalysis community. The stimulation of electrons from the valence band to the conduction band brought on by the absorption of a photon at the right wavelength is linked to semiconductors' capacity for photocatalysis.

Photocatalysis is a series of chemical reactions induced by electromagnetic irradiation. This will cause the excitation of atoms of the irradiated materials, which results in radicals that affect the surroundings. The photocatalysis process can be classified into reduction and oxidation (Konstantinova *et al.,* 2019). Exciton or electron/hole (e^-/h^+) pairs emerge when

the photocatalyst absorbs the necessary light energy, with holes in the valence band and electrons in the conduction band. Each charge carrier may go in different directions depending on the surroundings and band edge positions of the adsorbed species' redox potential. In the valence band, holes cause oxidation, whereas in the conduction band, electrons cause a reduction. Alternatively, both holes and electrons may combine again. Reactive oxygen species (ROS) as superoxide anion radicals (O_2•−), hydroxyl radicals (OH), singlet oxygen species (O_2), and peroxide molecules (H_2O_2), are therefore produced by the charge carriers. The redox reactions mentioned above are listed below in Equations 1-8 (Kermani *et al.*, 2023; Kumari *et al.*, 2023; Salem *et al.*, 2023; Tahir *et al.*, 2022).

$$\text{Semiconductor} + \text{hv} \rightarrow \text{Semiconductor}(\text{h}_{\text{VB}}^{+} + \text{e}_{\text{CB}}^{-}) \quad (1)$$

$$\text{e}_{\text{CB}}^{-} + \text{O}_2 \rightarrow \text{O}_2^{\bullet -} \quad (2)$$

$$\text{O}_2^{\bullet -} + \text{H}^{+} \rightarrow \text{HO}_2^{\bullet} \quad (3)$$

$$2\text{HO}_2^{\bullet} \rightarrow \text{H}_2\text{O}_2 + \text{O}_2 \quad (4)$$

$$2\text{HO}_2^{\bullet} \rightarrow \text{H}_2\text{O}_2 + \text{O}_2^{\bullet -} \rightarrow \text{OH}^{\bullet} + \text{O}_2 + \text{OH}^{-} \quad (5)$$

$$\text{h}_{\text{VB}}^{+} + \text{OH}^{-} \rightarrow \text{OH}^{\bullet} \quad (6)$$

$$\text{h}_{\text{VB}}^{+} + \text{H}_2\text{O} \rightarrow \text{OH}^{\bullet} + \text{H}^{+} \quad (7)$$

$$\text{OH}^{\bullet} + \text{MB} \rightarrow CO_2 + H_2O + Minerals \quad (8)$$

2.4 DSSC Energy Conversion

The various types of solar cells can be categorized into three generations. Silicon wafer-based photovoltaics currently accounts for 93% of the solar cell market and have had a significant edge over other device architectures and materials for many years. Because of their great efficiency and stability, silicon-based solar cells have been employed for a long time. They do, however, have several significant flaws (Bera *et al.*, 2021). Because silicon-based solar cells have some drawbacks, such as high fabrication costs and the production of harmful gases during fabrication, researchers are looking for other options (Chougala *et al.*, 2017). Amorphous silicon is used in the second generation of thin-film technology to create a homogenous thin layer. One of the most significant advantages of thin film technology is that it consumes far less silicon. Other materials, such as copper indium sulfide (CIS), copper indium gallium di-selenide (CIGS), and cadmium telluride (CdTe), are also utilized, although silicon continues to be the market leader. Thin-film solar cells have lower

efficiency (10-12%) than silicon solar cells (15-25%), but production costs are lower, resulting in a lower cost per watt (D. K. Kumar *et al.*, 2020; Mohamed & Selim, 2017; Sharma *et al.*, 2015).

DSSC with bio-mimics and artificial photosynthesis are the third-generation cells currently employed in building integration. It's a promising technology that dramatically lowers the initial costs of solar cells. Nanocrystal-based solar cells, polymer-based solar cells, dye-sensitized solar cells, and concentrated solar cells are all examples of third-generation photovoltaic cells (Aduloju *et al.*, 2011; Kibria *et al.*, 2014). Because of the low cost of materials and the ease of manufacture, dye-sensitized solar cells are well-known as cost-effective photovoltaic devices related to high-cost conventional silicon solar cells (Gong *et al.*, 2017).

Figure 2 depicts the general configuration of a typical dye-sensitized photochemical conversion device. Two TCO layer of FTO; a mesoporous metal-oxide layer photoanode; a dye; an electrolyte, and a CE are the major components (Bera *et al.*, 2021; Omar *et al.*, 2020; Wu *et al.*, 2015).

Many TCOs have been developed in the previous thirty years, but the best are ITO and FTO. Due to its low electrical conductivity, low cost, and excellent heat resistance (stable up to 550 °C), FTO is the most used substrate compared to ITO. However, FTO has lower optical transparency and electrical conductivity than ITO (Aslam *et al.*, 2020; Carella *et al.*, 2018).

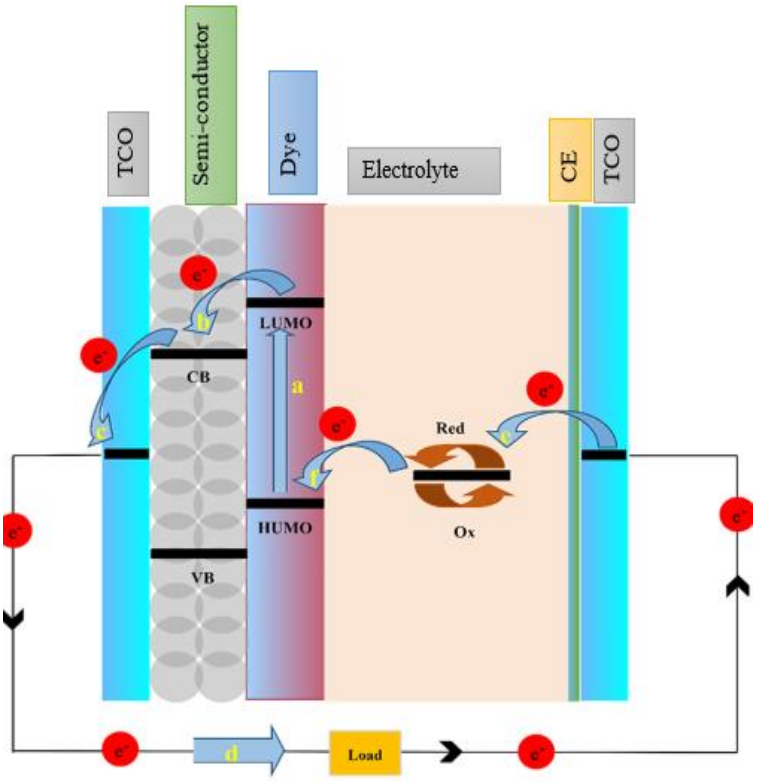

Figure 2. Simple structural components of a DSSC (Tomar *et al.*, 2020).

2.4.1 Conductive Transparent Substrate

A conductive transparent substrate is employed to carry and transport the charges at both ends of DSSCs. This transparent substance is layered on one side with a conductive surface and can be made of glass or polymeric material. These substrates allow for complete catalyst and semiconductor metallic oxide deposition. The overall efficiency of DSSC is largely affected by the transparency and electrical conductivity of the substrate. The resistance of the conducting substrate should be between 10 and 20 Ω/cm^2. Furthermore, the substrate transparency should be greater than 80%. The major conductive substrates in DSSCs are FTO and ITO. When assessing the total efficiency of DSSCs, a comparison of ITO and FTO has shown that the FTO is the more appropriate (Aslam *et al.*, 2020).

2.4.2 TMOs Photoanodes

Mesoporous metal oxide films have exceptional physicochemical properties, including a high band gap, a large surface area, controlled pore size and morphology, strong thermal and chemical stability, unique optical and electrical properties, non-toxicity, and

inexpensive costs. The capacity to interact with molecules not only on their outer surface but also on the massive internal surfaces of the material, giving more accessible active sites for reactants, distinguishes porous metal oxides from non-porous metal oxides (Niu *et al.*, 2018; Topoglidis, 2020). The photoanode/working electrode of DSSCs is made from mesoporous semiconductor metal oxide. It's a porous surface that creates permeable gaps for dye to be adsorbed efficiently. Its job is to catch electrons from dyes and deliver them to the conductive substrate. A thin layer of oxide semiconducting materials such as ZnO, NiO, TiO_2, Nb_2O_5, and SnO_2 is deposited on a transparent conducting glass plate to create metal oxide working electrodes (Aslam *et al.*, 2020; Bykkam *et al.*, 2021; Sharma *et al.*, 2018a; Zhang *et al.*, 2020).

Because of its enormous surface area, homogeneous pore size, structural homogeneity, and integrity, mesoporous TiO_2 is a good candidate for dye-sensitized solar cell production (Zhang *et al.*, 2020). To date, TiO_2 has been the most widely utilized photoanode material, with a DSSC efficiency of roughly 14% (Gnida *et al.*, 2021). In general, TiO_2 is the material of choice due to superior properties such as the position of the conduction band (the TiO_2 conduction band is lower than the LUMO level of most commonly used organic dyes, allowing for faster electron transfer), low toxicity, high chemical stability, and a high refractive index (n = 2.5 for anatase) which allows for efficient diffuse scattering of light inside three crystalline layers. TiO_2 comes in three different crystal structures. These are anatase, rutile, and brookite with a bandgap of 3.2 eV, 3.0 eV, and 3.4 eV, respectively. The porous photoelectrode, with its high dielectric constant (£ = 80 for anatase) and good electrostatic shielding of the injected electrons from the oxidized dye molecule connected to the TiO_2 surface, inhibits the quick recombination of the electrons at the TiO_2/dye interface site. (Su'ait *et al.*, 2015).

Photocatalysis, separations, sensor devices, paints, and dye-sensitized solar cells are just a few of the applications for TiO_2 NPs. The material properties of TiO_2 nanoparticles are determined by the crystal structure, nanoparticle size, and shape, and are thus substantially influenced by the synthesis procedure. Anatase, brookite, and rutile are the three primary phases of TiO_2. Although rutile is the most stable phase in bulk, most solution-phase production procedures for TiO_2 favor the anatase structure. The surface energy of anatase is lower than that of rutile and brookite at very small particle dimensions, and it has been

discovered that the surface energy of anatase is lower than that of rutile and brookite. The crystal structure stability has been explained using a molecular model, in which the precursor chemistry, which is dependent on the reactants utilized, determines the nucleation and development of the various polymorphs of TiO_2 (Aslam *et al.*, 2020; Nyamukamba *et al.*, 2018).

In comparison to rutile and brookite, the anatase phase possesses traits such as an indirect band gap, which prevents the direct transfer of electrons from the conduction to the valence band, resulting in an order of magnitude longer lifespan for photogenerated electrons. In addition, the recombination of photogenerated carriers is significantly lower in anatase due to a reduced photo carrier effective mass, which may aid their rapid migration (Aslam *et al.*, 2020). Rutile is the most frequent form, with a tetragonal structure, 6 oxygen atoms per unit cell, and TiO_6 as an octahedron that is slightly deformed. Rutile is the most thermodynamically stable phase of TiO_2, with a low value of Gibbs free energy at atmospheric pressure compared to anatase and brookite. Rutile transforms irreversibly from anatase and brookite to rutile during calcination, beginning at 600 °C and ending at 900 °C. Anatase has a tetragonal structure as well, even though the TiO_6 octahedron in the anatase phase is more deformed than in the rutile phase. Anatase is more stable at low temperatures, and rutile and anatase are widely utilized in photocatalysis processes. Because the conductive band of anatase is closer to the negative position than that of rutile, it is more photoactive. This increases the reducing power. Furthermore, the Fermi level is somewhat higher, with strong electron mobility, low density, and lower surface energy, all of which contribute to the production of anatase solar cells (Aslam *et al.*, 2020; Rao *et al.*, 2016).

2.4.3 Photosensitizers (dyes)

Photosensitizers are the most important component of DSSC, and there are a variety of photosensitizers based on their chemical and physical qualities. Metal-free sensitizers, natural sensitizers, and metal complex sensitizers are among the many types of photosensitizers (Conradie, 2024; Kumara *et al.*, 2017; Tomar *et al.*, 2020). The most crucial component of dye selection is that the dye's redox potential is high, allowing it to regenerate quickly by taking electrons from the electrolyte. For efficient operation in

DSSCs, the dye should have electrochemical and photophysical properties (Sharma *et al.*, 2018b).

An ideal dye sensitizer should meet the following criteria:

i. The absorption spectrum is broad; maximum photons are harvested from visible to near-infrared wavelengths.
ii. It Possesses a high extinction coefficient.
iii. The dye should be luminescent;
iv. Production of photo-excited electrons upon absorption;
v. The ability of the mesoporous semiconductor layer to effectively infuse charge into the conduction band;
vi. Appropriate levels of LUMO and HOMO provide effective electrons injection;
vii. Dye regeneration; the oxidation potential of dye should be higher than the oxidation potential of the redox couple contained in the electrolyte;
viii. Presence of chemical groups that are capable of permanent chemisorption of photosensitizer onto photoanode surface, such as –COOH, $–H_2PO_3$, $–SO_3H$;
ix. Possess good thermal and chemical stability, and good solubility (Krawczak, 2019; Rahman *et al.*, 2023; Sharma *et al.*, 2018a; Trihutomo *et al.*, 2019)**.**

Natural Dye Photosensitizers

Natural dyes extracted from plant resources are an alternative method of manufacturing cost-effective colors on a wide scale. These dyes are derived from naturally occurring colorful flowers, leaves, and fruits, among other sources. The hues come from the presence of many pigments that are effective photosensitizers. Natural dyes also have several advantages, including a simple preparation method, complete biodegradation, ease of access, high availability, environmental friendliness, and, most notably, a large decrease in the usage of precious metals and a low manufacturing cost (Ludin *et al.*, 2014; Tomar *et al.*, 2020).

The electronic structure of these plant pigments interacts with sunlight, changing the wavelengths that are either transmitted or reflected by the plant tissue. Plant pigmentation results from this process, and each pigment is characterized by the wavelength of maximum absorption (λmax) and the color observed by humans. Chlorophyll, carotenoid, flavonoid,

and anthocyanin are natural color pigments that are comparatively easier to extract from natural resources than manufactured dyes. Figure 3 depicts a flow chart illustrating the various pigment classifications found in plants. Plant pigments are classified into four categories, as depicted in the flow chart (Kumara *et al.*, 2013).

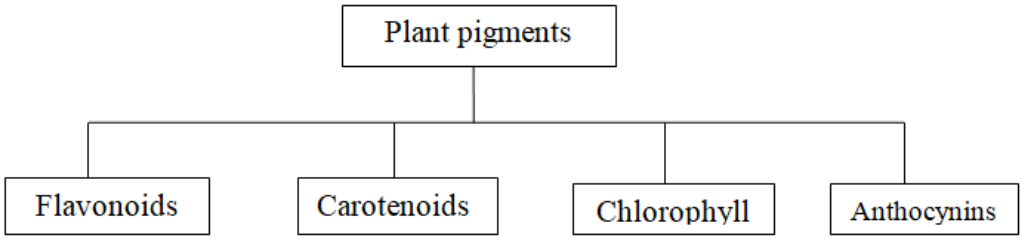

Figure 3. Classification of plant pigments.

Carotenoids

Carotenoids are organic pigments that can be found in plants, as well as some fungi and algae (Nabi *et al.*, 2020). They are a vast family of isoprenoids with over 700 members that produce a variety of red, orange, and yellow fruits and flowers. The presence of a C_{40} hydrocarbon backbone distinguishes carotenoids, causing structural and oxygenic changes. (Ashenafi *et al.*, 2023; Mezzomo & Ferreira, 2016). The molecular structures of zeaxanthin, lutein, beta-cryptoxanthin, and astaxanthin are shown in Figure 4 A-D, respectively. The β-ionone ring of β-carotene and its derivatives, which act as vitamin precursors, is the most abundant end group. By undergoing hydrogenation, dehydrogenation, cyclization, oxygen insertion, double bond migration, methyl migration, chain elongation, and chain shortening, all carotenoids can be classified as lycopene ($C_{40}H_{56}$) derivatives (Zhang *et al.*, 2014).

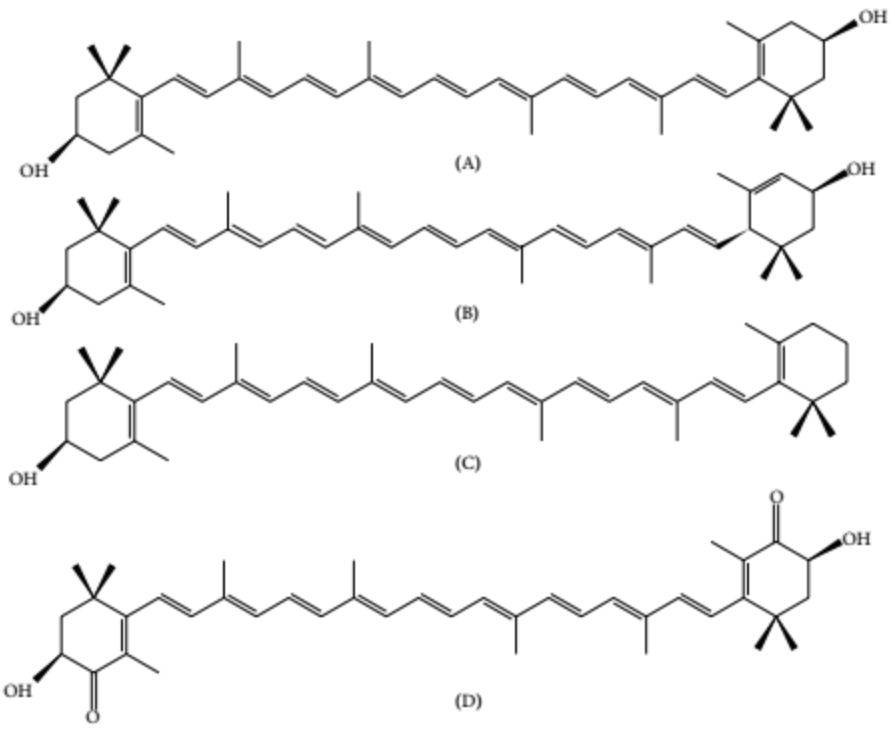

Figure 4. Carotenoids structure: (A) zeaxanthin, (B) lutein, (C) beta-cryptoxanthin, and (D) astaxanthin(Mezzomo & Ferreira, 2016).

Chlorophyll

Chlorophyll is a green pigment that can be found in the leaves of green plants, algae, and cyanobacteria. It can absorb red, blue, and violet wavelengths of light and obtain its color from green reflection (Al-Alwani *et al.*, 2017; Bera *et al.*, 2021). Over 50 tetrapyrrolic pigments have been discovered, comprising six main forms of chlorophyll pigments. Chlorophyll-a and chlorophyll-b, however, are the most often used. Because of the presence of phytyl and alkyl groups in the structure, chlorophyll-a has poor adsorption and sensitization on photoanodes. As a result, steric hindrance occurs, preventing chlorophyll molecules from binding efficiently to the photoanode. Chlorophyll-b differs from chlorophyll-a in the presence of the aldehyde group (-CHO) instead of the methyl group ($-CH_3$). In addition, as compared to chlorophyll-a, chlorophyll-b has a blue color spectrum and a redshift (Arof & Ping, 2017). Figure 5 depicts the chemical structures of chlorophyll-a and chlorophyll-b. Because of their propensity to absorb blue and red light, chlorophylls are used as sensitizers in DSSCs. Furthermore, photosensitizers that have three carboxylate groups in a molecule but no heavy metal ions have been considered environmentally beneficial (Arulraj *et al.*, 2019).

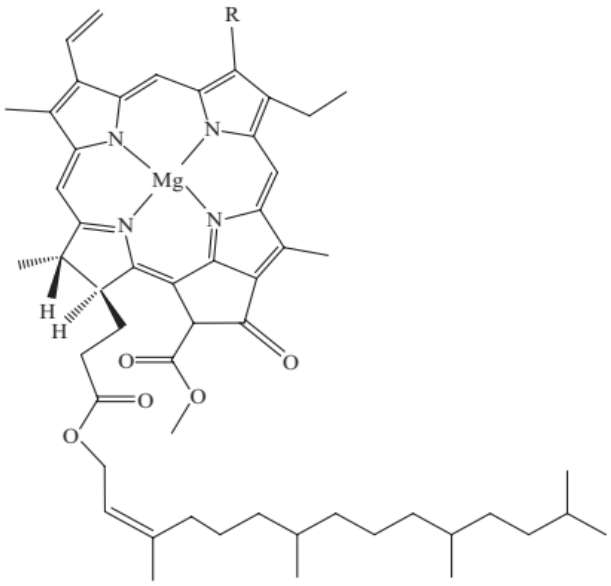

Figure 5. Chemical structure of Chlorophyll, Chlorophyll-a (R=CH_3) and Chlorophyll-b (R=CHO) (Godibo *et al.*, 2015).

Flavonoids

The family of naturally occurring polyphenolic substances known as flavonoids is receiving attention. Their vast distribution and diverse biological activity make them attractive to a wide range of scientific disciplines (Liga *et al.*, 2023). Flavonoids are the most important flower pigments, accounting for most visible spectrum hues. Furthermore, flavonoids are responsible for attracting insects to plants, shielding plants from UV-B radiation, signaling amongst microorganisms in plants, and regulating auxin transport (Kumara *et al.*, 2017).

Flavonoids have a C_6-C_3-C_6 carbon framework with two phenyl rings joined by a three-carbon bridge that usually produces a third ring or, more precisely, phenylbenzopyran activity. The degree of oxidation of the C-ring determines the color of the flavonoid in most cases (Rudrapal *et al.*, 2022). The majority of naturally occurring flavonoid pigment molecules include unbound or loosely bound electrons, lowering the amount of energy required to excite such electrons to a higher energy level (Dias *et al.*, 2021). As a result, the charge transfer transitions from HOMO to LUMO require less energy, allowing visible light to energize the pigment molecules, resulting in a broad absorption band in the visible area (Shalini *et al.*, 2016). Figure 6 depicts the common structure of flavonoids.

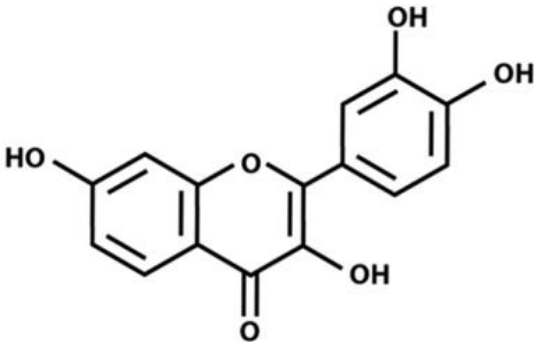

Figure 6. Chemical structure of a commonly occurring flavonoid (Shalini *et al.*, 2016).

Anthocyanins

Anthocyanins are naturally occurring pigments that are responsible for the color of many plant organs, such as the stem, leaf, flower, fruit, root, and tuber (Nassour *et al.*, 2020) . Figure 7 depicts the basic chemical structure of anthocyanin. Anthocyanins are the pigments that give flowers, fruits, and leaves their appealing colors (orange, red, purple, and blue) (Pervaiz *et al.*, 2017). Anthocyanins are commonly used in dye-sensitized solar cell research because their molecules can easily absorb light and become electrified (Shalini *et al.*, 2020). Carbonyl and hydroxyl groups on the surface of anthocyanin molecules help with excitation and electron transfer from the anthocyanin molecules to the conduction band of a porous semiconductor (Ludin *et al.*, 2014; Shalini *et al.*, 2020).

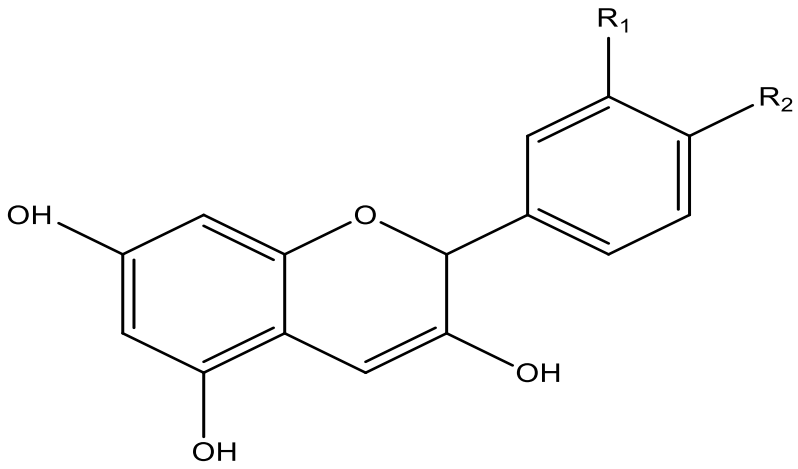

Figure 7. Basic chemical structure of anthocyanin pigment in which 'R' could be replaced with H, OH or OCH_3 depending on the pigment (Krawczak, 2019).

Table 4. DSSC from some natural photosensitizers.

Natural dye source	Photoanode	Electrolyte	Efficiency (%)	Reference
Sweet pomegranate	TiO_2	I^-/I^-_3	1.5	(Godibo *et al.*, 2015)
Sumac/Rhus	TiO_2	I^-/I^-_3	1.5	(Suhaimi *et al.*, 2015)
solanum betaceum	TiO_2	I^-/I^-_3	0.043	(Susanti *et al.*, 2014)
Pterocarpus Indicus	TiO_2	I^-/I^-_3	0.023	(Diantoro *et al.*, 2019)
Mangosteen peel	TiO_2	I^-/I^-_3	0.0071	(Subodro *et al.*, 2017)
Ziziphus jujube	TiO_2	I^-/I^-_3	1.077	(Taya *et al.*, 2015)
Allium cepa	TiO_2	I^-/I^-_3	0.875	(El-Ghamri *et al.*, 2014)
Allium cepa	*ZnO*	*I^-/I^-_3*	*0.19*	*(El-Ghamri et al., 2014)*
Rapa	ZnO	I^-/I^-_3	0.035	(El-Ghamri *et al.*, 2014)
Rapa	TiO_2	I^-/I^-_3	0.86	(El-Ghamri *et al.*, 2014)
Red cabbage	TiO_2	I^-/I^-_3	0.024	(Pratiwi *et al.*, 2017)
S. guineense fruits	TiO_2	I^-/I^-_3	0.51	(Tadesse *et al.*, 2012)
Malvaviscus penduliflorus	TiO_2/MnO_2 bilayer	I^-/I^-_3	0.88	(Datta *et al.*, 2020)
dragon fruit	TiO_2	I^-/I^-_3	0.22	(Ali & Nayan, 2010)
Kalanchoe	TiO_2	I^-/I^-_3	0.61	(George *et al.*, 2020)
Mangosteen	TiO_2	I^-/I^-_3	0.067	(Sofyan *et al.*, 2017)
Mangosteen	TiO_2	I^-/I^-_3	0.003	(Sofyan *et al.*, 2017)
Pomegranate	TiO_2	I^-/I^-_3	2.0	(Ghann *et al.*, 2017)
Hibiscus Sabdariffa calyx	TiO_2	I^-/I^-_3	0.92	(Shalini *et al.*, 2020)
Hibiscus Sabdariffa calyx	TiO_2 doped with 6% Na	I^-/I^-_3	1.65	(Shalini *et al.*, 2020)
Kniphofia schimperi root	TiO_2	EMIM-I	1.3	(Bekele *et al.*, 2021)

The efficiencies of DSSCs are affected by different factors like photo anode material, the type of dye, solvent type, and ratio and percentage of doping materials as shown in Table 4 El-Ghamri et al (2014), reported that TiO_2 photoanode resulted in better efficiency than that of ZnO photo anode for all natural pants dyes which they have tested. The effect of incorporation of the MnO_2 blocking layer into TiO_2 photoelectrode increased the efficiency of DSSC from 0.31% to 0.88% of *Malvaviscus penduliflorus dye* (Datta *et al.*, 2020). Sofyan et al. (2017) tested the effect of solvents on Mangosteen dye, and the efficiencies were recorded as ranging from 3.914% (ethanol-water mixture) to 0.003% (ethanol-acetic acid mixture). The effects of doping material to photo anode on the efficiencies of *Hibiscus sabdariffa calyx* dye were found to be 0.92% (bare TiO_2), 1.65% (TiO_2 + 6% Na), 2.17% (TiO_2 + 6% Na +4% yeast) and 2.4% (TiO_2 + 6% Na +6% yeast) (Shalini *et al.*, 2020).

Metal Complex Sensitizers

Metal complex dyes produced from heavy transition metals like ruthenium, osmium, and iridium complexes have been widely used as inorganic dyes in DSSCs due to their extended excited lifetimes, very effective metal-to-ligand charge transfer spectra, and strong redox properties (Sharma *et al.*, 2018a). Fan and his coworkers have fabricated DSSC from ruthenium dye with an efficiency of 14% (Fan *et al.*, 2017). In most DSSC devices Ruthenium metal complexes are effective due to the following properties (Bera *et al.*, 2021):

I. Its octahedral geometric structure helps in the smooth addition of ligands.
II. The attractive photophysical, photochemical, and electrochemical properties of Ru (II) complexes can be tuned to produce the requisite properties.
III. It possesses stable and affordable oxidation states from I to IV.
IV. It is stable in many solvents.

Due to these properties, it is the most preferable sensitizer in DSSC, and some of the ruthenium dyes are shown in Figure 8. ML2(X)2 is the generic structure of the sensitizer preferred as a dye, where M is a metal center, L is a ligand 2, 2′-bipyridyl-4,4′-dicarboxylic acid (Figure 9), and X can be a halide, cyanide, thiocyanate, acetylacetonate, or thiocarbamate substituent group.

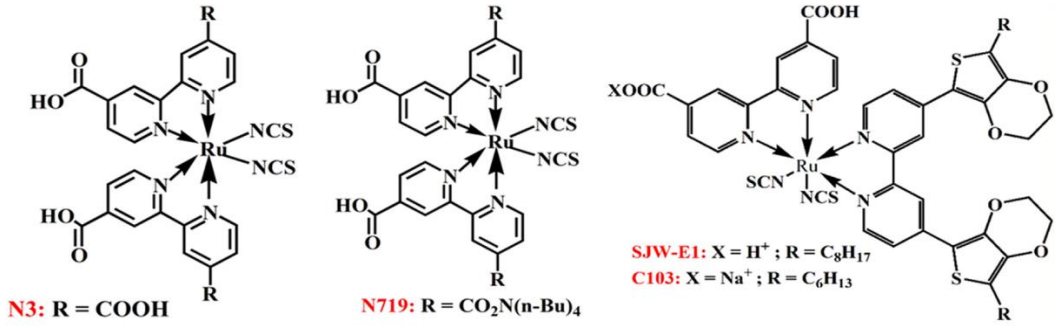

Figure 8. Structures of different ruthenium metal complex dyes (Tomar *et al.*, 2020).

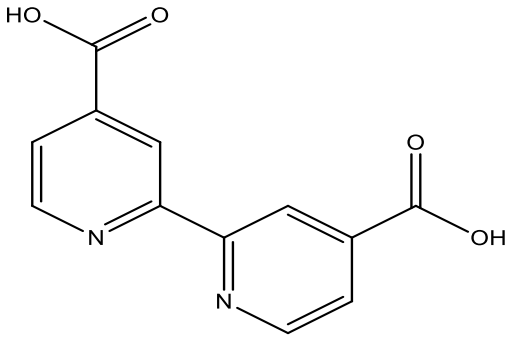

Figure 9. Chemical structure of ligand 2, 2′-bipyridyl-4, 4′-dicarboxylic acid.

Metal-free Organic Dyes

Metal-free dyes like carbazole/hexyl-functionalized oligothiophene/trimethoxysilyl-anchor dye (ADEKA-1), Dibiphenylmonophenylamine dyes (LEG4), eosin Y, aniline blue, bromophenol blue, alcian blue, methyl orange, crystal violet, and fast green have been studied as sensitizers in DSSCs, and significant progress has been made (El-Agez *et al.*, 2014; Kakiage *et al.*, 2015). Metal-free organic dyes have extremely high molar extinction coefficients, readily tunable absorption energies, and are less expensive than Ru-, Os-, and Ir-based complexes. Furthermore, they are free of the poisonous and costly Ru metal. To generate a broad absorption spectrum, these materials can be utilized as both sensitizers and co-sensitizers (Bera *et al.*, 2021). The D-π-A structure is a push-pull structure in which an electron donor (D) group is coupled to an electron acceptor (A) through a π -π-conjugated bridge. In most cases, the electron acceptor also serves as an anchoring group for the dye, allowing it to adhere to the semiconductor surface. This configuration is advantageous in terms of aiding the separation of photoinduced charge after photoexcitation. The electron density shifts from the donor to the electron acceptor side of the molecule, aiding electron

injection into the photoanode conduction band while also inhibiting charge recombination between the semiconductor and the oxidized molecule (Carella *et al.*, 2018). Table 5 shows the effect of the sensitizer on DSSC performance.

Table 5. The Efficiencies of DSSCs of some synthetic photosensitizers using TiO_2 Photoanode.

Dye	Efficiency	References
N719	6.87%	(Colombo *et al.*, 2019)
N719	14%	(Fan *et al.*, 2017)
N719	5.73%	(Pujiarti *et al.*, 2018)
ADEK-1+ LEG4	14.3%	(Kakiage *et al.*, 2015)
N719	8.95%	(T. N. Kumar *et al.*, 2020)
N719	10%	(Ito *et al.*, 2008)

2.4.4 Electrolytes

An electrolyte is one of the basic components in DSSC, which plays a great role in the process of light-to-electricity conversion. Good electrolytes in DSSC should satisfy the following conditions:

i. Produce good interfacial contact with the porous nano-crystalline layer and the counter electrode.
ii. For liquid electrolytes, it is necessary to prevent the loss of the liquid electrolyte by leakage and/or evaporation of solvent.
iii. The electrolyte must be non-corrosive concerning the other DSSC components.
iv. The electrolyte should have the capacity to cause fast regeneration of the dye.
v. The potential of redox couple of the electrolyte must be more negative compared with the HOMO of the dye.
vi. The electrolyte must be stable over time, including chemical, thermal, optical, electrochemical, and interfacial stability, so that the dye does not desorb and degrade from the oxide surface.
vii. The electrolyte should not exhibit a significant absorption in the range of visible light (Bera *et al.*, 2021; Wu *et al.*, 2008).

Solid-state electrolytes, liquid electrolytes (organic electrolytes and ionic electrolytes), and quasi-solid-state electrolytes are the electrolytes used in DSSCs (Khan, Al-Mamun, Halder, *et al.*, 2017; Trihutomo *et al.*, 2019; Venkatesan & Lee, 2017).

Solid-state electrolytes

The term solid-state electrolytes refers to a group of materials that transmit holes (HTM). The carrier transport in HTM-based solid-state DSSC is typically electronic (Li *et al.*, 2009). Organic HTMs such as 2,2',7,7'-tetrakis (N, N-di-4-methoxyphenylamino)-9,9'-spirobifluorene (spiro-OMeTAD) have been employed as solid electrolytes for DSSCs. The oxidized dye can be replenished by injecting a hole into the HTM, which is subsequently collected by the CE to complete an electronic circuit. These findings suggest that using organic HTMs to make solid-state DSSCs has a lot of promise (Duan *et al.*, 2015). Solid-state electrolytes have gotten a lot of interest because of their thermal and long-term stability, solvent independence, and environmental safety. However, high-crystalline solid-state electrolytes have low ionic conductivity, high production costs, and limited mass diffusion capabilities, prompting researchers to look for acceptable electrolytes for DSSCs (Moon *et al.*, 2019; Shaikh *et al.*, 2018).

Liquid state electrolytes

Liquid electrolytes are preferred in DSSCs over solid and quasi-solid electrolytes because of their low viscosity, high conductivity, good interfacial wetting, and ease of manufacture (Thomas *et al.*, 2021). At room temperature, liquid electrolytes are divided into organic solvent-based electrolytes and ionic liquid electrolytes. Organic-based electrolytes are composed of organic solvents, redox couples, and additives. Some of the commonly used redox couples are Br^-/Br_2, I^-/I_3^-, SCN^-/SCN_2, S/S_2^-, $SeCN^-/(SeCN)_3^-$, and Co(II)/Co(III) (Khan, Al-Mamun, Halder, *et al.*, 2017; Thomas *et al.*, 2021). Among these redox couples I^-/I_3^- is an ideal redox couple because of its good solubility, fast ion diffusion, high efficiency, ease of fabrication, low absorbance of light in IR region, rapid dye regeneration, suitable redox potential and very slow recombination kinetics between injected electrons into the semiconductor and triiodide (Khan, Al-Mamun, Halder, *et al.*, 2017). Organic solvents such as acetonitrile, 3-methoxypropionitrile, N-methylpyrrolidone, propylene carbonate, γ-butyrolactone, N-methyl-2-pyrrolidone, ethylene carbonate, and counter ions

of iodides are used in organic solvent-based electrolytes with high dielectric constant, where solvents are the key component of a liquid electrolyte (Khan, Al-Mamun, Halder, *et al.*, 2017; Sharma *et al.*, 2018a). 4-tert-butypyridine, guanidinium thiocyanate, and N-methylbenzimidazole are the most effective additives. The additive's purpose is to absorb at the photoelectrode/electrolyte interface, preventing injected electrons from recombining with tri-iodide ions (Khan, Al-Mamun, Halder, *et al.*, 2017).

Organic solvent-based electrolytes, in comparison to ionic electrolytes, have a fast rate of evaporation due to their high volatility and permeability. To help with these difficulties, ionic solutions have been utilized. Low-temperature molten salts having melting temperatures below 100 degrees Celsius, or liquids consisting solely of ions, are known as ionic liquids (ILs). The salts exhibit weak interactions due to the presence of a large cation and a charge-delocalized anion (Lee *et al.*, 2013). They are a class of organic salts that comprise cations, such as imidazolium and pyridinium, as well as anions derived from halides. They serve as both a solvent and an ionic liquid simultaneously. 1-butyl-3-methylimidazolium chloride, 1-butyl-3-methylimidazolium iodide, and 1-butyl-3-methylimidazolium tetrafluoroborate, 1-methyl-3-propyl imidazolium iodide, 1-butyl-3-methylimidazolium, and 1-hexyl-3-methylimidazolium iodide are the most common ionic liquids (Abu Talip *et al.*, 2020; Khan, Al-Mamun, Halder, *et al.*, 2017; Shi *et al.*, 2013).

Quasi-solid State Electrolytes

This form of electrolyte solves the problem of inadequate contact between the photoelectrode and the HTM in solid-state electrolytes. A quasi-solid-state electrolyte combines a polymer and a liquid electrolyte that can penetrate the photoelectrode and make good contact. The inclusion of an inert polymer, such as poly (methyl methacrylate) (PMMA), results in increased stability, superior electrical conductivity, and particularly good interfacial contact (Hu *et al.*, 2017; Kumara *et al.*, 2017). In DSSCs, quasi-solid state electrolytes are used to avoid the problems of leakage, flammability, and electrochemical stability that liquid electrolytes have. Furthermore, the presence of liquid electrolytes causes desorption and photodegradation of the attached dyes in DSSCs, as well as corrosion of the counter electrode and photodegradation of some components, all of which reduce the cell's lifetime, performance, and practical utility (Su’ait *et al.*, 2015).

2.4.5 Counter Electrode

The counter electrode (CE) is a thin layer of catalyst on a conductive substrate that is one of the most important components in DSSCs. The CE plays two important roles: (a) acting as a catalyst by reducing redox species, which are mediators for regenerating the dye following electron injection, and (b) collecting the hole from hole-transporting materials in a solid-state DSSC (Carella *et al.*, 2018; Tomar *et al.*, 2020). Most of the research in DSSC focused on boosting the short-circuit current density (J_{SC}), open-circuit voltage (V_{OC}), and fill factor (FF) to increase efficiency. Due to its appealing qualities such as high catalytic activity, low charge transfer resistance, high exchange current density, and outstanding stability towards the electrolyte redox species, platinum (Pt) is chosen as a standard material for CE in DSSCs; however, Pt is a pricey material to commercialize. Different materials, including graphite, activated carbon, platinum, carbon black, single-wall carbon nanotubes, polypyrrole, polyaniline, and poly (3,4 ethylene dioxythiophene), can be used as catalysts in DSSCs to reduce the redox coupling (Carella *et al.*, 2018; Khan, Al-Mamun, Al-Amin, *et al.*, 2017; Shaikh *et al.*, 2018).

In general, CE has to fulfill the following requirements:

- To regenerate the electrolyte rapidly and to avoid electron recombination, the mobility of electrons must be high;
- Highly stable against the corrosive electrolyte;
- It does not react with the electrolyte, so it must be chemically inert;
- Electrocatalytic properties should be high and electrical resistance should be low (Tomar *et al.*, 2020).

Because of its high catalytic activity and conductivity, Pt-coated ITO or FTO substrate has been employed as the counter electrode in DSSCs for a long time. However, because platinum is a rare and expensive metal, researchers are looking at other materials that have excellent conductivity, stability, and catalytic activity (Khan, Al-Mamun, Halder, *et al.*, 2017). Since the last decade, transition metal compounds including carbides, nitrides, and oxides (such as WO_2, WO_3, SnO_2, Nb_2O_5, TiO_2, ZrO_2, Cr_2O_3, MoO_2) due to their characteristics such as low cost, thermal stability, durability, high thermal and electrical conductivity, and most crucially, catalytic activity similar to platinum, they have been

identified as a prospective contender to replace Pt (Gnanasekar *et al.*, 2019). Due to their cost-effectiveness, environmental friendliness, availability, strong catalytic activity toward redox species, and corrosion resilience, carbon-based materials are suitable counter electrodes. Carbon black, activated carbon, mesoporous carbon, carbon nanotubes (CNTs), graphene, and fullerenes, all belonging to the carbon family, have all been investigated as possible replacements for Pt in the counter electrode, as well as composites (Khan, Al-Mamun, Halder, *et al.*, 2017; Thomas *et al.*, 2014).

Working Principle of Dye-Sensitized Solar Cell Device

The working principle of DSSC is initiated as follows:

1. The dye molecules adsorbed on the semiconductor photoanode start to absorb the solar light.
2. To generate an electric current, excited electrons are injected into the semiconductors' conduction bands (CB). The current then flows via the external wire before being collected by the CE's transparent conductive substrate.
3. The redox system regenerates the oxidized dye in the electrolyte solution.
4. The redox system is regenerated through a counter electrode.

If the energy levels of each component are appropriately aligned, an efficient electron transfer mechanism may be obtained in DSSCs. The energy level of the dye's lowest unoccupied molecular orbital (LUMO) must, for example, be higher than the CB of TiO_2, whilst the CB of the TiO_2 photoanode must be higher than the electrolyte's redox potential. Similarly, the electrolyte's redox potential must be greater than the dye's highest occupied molecular orbital (HOMO) level. The electron transport processes and energy level diagram for a complete DSSC-based Ru-complexes dye with TiO_2 photoanode, iodide/tri-iodide redox couple, and Pt counter electrode are depicted in Figure 10 (Karim *et al.*, 2019). The dye molecules move from the ground state, S, to the excited state, S*(1), or excite an electron from the HOMO level to the LUMO level when the photon is absorbed by the dye (Equation 9). The excited dye molecules will then inject electrons into the semiconductor's conduction band (CB) (2), leaving the dye in an oxidized state, S+ (Equation 10). To regenerate the dye (S), the oxidized dye (S+) obtains electrons from the reduced component of the redox couple in the electrolyte (3), and the reduced component is oxidized into the

oxidized component of the redox couple. This step is called dye regeneration (Equation 11). The oxidized species in the redox couple migrates to the counter electrode (CE) to make up for its missing electrons (4), allowing the reduced species to be regenerated by oxidized species reduction at the CE, and the circuit to be completed by electron immigration through the external load (Equation 12) (Sacco, 2017; Shaikh *et al.*, 2018).

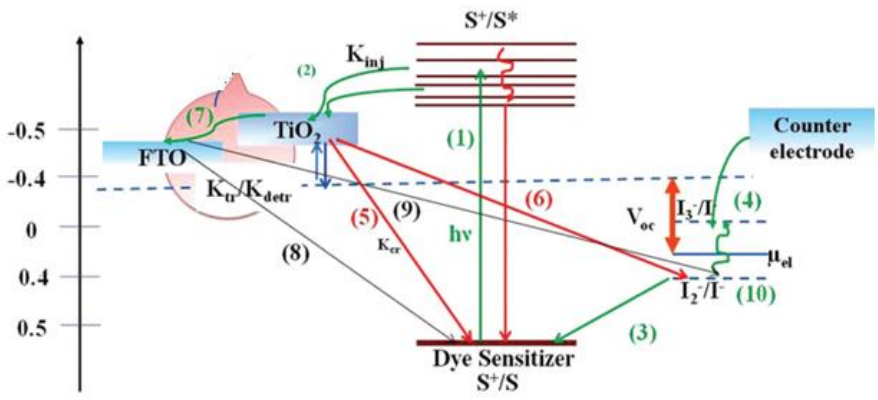

Figure 10. Electron transfer mechanisms and energy level diagram (y-axis in electron volt) of a typical DSSC (Shaikh *et al.*, 2018).

For the moment, there are other competitive reactions in the process. The electrons in TiO_2 film are taken by the oxidized species (S^+), follow-on in the recombination of oxidized species with electrons (5) (Equation 13); the other is that the electrons in TiO_2 film are captured by oxidized species of the redox couple (6), also leading to the recombination of electrons (Equation 14). In general, equations 13, 14, 16, and 17 are recombination processes that reduce the device's efficiency. Equation 15 shows electron transportation to the external circuit, and equation 18 represents redox couple regeneration (Sacco, 2017).

Photoexcitation:

$$S_{adsorbed} + h\nu \rightarrow S^*_{adsorbed} \quad (9)$$

Electron injection:

$$S^*_{adsorbed} \rightarrow S^+_{adsorbed} + e^-_{injected} \quad (10)$$

Dye regeneration:

$$S^+_{adsorbed} + \frac{3}{2} I^- \rightarrow S_{adsorbed} + \frac{1}{2} I_3^- \quad (11)$$

Electrolyte regeneration:

$$I_3^- + 2e^-_{counter\ electrode} \rightarrow 3I^-_{counter\ electrode} \quad (12)$$

Recombination by S^+ dark reaction:

$$S^+_{adsorbed} + e^-_{TiO_2} \rightarrow S_{adsorbed} \quad (13)$$

Recombination by the oxidized state of electrolyte, dark reaction:

$$I_3^- + 2e^-_{TiO_2} \rightarrow 3I^-_{anode} \quad (14)$$

Electron transportation:

$$e^-_{TiO_2} + FTO \rightarrow e^-_{FTO} + TiO_2 \quad (15)$$

Back reaction from FTO to dye:

$$e^-_{FTO} + S^+ \rightarrow FTO + S \quad (16)$$

Backreaction from FTO to electrolyte:

$$2e^-_{FTO} + I_3^- \rightarrow FTO + 3I^- \quad (17)$$

Electrolyte reduction reaction:

$$I_3^- + e^- \rightarrow 3I^- \quad (18)$$

The injected electrons go through the semiconductor before being delivered to the conductive substrate, external circuit, and counter electrode, where the electrical energy is converted to other forms of energy. The fundamental driving factor for electron transport in the mesoporous film is diffusion, which occurs due to electron concentration. Furthermore, incident light intensity is significant because higher light intensities result in faster electron diffusion.

DSSC Performance Evaluation Parameters

Short circuit current density (Jsc), open circuit voltage (Voc), energy conversion efficiency (η), and fill factor (FF) are photovoltaic characteristics used to characterize the performance of DSSCs. These values are derived from the photocurrent density-voltage (J-V) and power-voltage (P-V) curves, as illustrated in Figure 11, in which current density is plotted against voltage when the DSSC is exposed to standard AM 1.5 sunlight (100 mW cm^{-2}) (Bera *et al.*, 2021; Kumara *et al.*, 2017).

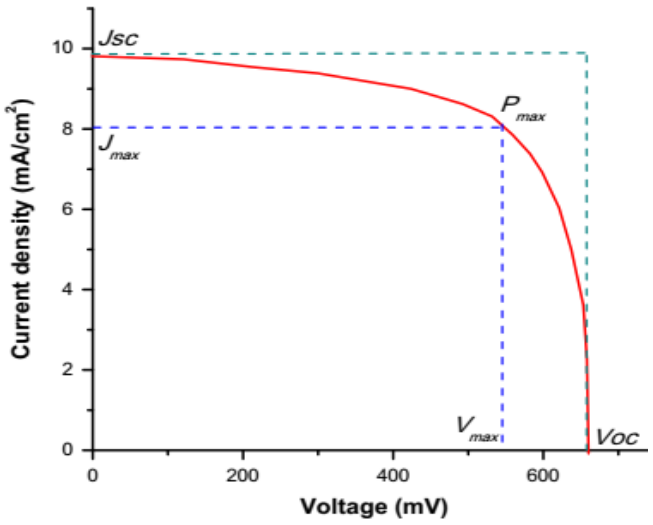

Figure 11. Current density-voltage characteristics of a silicon solar cell (Kumara *et al.*, 2017).

Open Circuit Voltage

The electrical potential difference between a cell's two terminals while the circuit is open and illuminated is known as the open-circuit voltage. The measured cell voltage in the absence of internal current flow is known as the Voc. When the resistance between the working and counter electrodes is infinite, it is the highest voltage that a solar cell can produce. This is the difference between the semiconducting oxide's Fermi level and the electrolyte's redox potential. Voc can be calculated by using Equation 19.

$$V_{oc} = \frac{E_{CB}}{e} + \frac{k_B T}{e} ln\left(\frac{n}{N_{CB}}\right) - \frac{E_{redox}}{e} \quad (19)$$

where e is the elementary charge, n is the number of the electrons in conduction band, k_B is the Boltzmann constant, T is the absolute temperature, N_{CB} is the density of accessible states in the conduction band, E_{CB} is the energy of the conduction band of the electrode (like TiO_2) and E_{redox} is the redox potential of the redox mediator(electrolyte) (Okello *et al.*, 2021).

Thus, the maximum V_{oc} of a DSSC corresponds to the difference between the energy level of the CB of TiO_2 and the redox potential of the electrolyte (I^-_3/I^-). However, the actual V_{oc} is lower than the theoretical value because of the recombination of injected electrons with dye cations and with I_3^- ions in the electrolyte (Thomas *et al.*, 2021).

Short-Circuit Current Density (Jsc).

The current per unit area ($mAcm^{-2}$) is indicated by Jsc, which is calculated for a DSSC under a short-circuit irradiation. The Jsc depends on the interaction between the semiconductor (TiO_2) and the dye sensitizer, as well as the absorption coefficient of the dye sensitizer. Consequently, a high J_{sc} is associated with the following characteristics:

1) intense light-absorption capabilities of dyes over a wide range of sunlight.
2) high electron-injection efficiencies from photoexcited dyes to the CB of TiO_2, and
3) efficient reduction of the oxidized dye by I^-.

J_{sc} can be expressed as follows (Equation 20);

$$J_{sc} = q.\eta_{lh}.\eta_{inj}.\eta_{col}.I_o \quad (20)$$

Where q is the elementary charge, η_{lh} is light harvesting efficiency, η_{inj} is the electron injection efficiency, η_{col} is the efficiency of light collection at the electrode and I_0 is the incidence of solar energy (Isah *et al.*, 2017; Robledo *et al.*, 2023; Wu *et al.*, 2015; Zhu *et al.*, 2007).

Fill Factor (FF)

The fill factor is an important parameter to evaluate the performance of a solar cell, and it is calculated as shown in Equation 21;

$$FF = \frac{P_{max}}{J_{sc}V_{oc}} = \frac{J_{max}V_{max}}{J_{sc}V_{oc}} \quad (21)$$

where, P_{max} is the maximum power output and J_{max} (mA/cm^{-2}) and V_{max} (V) are the current density and voltage at the point of maximum power output in the J-V curves, respectively, as shown in Figure 11. Thus, the maximum value of FF is unity (Chatterjee, 2018; Isah *et al.*, 2017; Kumar *et al.*, 2019; Kumara *et al.*, 2017).

Solar Energy to Electrical Power Conversion Efficiency (PCE)

The overall power-conversion efficiency (η) measures the efficiency of converting incident light into electrical energy. It is the ratio of the maximum electrical power and the energy of incident sunlight (P_{in}) and is calculated according to Equation 22, using the parameters obtained from the J-V plot (Figure 11).

$$\eta\% = \frac{P_{max}(mWcm^{-2})}{P_{in}(mWcm^{-2})} x100\% = \frac{J_{sc}(mAcm^{-2}).V_{oc}(V).FF}{P_{in}(mWcm^{-2})} x100\% \quad (22)$$

Hence, to get the maximum value of η, Jsc, Voc, and FF of the cell needs to be optimized (Kumar *et al.,* 2019; Wu *et al.*, 2015).

Incident Photon to Current Conversion Efficiency (IPCE)

The IPCE, also known as external quantum efficiency (EQE), is defined as the number of electrons flowing through the external circuit, divided by the number of incident photons. IPCE can be represented by Equation 23.

$$IPCE\% = \frac{n_{electrons}}{n_{photons}} = \frac{J_{ph}/e}{I/hv} = \frac{J_{ph}xhc}{Ixe\lambda} = \frac{1240\ (eVnm)xJ_{ph}(mAcm^{-2})}{\lambda(nm)xI(mAcm^{-2})} \quad (23)$$

Where J_{ph} is the short-circuit photocurrent density generated under monochromatic light illumination, λ and I are the wavelength and intensity of the incident light, respectively. e is the elementary charge, h is Planck's constant (6.626×10^{-34}Js), ν is the frequency of monochromatic light, and c is the speed of light in vacuum (Kumara *et al.*, 2017; Thomas *et al.*, 2021).

3 MATERIALS AND METHODS

3.1 Chemicals and Reagents

The chemicals and reagents used in this work were deionized water, titanium tetra isopropoxide (96%, Sigma Aldrich, Germany), carbon tetrachloride (99.9%, Alpha Chemika, India), isopropanol (96%, Alpha Chemika, India), sodium hydroxide (98%, Luba, India), sulphuric acid (98%, Loba Chemie, India), zinc (II) acetate dihydrate (99%, UNI-CHEM, India), copper(II) nitrate trihydrate (96%, Alpha Chemika, India), silver nitrate (99%, Nanjing, China), acetone (99%, Alpha Chemika, India), lead acetate (99%, SLR, India), hydrochloric acid (37%, Alpha Chemika, India), triton X-100 (99%, Sigma Aldrich, USA), chloroform (97%, SLR, India), ethylenediaminetetraacetic acid disodium (99.5%, SRL, India), sodium sulphate (97%, Sigma Aldrich, Germany), HI-30 iodolyte (Solaronix, Switzerland), platinum coated counter electrode (Solaronix, Switzerland), ethanol (99.8% Alpha Chemika, India), acetonitrile (99%, Alpha Chemika, India), transparent TiO_2 (Ti-Nanoxide T/SP) paste, and reflective TiO_2 (Ti-Nanoxide R/SP) paste (Solaronix, Switzerland). All the chemicals and reagents are used as received without further purification.

3.2 Instruments and Apparatus

Thermal analyzer (DTG-60H Shimadzu Co., South Korea), FTIR-6600 spectrophotometer (JACO International Co., Ltd., Tokyo, Japan), X-ray diffractometer (Shimadzu 7000, Japan), Raman spectrophotometer (JASCO, NRS-5000, Japan), ultraviolet-visible spectrophotometer (JASCO V-750 UV-Vis, Tokyo, Japan), potentiostat (Autolab, EcoChemie, Netherlands) electrochemical workstation, solar simulator (16S-Series 150-300W, Germany), scanning electron microscope (400, FEG, USA), transmission electron microscope (FEI, Titan, 80–300 kV, USA) were used in this work.

3.3 Sample Collection

The fresh part of the plants of *Impatiens rothii Hook. f.* leaf (IHL), flowers (IHF) and root (IHR), *Thymus schimperi Ronnige* flowers (TRF), and *Rumex nepalensis Spreng* flowers (RSF) (Figure 12) were collected from Menz Gera-midir Woreda, North Shewa Zone, Amhara Region, Ethiopia.

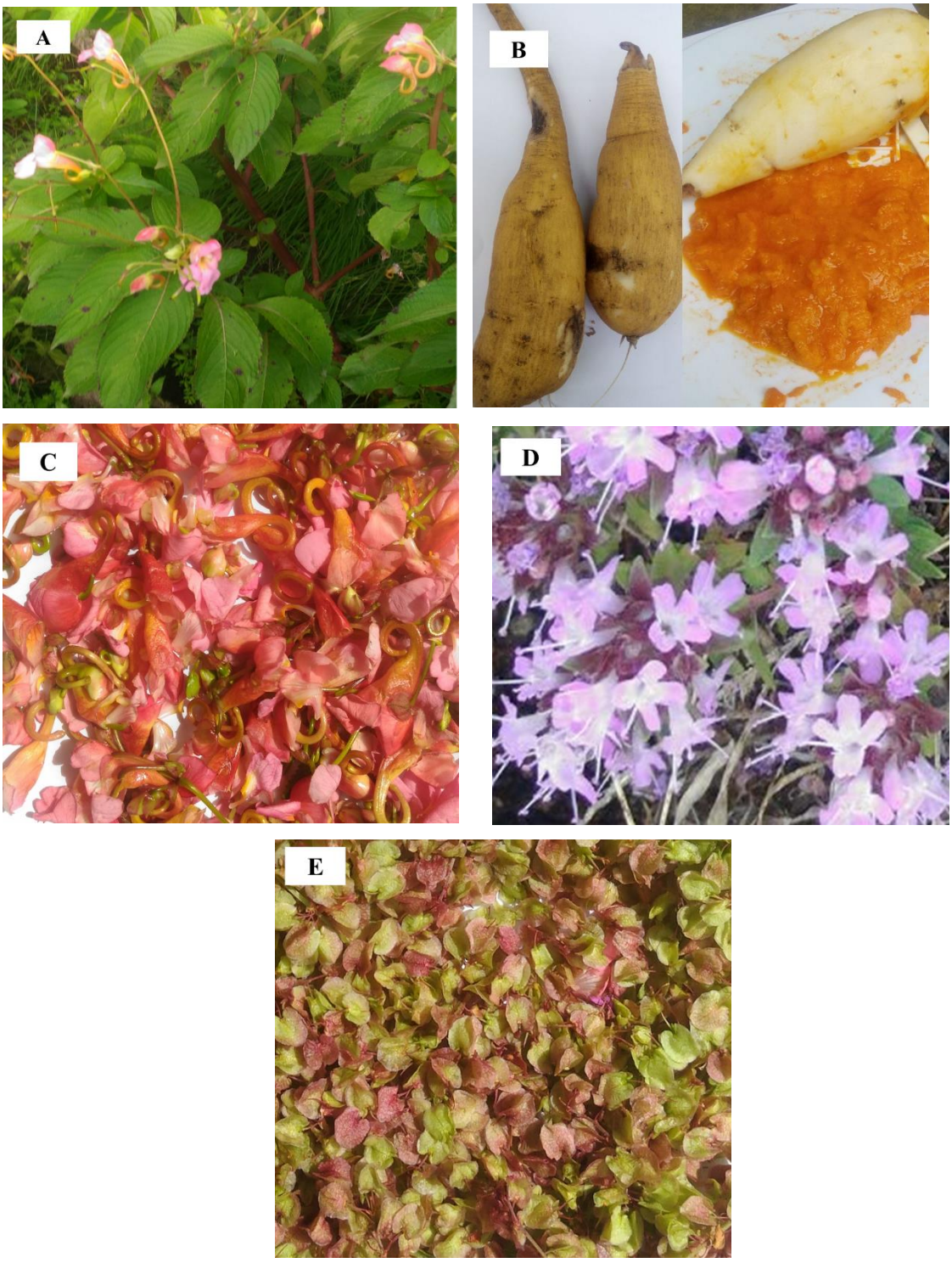

Figure 12. Photo of (A) IHL, (B) IHR, (C) IHF, (D) TRF and (E) RSF.

3.4 Experimental Procedures

3.4.1 Preparation and Extraction of Plant Parts

Preparation of plant parts for extraction

The natural dyes used in the DSSC as light absorbers (IHR, IHF, TRF, RSF) and the IHL to synthesize metal oxide nanomaterials were collected from the garden and washed with deionized water. The washed parts were dried in the dark for two weeks (Ortiz-Quiñonez & Pal, 2024). Then the dried plant parts were ground using an electrical grinding machine and stored in plastic bags for further use.

Extraction of IHL for Nanomaterials Synthesis

The extraction was done following the method reported by Basit and his co-authors (Basit *et al.*, 2023). 20 g of IHL powder was placed into a 1000 mL Erlenmeyer flask containing 500 mL deionized water and boiled at 60 °C for 4 hr while stirring magnetically at 600 rpm. The resulting extracted solution was allowed to cool to room temperature and was filtered using Whatman filter paper No. 1 (Chatterjee, 2018; El-Ghamri *et al.*, 2015; García-Salinas & Ariza, 2019). The schematic representation of the extraction procedure is shown in Figure 13.

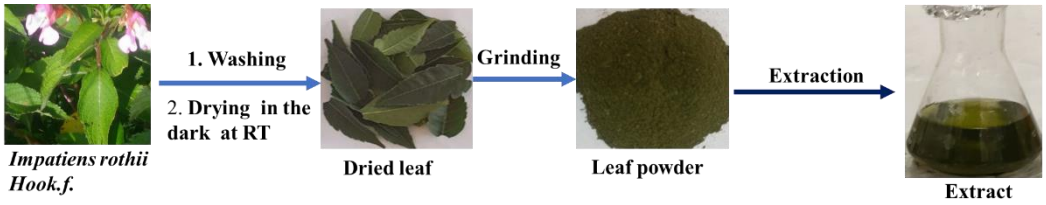

Figure 13. Schematic representation of plant leaf extraction procedure.

Extraction of dyes from plants' roots and flowers for photosensitization

Natural dye solutions were extracted from TRF, IHR, IHF, and RSF using a mixture of ethanol and deionized water (water: ethanol; 80:20) (Peev *et al.*, 2011). 10 g of the ground powder of TRF was placed into a 250 mL Erlenmeyer flask containing 100 mL of deionized water (w) (Step 1). The mixture was stirred magnetically for 24 hr in the dark (Ardeshirfard & Elhamifar, 2023), the extracted dye was filtered, and the filtrate was used for photoanode sensitization. The same procedure was followed to prepare an extract of TRF with a mixture of 20 mL ethanol and 80 mL DI water (mix) (Step 2). Similar steps

were followed to prepare dye extracts of IHR, IHF, and RSF. Figure 14 shows a schematic representation of the extraction of the natural dye sensitizer from TRF.

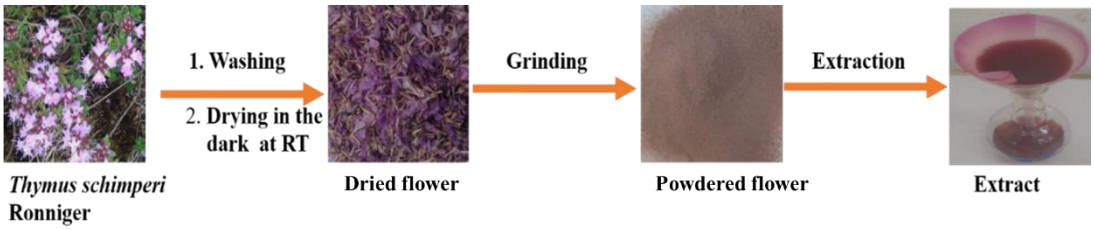

Figure 14. Schematic representation of the extraction of dye solution from TRF.

3.4.2 Phytochemical Screening Test

The aqueous extracts of plants were used for phytochemical tests to identify the chemical composition of IHL, TRF, IHR, IHF, and RSF using standard methods (Dahanayake *et al.*, 2019).

Test for Alkaloids

A 2 mL of the extract was treated with a few drops of Wagner reagent, and the formation of a yellowish color is an indication of the presence of alkaloids (Dahanayake *et al.*, 2019).

Test for Flavonoids

In a 2 mL concentrated extract 1 mL of 10% NaOH solution was added and the formation of an intense yellow color indicates the presence of flavonoids (S. Ali *et al.*, 2018).

Test for Proteins

In a dry test tube, 2 mL of the extract was taken and few drops of concentrated HNO_3 solution was added drop wisely. The formation of a yellow color shows the presence of proteins (Dubale *et al.*, 2023).

Test for Phenols

About 2 mL of the plant extract was taken into a test tube, and 3 drops of 3% $FeCl_3$ were added. The formation of a dark green color confirms the presence of phenolic compounds (Oloya *et al.*, 2022).

Test for Saponins

Plant extract (2 mL) was treated with a few drops of 1% lead acetate solution. The formation of white precipitates indicates the presence of Saponins (Saha *et al.*, 2020).

Test for Steroids

About 2 mL of extract was taken into a test tube, and 1 mL of chloroform was poured into it. About 2 mL of acetic anhydride and 0.5 mL of concentrated H_2SO_4 was added to the test tube dropwise. The solution was shaken slowly, and the formation of a red color in the upper layer of the test tube indicated the presence of steroids (Agidew, 2022).

Test for Tannins

About 3 mL of aqueous plant extract solution was taken into a test tube, followed by 4 drops of 1% lead acetate solution. The formation of a yellowish precipitate indicates the presence of tannins (Dahanayake *et al.*, 2019).

Test for Terpenoids

A 2 mL of plant extract was taken into a test tube, and 1 mL of chloroform was added. Then, 1 mL of concentrated H_2SO_4 was added dropwise into the test tube and shaken slightly. The formation of a yellow color in the lower portion indicates the presence of terpenoids (Mabadahanye *et al.*, 2022).

3.4.3 Green Synthesis of Nanomaterials and Nanocomposites

3.4.3.1 Green Synthesis of TiO_2 NPs

To synthesize pure TiO_2 NPs, 15 mL of titanium (IV) isopropoxide (TTIP) was used as the precursor salt. To evaluate the effect of plant extract concentration, the volumes of plant extracts added were 25 mL, 50 mL, and 75 mL. The TTIP was dissolved in 50 mL of ethanol, then 25 mL of the plant extract was added to the precursor solution and left for homogenization, and stirred for 12 hr. After the yellowish precipitate formation, the mixture was further allowed to stand overnight for stabilization. The precipitate was filtered by Whatman filter paper no. 1 and washed 3 times with deionized water and twice with ethanol. The precipitate was dried at 80 °C for 3 hr in a hot air oven (Bopape *et al.*, 2023). The same steps were followed for the 50 mL and 75 mL extracts. The dried powder samples were ground using a mortar and pestle, and the synthesized NMs were calcined at 500 °C for 3 hr in a muffle furnace with a heating rate of 10 °C/min as shown in Figure 15.

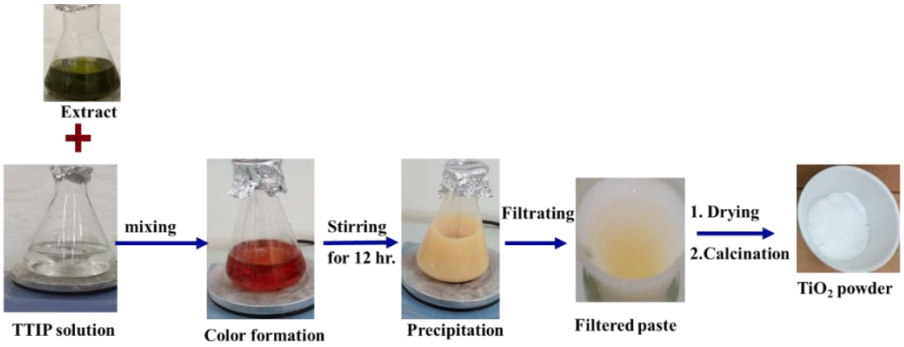

Figure 15. Schematic representation of green synthesis of TiO_2 NPs.

3.4.3.2 Green Synthesis of TiO_2/CuO NCs

TiO_2/CuO NCs were synthesized based on optimization in section 3.4.3.1. The IHL extract was fixed to 50 mL and the TTIP to copper nitrate trihydrate solution ratio was varied as 1:2, 1:1, and 2:1, and the total volume of these precursors was fixed to 15 mL. To prepare 0.2 M of copper nitrate trihydrate solution, 4.8 g of its salt precursor was added to 100 mL of DI water, and completely dissolved by mechanical shaking. Then 5 mL of 0.2 M copper nitrate trihydrate solution was poured into a 250 mL Erlenmeyer flask containing 50 mL ethanol, followed by the addition of 10 mL of TTIP. Then 50 mL of plant extract was added while magnetically stirring the mixture, and the system was stirred for 12 hr. The mixture was allowed to stand overnight for stabilization. The precipitate was filtered by using Whatman filter paper no. 1, washed 3 times with deionized water, and twice with ethanol, and dried at 80 °C for 3 hr in a hot air oven (Bopape *et al.*, 2023). The same steps were followed to synthesize the 1:1 and 2:1 ratio of precursors. The dried samples were calcined at 500 °C for 3 hr (Ahmad *et al.*, 2020; Aravind *et al.*, 2021b; Muniz *et al.*, 2011).

3.4.3.3 Green Synthesis of TiO_2/ZnO Nanocomposites

To synthesize TiO_2/ZnO NCs, a 0.2 M zinc solution was prepared by dissolving 4.4 g of zinc acetate dihydrate salt in 100 mL of DI water. Then, the same procedure was followed in Section 3.4.3.2, using a zinc acetate precursor in place of copper nitrate.

3.5 Characterization Techniques

3.5.1 TGA/DTA Study

The thermogravimetric analysis/differential thermal analysis (TGA/DTA) curve was obtained on the thermal analyzer (DTG-60H Shimadzu Co., South Korea) instrument in a

temperature range of 25 ℃ to 800 ℃ at a heating rate of 10 ℃ /min for TiO_2 NPs. A sample size of 10 mg was taken, and TGA/DTA analysis was performed (Lal *et al.*, 1998).

3.5.2 X-ray Diffraction Study

The crystal structure and phase of the green synthesized nanomaterials were analyzed by X-ray diffraction (XRD) technique using Shimadzu 7000 X-ray diffractometer (Japan) equipped with Cu Kα1 radiation source (λ = 1.5406 Å) with an accelerating voltage of 40 kV and a source current of 30 mA at a scanning rate of 4° min^{-1} in 2θ range of 10 ° to 80 °. A 100 mg powder sample was taken for characterization. The crystallite size (D) of synthesized NPs was determined by using the Scherrer equation (Equation 27).

$$D = \frac{K\lambda}{Bcos\theta} \tag{27}$$

where λ is the wavelength of incidence X-ray, K is a constant taken from the x-ray wavelength of radiation (0.9), B is the full-width at half-maximum intensity (FWHM), and θ is the diffraction angle in radians (Tahir *et al.*, 2018; Velázquez-Martínez *et al.*, 2019).

3.5.3 Ultraviolet-Visible Diffuse Reflectance Spectroscopic study

The optical property and dye absorbance were recorded on a UV-Vis diffused reflectance spectrophotometer (JASCO V-750 UV-Vis). An amount of 50 mg of each synthesized powder was well-grounded with 1 g of $BaSO_4$, and spread onto the sampling plate (Ramakrishnan *et al.*, 2012). The background reflectance of $BaSO_4$ was measured before the sample measurement.

3.5.4 Fourier Transform-Infrared Spectroscopic Study

The samples for measurement were prepared by mixing the powder of the samples with KBr in a 5 to 95 ratio, forming a homogeneous paste, and then the resulting paste was molded into pellets (T. K. Shah *et al.*, 2019). The functional groups found in the synthesized materials were recorded using an FTIR-6600 spectrophotometer (JACO International Co., Ltd., Tokyo, Japan) in the range of 4000-400 cm^{-1}.

3.5.5 Photoluminescence

The synthesized powder sample was prepared by dissolving 4 mg in 20 mL ethanol and sonicated for 30 min to make a homogeneous suspension. Then, 4 mL of sample from the

suspension solution was taken into the quartz cuvette, and the photoluminescence emission spectra were recorded by a fluorescence spectrophotometer (Agilent Cary Eclipse Fluorescence Spectrophotometer) using a 150 W xenon lamp as the excitation source. at the excitation wavelength corresponding to the absorption wavelength of 390 nm (El-Awady *et al.*, 2022).

3.5.6 Scanning Electron Microscopy/Energy-Dispersive X-ray Spectroscopic Study

Energy dispersive spectroscopy attached to SEM was used to analyze the elemental composition. The samples for SEM image measurement were prepared by dispersing about 3 mg of sample powder was dispersed in 15 mL of ethanol and sonicated for 20 min. A few drops of the resulting suspension were placed on the glass slide with carbon tape and allowed to air dry. Then the slides were used for the surface morphology and elemental composition of TiO_2 NPs, TiO_2/CuO NCs, and TiO_2/ZnO NCs study using by SEM/EDX technique. (Nguyen *et al.*, 2013).

3.5.7 Transmission Electron Microscopic (TEM) Studies

The samples were mounted on a copper grid using a drop of ethanol. Then the copper grids were dried and loaded into the microscope holder for TEM micrograph analysis utilizing a TEM operating voltage of 300 kV (FEI, Titan, 80–300 kV) (Kuei *et al.*, 2020). The samples underwent focused ion beam (FIB) milling to create thin sections to allow electron transmission.

3.5.8 X-Ray Photoelectron Spectroscopic (XPS) Studies

To conduct XPS analysis, the powder of each synthesized nanomaterial sample (2 mg) was mixed with 15 mL of DI water and sonicated for 20 min. Then a few drops of the resulting suspension were placed on the glass slide and allowed to air-dry. Finally, the dried sample on the slide was used for the XPS measurement using a Kratos Axis DLD x-ray photoelectron spectrometer (Shimadzu, Canada), with Al Kα (hν = 1486.6 eV, 37 mA) monochromatic incident radiation (Atış *et al.*, 2024; Li *et al.*, 2024).

3.5.9 Surface Area Analysis

To measure the surface area and pore size distribution, standard (Brunauer-Emmett-Teller (BET) surface area analysis and Barrett-Joyner-Halenda (BJH) pore size and volume analysis were employed using Quantachrome v11.02, USA instrument. The powder

samples were dried at 110 °C to remove moisture adsorbed on sample surfaces. Then, the samples were placed in the degassing chamber of the BET instrument and degassed at 300 °C under vacuum conditions to remove impurities, after which they were cooled to -196 °C (77 K). After degassing, 0.40 g of the sample was taken into the sample holder of the BET apparatus. Then the adsorption measurement was done by introducing Nitrogen gas incrementally, and the pressure was measured at each step. Finally, the desorption measurement was performed gradually by reducing the pressure and measuring the amount of gas released (Matshitse, 2010).

3.5.10 Electrochemical Studies

The electrochemical measurements were conducted using a potentiostat (Autolab, EcoChemie, Netherlands) electrochemical workstation, which was carried out with a three-electrode electrochemical cell with Ag/AgCl reference electrode (saturated), platinum wire counter electrode, and FTO coated with the catalyst sample as working electrode, while 0.1 M Na_2SO_4 was used as a supporting electrolyte. Mott-Schottky analyses were conducted over the range of -1.0 V to 1.5 V at a frequency of 1000 Hz. Similarly, an electrochemical impedance spectroscopic (EIS) study was carried out with an amplitude of 5 mV over the frequency region ranging from 100 kHz to 0.01 Hz (Atış *et al.*, 2024).

3.6 Photocatalytic performance test

The photocatalytic degradation activity of green synthesized TiO_2 NPs, TiO_2/CuO, and TiO_2/ZnO NCs against MB dye was tested under a 150 W tungsten-halogen lamp (320-2400 nm, Philips, China). An amount of 60 mL aqueous solution of MB (5–20 ppm) was prepared in vessels, and an appropriate amount of the catalyst (10 – 40 mg) was added. The solution was sonicated in the dark for 10 min and allowed to stand for 30 min before irradiation for adequate adsorption-desorption equilibrium. In every 10 min interval, 4 mL of MB solution was taken from the reaction mixture, and absorbance was measured by UV-Vis spectrophotometer (Ali, 2022).

The point of zero charge (pH_{PZC}) was determined using the salt addition method (Bakatula et al., 2018). An amount of 50 mL of 0.01 M aqueous solution of KNO_3 was added to ten separate Erlenmeyer flasks. Then 10 mg of the photocatalyst was added to each solution, and the initial pH was adjusted to 3-12 using 0.1 M NaOH and 0.1 M HCl. The same

procedure was followed to determine the pH_{PZC} for TiO_2/CuO and TiO_2/ZnO (Al-Maliky *et al.*, 2021). Then, based on pH_{PZC} value, photocatalytic activities were performed at different pH levels (7-10). The pH values were adjusted by adding 0.1 M NaOH solution.

The trapping experiments were conducted to investigate the main active species involved in the photocatalytic degradation of MB using TiO_2 NPs, TiO_2/CuO, and TiO_2/ZnO NCs. In the experiment, the scavengers used were $AgNO_3$, ethylenediaminetetraacetic acid disodium (EDTA) (Bakry *et al.*, 2022), isopropanol (IPA) (Salesi & Nezamzadeh-Ejhieh, 2023) and acetonitrile (Saharudin *et al.*, 2018) for e^-, h^+, $OH^\bullet$, and $O_2^{-\bullet}$, respectively, to quantify the relative contribution of reactive species. In the experiments, 1 mmol of scavenger was added to the dye solution with an optimized dose of photocatalyst.

The photocatalytic performance of TiO_2 NPs, TiO_2/CuO, and TiO_2/ZnO NCs was evaluated in terms of removal efficiency and reaction kinetics. The percent removal of MB dye by the synthesized nanomaterials was calculated using the formula in Equation 24 (Basit *et al.*, 2023).

$$\%Degradation = \frac{C_o - C}{C_o} \times 100 = \frac{A_o - A}{A_o} \times 100 \quad (24)$$

Where C_0 and A_0 are dye concentration and absorbance, respectively, before irradiation. The parameters C and A are the concentration of MB dye and its absorbance respectively, at any time t after the irradiation started. The rate constant of the photocatalysis was determined using the pseudo-first-order ($\ln(C_o/C_t)$ vs t) (Equation 25) and the pseudo-second-order ($1/C$) vs t) kinetic models (Equation 26).

$$ln\left(\frac{C_o}{C_t}\right) = kt \quad (25)$$

$$\frac{1}{C_t} - \frac{1}{C_o} = kt \quad (26)$$

C_o and C_t are initial concentrations of MB dye at the start of photocatalysis and after a given time t, respectively. The rate constant k was obtained from the slope of the curve $\ln(C_o/C_t)$ against t (Akerdi *et al.*, 2020; Guo *et al.*, 2023).

3.7 Optimization of Process Parameters

Multiple experiments were run to modify various parameters to move forward with the finer outcomes. Experiments with varying volumes of plant extract added to TTIP

precursor, ratios of precursors, catalyst doses, the concentration of pollutant dye, pH values, and other factors were conducted at room temperature. The TTIP: extract volume ratio was 15 mL: 25, 50, 75 mL, and the photocatalytic performance of a 15:50 mL ratio showed better performance, and 50 mL of plant extract was selected as the optimum volume for the synthesis of TiO_2/CuO, and TiO_2/ZnO NCs. To optimize TTIP: CuO or ZnO precursor, the total volume of precursor was fixed to 15 mL, and the ratios were prepared in such a way that 1:2, 1:1, and 2:1 (TTIP: 0.2 M CuO or ZnO precursor). The photocatalytic performance of the 1:1 TTIP: CUO precursor ratio was found to be optimum. Then, using this optimum ratio, other parameters were optimized (Behera *et al.*, 2023).

3.8 Reusability Test

The reusability tests were done after being used in the photocatalytic degradation of MB. Catalyst recovery was performed at the end of each cycle by centrifuging the reactant mixture at 5000 rpm for 15 min to separate the catalyst from the supernatant solution and washed using deionized water and ethanol 3 times. Finally, the residue was dried at 70 $°C$ for 8 hr and used again in the next step of the experiment (Behera *et al.*, 2023; Rusman *et al.*, 2021; Sundaram *et al.*, 2019). This procedure was repeated for three consecutive cycles of photocatalysis using fresh MB dye.

3.9 Preparation of photoanodes

3.9.1 Preparation of T/R photoanodes

FTO glass substrates were first cleaned in an ultrasonic bath using DI water, isopropanol, and acetone for 5 minutes in each solvent. The transparent TiO_2 nanoparticles paste (Ti-Nanoxide T/SP) was coated over the conductive side of FTO glass substrates uniformly by the doctor blade technique (S. A. Abrol *et al.*, 2021). The coated FTO glass substrates were heated at 120 ℃ for 30 minutes and cooled down. After cooling, the reflective TiO_2 nanoparticles paste (Ti-Nanoxide R/SP) was coated over the transparent films, and again the coated glass substrates were heated at 120 ℃ for 30 minutes. These doubly coated films were calcined at 450 ℃ for 40 minutes at the rate of 10 ℃ min^{-1} (Sullivan *et al.*, 2022). The detailed procedure is shown in Figure 16.

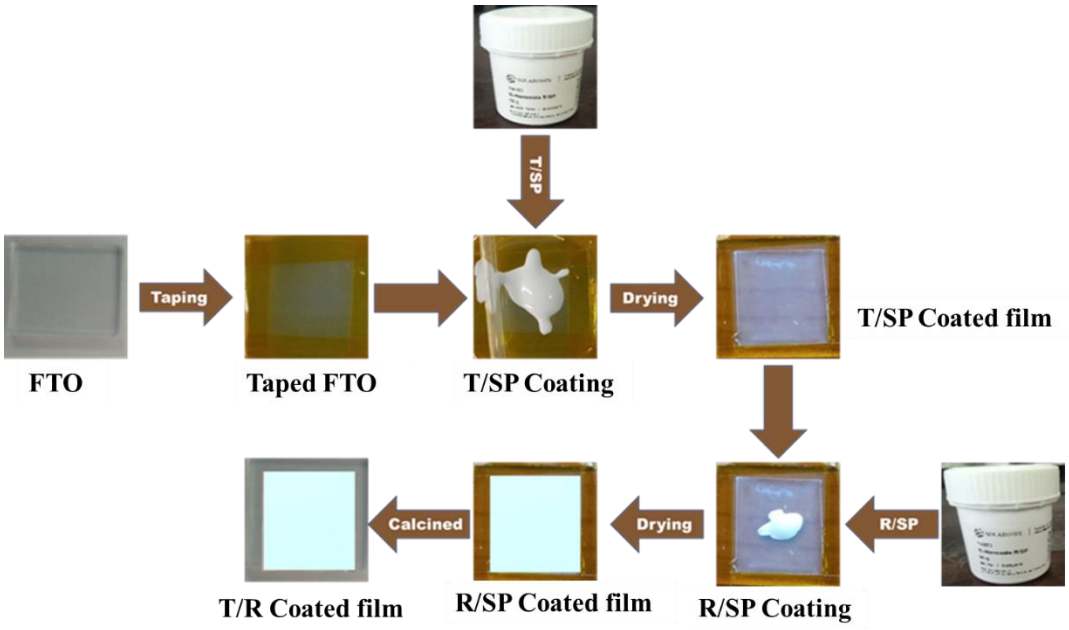

Figure 16. Schematic representation of the T/SP-R/SP photoanode preparation.

3.9.2 Preparation of TiO_2, TiO_2 /CuO (1:1) and TiO_2 /ZnO (1:1) NCs photoanodes

FTO glass substrates were first cleaned in an ultrasonic bath using DI water, isopropanol, and acetone for 5 minutes in each solvent. An amount of 2 g of TiO_2 was taken into the crucible. 2 mL of Triton X-100 and 0.5 mL of Nafion binders were added to the TiO_2 and mixed well using the glass rod to produce a uniform paste. The prepared paste was coated over the conductive side of FTO glass substrates by the doctor blade technique (S. A. Abrol *et al.*, 2021; Prakash *et al.*, 2022). The coated FTO glass substrates were heated at 120 ℃ for 30 minutes in an oven and cooled down. After cooling, the films were calcined at 450 ℃ for 40 min at a heating rate of 10 ℃ min^{-1} (Sullivan *et al.*, 2022; Zhang *et al.*, 2024). The steps were repeated for TiO_2 /CuO and TiO_2 /ZnO NCs.

3.10 Sensitization of photoanodes

The calcined photoanodes were immersed in the Petri dish containing filtered extracted dye solution for 24 hrs. The immersed photoanodes were taken from the solution and rinsed with the solvent from which the extract was prepared (Sowmya *et al.*, 2021).

3.11 DSSC Device Fabrication and Performance Test

Using the dyed photoanodes and the platinum-coated counter electrodes, DSSCs were assembled by sandwiching the two electrodes together in such a way that they faced the

conductive faces by binder clips. The redox electrolyte (HI-30 Iodolyte) was injected into the cell through the back-drilled counter electrode using a syringe (Sowmya *et al.*, 2021). The J-V measurements of fabricated cells were carried out under the illumination of a Keithley 2450 source meter with AM 1.5 G spectrum and calibrated irradiance of 100 mW/cm^2.

4 RESULTS AND DISCUSSION

4.1 Analysis of Extracts

4.1.1 Phytochemicals Screening Analysis

All selected plant extracts showed notable positive phytochemical screening results except water extract flavonoids in TRF and RSF, saponins in TRF and RSF, and tannins in IHL

and IHR (Table). Phytochemical screening helps identify bioactive compounds, such as flavonoids, anthocyanins, carotenoids, and tannins, which can serve as effective sensitizers in DSSCs (Aly *et al.*, 2019) .

Table 6. Summary of phytochemicals screening results for IHL, TRF, IHL, IHR, and RSF of crude extracts.

Phytochemicals	IHL	IHR		IHF		TRF		RSF	
	w	w	mix	w	mix	w	mix	w	mix
Alkaloids	+	+	+	+	+	+	+	+	+
Flavonoids	+	+	+	+	+	-	+	-	+
Proteins	+	+	+	+	+	+	+	+	+
Phenols	+	+	+	+	+	+	+	+	+
Saponnins	+	+	+	+	+	-	+	-	+
Steroids	+	+	+	+	+	+	+	+	+
Tannins	-	-	+	+	+	+	+	+	+
Terpenoids	+	+	+	+	+	+	+	+	+

'-' absence, '+' presence, 'w' Deionized water, 'mix' mixture of ethanol (20%) and deionized water (80%) used for extraction.

4.1.2 UV-Vis Analysis of the Dye Extracts

The UV-Vis spectroscopic technique was used to evaluate the optical properties of extracted dye solutions. The solutions showed different absorption peaks due to the presence of various phytochemical constituents. The peaks at about 630 and 750 nm are attributed to chlorophyll a and b, respectively. Other peaks at 340, 383,413, 466, and 536 nm are due to the presence of anthocyanins and flavonoids (Figure 17). (Alami *et al.*, 2019). Flavonoids, a diverse group of polyphenolic compounds, exhibit distinct UV-Vis absorbance characteristics due to their chemical structure, which includes multiple aromatic rings and conjugated double bonds. The UV-Vis absorbance range of flavonoids is 270-520 nm (Taniguchi *et al.*, 2023). Carotenoids typically exhibit strong UV-Vis absorption in the range of 400 to 500 nm. The exact absorption maxima can vary based on the specific type of carotenoid: Beta-Carotene (450–480 nm), Lutein (420–460 nm), Lycopene (470-500 nm), reflecting its deep red color (Chazaux *et al.*, 2022).

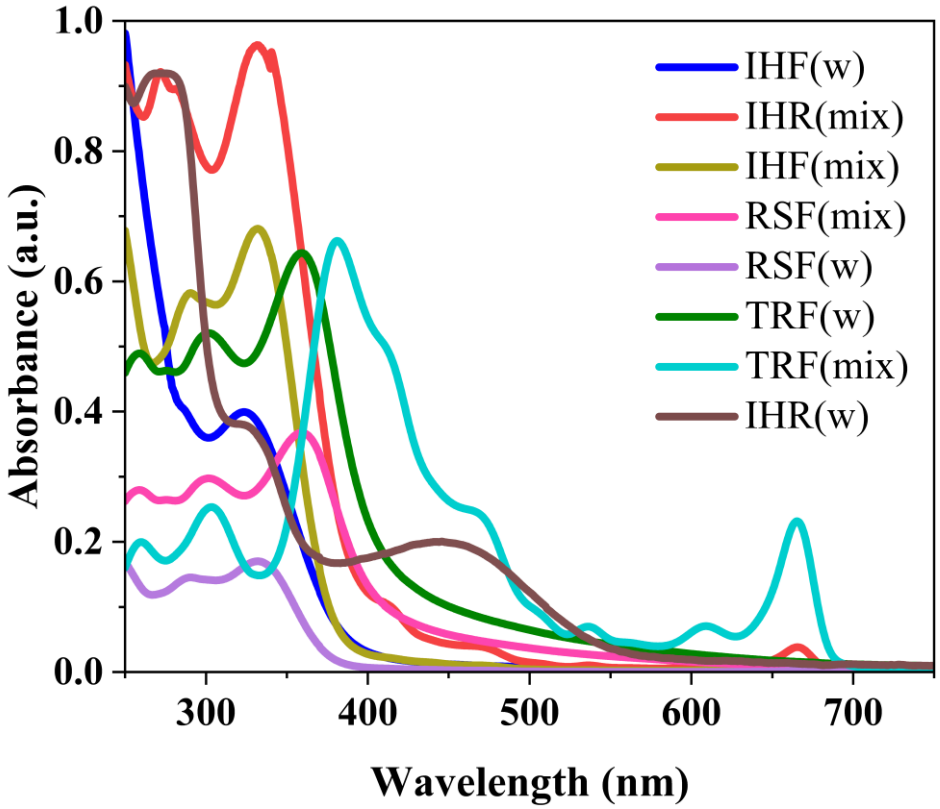

Figure 17. The UV-Vis absorption spectra of dye extracts of IHF(w), IHF(mix), IHR(W), IHR(mix), TRF(w), TRF(mix), RSF(w), and RSF(mix).

4.1.3 FTIR Analysis of Dye Extracts

The FTIR spectra of dye extracts were measured in the range of 4000–400 cm^{-1} (Figure 18). The peaks in the range of 3400–3100 cm^{-1} confirm the presence of hydroxyl group stretching, which is a characteristic property of polyphenolic molecules (Wongsa *et al.*, 2022). The broad band absorption peaks between 3500 - 3000 cm^{-1} indicate the presence of more intermolecular hydrogen bonding in the case of IHF(mix), RSF(w), TRF(mix), and RSF(mix) (Azmi & Fatmiyah, 2021). The peaks in the range of 2975–2940 cm^{-1} indicate the presence of -CH, $-CH_2$, and $-CH_3$ stretching vibrations (Park *et al.*, 2015). The presence of one or more aromatic rings in the chemical structure of a compound is confirmed by the vibrations associated with the C–H and C=C–C rings. The bands in the 1615–1580 cm^{-1} region confirm the presence of the C–H and C=C–C aromatic bonds stretching (Wittkamp *et al.*, 1997). Besides, at approximately 1200 cm^{-1}, the phenolic C–O bending vibration is observed (Ninnes *et al.*, 2024).

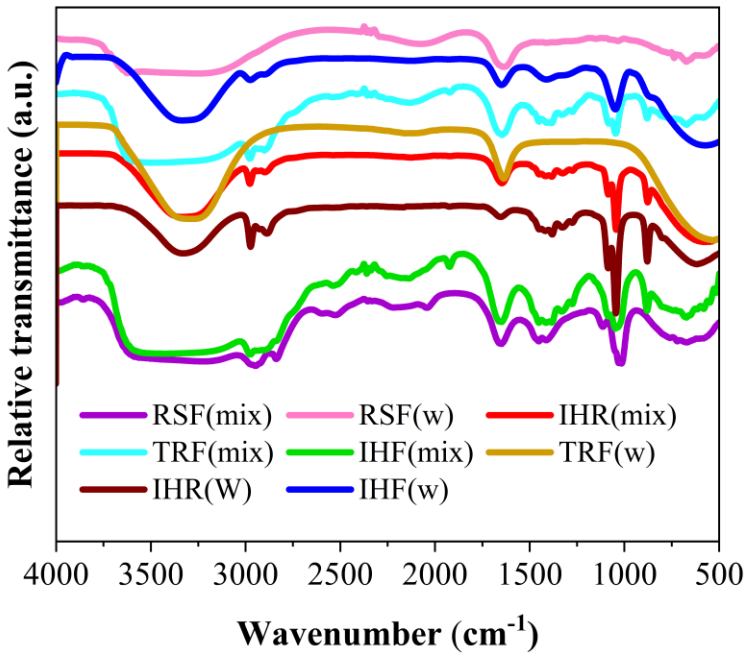

Figure 18. FTIR absorption spectra of dye extracts of IHF(w), IHF(mix), IHR(W), IHR(mix), TRF(w), TRF(mix), RSF(w), and RSF(mix).

4.2 Green Synthesized Nanomaterial Analysis

4.2.1 TGA/DTA Analysis

The thermal decomposition property of green synthesized TiO_2 NPs, TiO_2/CuO NCs, and TiO_2/ZnO NCs before calcination was evaluated between 25 ℃ and 800 ℃. The TGA curve shows three main mass loss steps. In the case of TiO_2 NPs (Figure 19A), the first 6% weight loss between 36 °C and 150 °C temperature range is associated with the decomposition of adsorbed water (Abbasi *et al.*, 2016). The second approximately 5% mass loss observed between 180 and 420 °C is attributed to the volatilization of organic matters from TTIP precursors and plant extract, the transformation of amorphous structure to crystalline form, as well as the elimination of chemisorbed hydroxyl groups (Kučerík *et al.*, 2018). The third weight loss in the temperature range of 580–610 ℃ and exothermic peaks at 590 ℃ can be attributed to the phase transformation of anatase to rutile polymorph (Zhu *et al.*, 2018). Similarly, the TGA curve for TiO_2/CuO NCs (Figure 19B) shows about 4.5% weight loss, which is attributed to the evaporation of surface adsorbed water in the temperature range of 26-150 °C. The second weight loss from 180-340 °C is due to the removal of chemically adsorbed water and some organic matter from the plant extract,

which accounts for about 6% of weight loss. The TGA curve is almost constant from 400-600 °C, which is used to determine the calcination temperature (Zhu *et al.*, 2018). The TGA curve for the thermal analysis of TiO_2/ZnO NCs shows about 4% weight loss in the temperature range of 25-180 °C (Figure 19C). It shows stability in the temperature range of 400-600 °C. From the TGA/TDA analysis of TiO_2 NPs, TiO_2/CuO NCs, and TiO_2/ZnO NCs, the calcination temperature was taken as 500 °C.

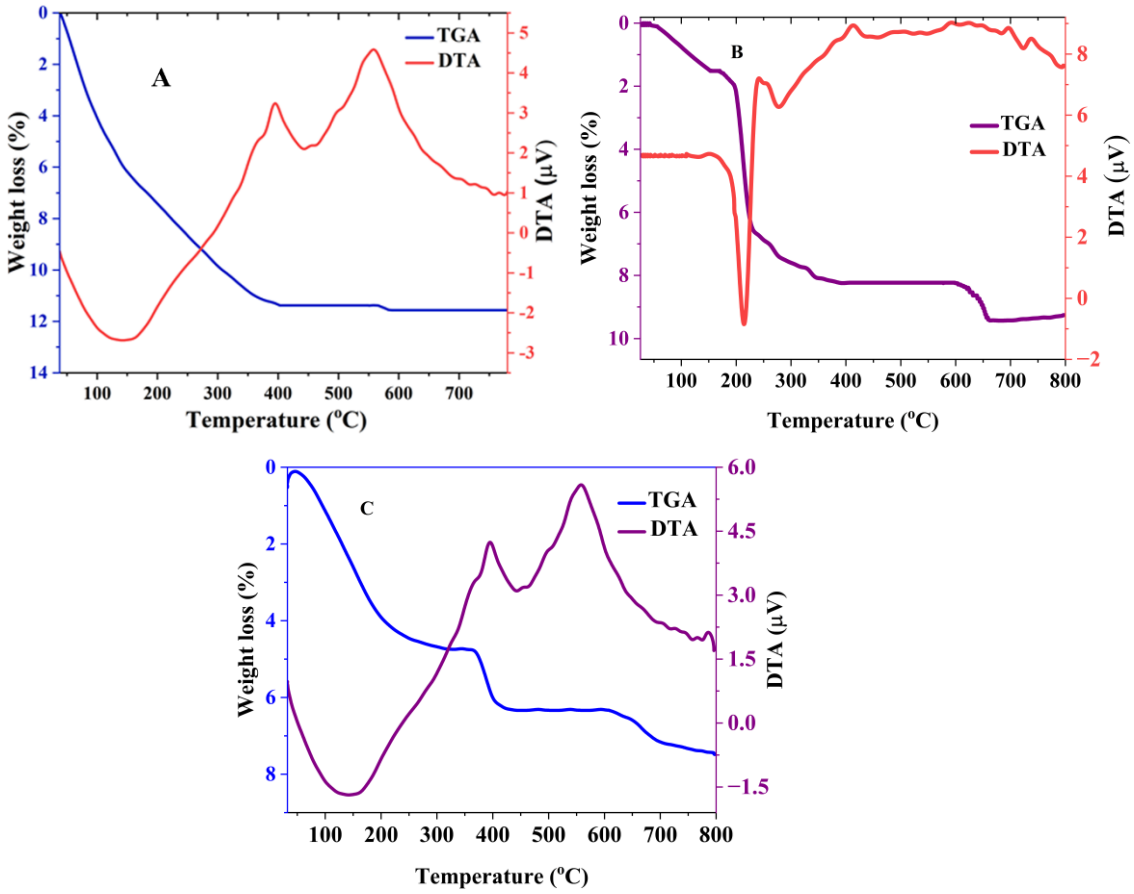

Figure 19. The TGA/DTA graph of green synthesized (A) TiO_2 NPs, (B) TiO_2/CuO NCs, and (C) TiO_2/ZnO NCs before calcination.

4.2.2 XRD Analysis

The XRD pattern of TiO_2 NPs was investigated by the profile-matching method using Xpert High Score Plus software. The XRD pattern of TiO_2 NPs demonstrates the high quality of fitting within the space group of I41/amd anatase (Figure 20A). The peaks obtained at 2θ values of 25.32 °, 37.07 °, 37.99 °, 38.58 °, 48.12 °, 53.97 °, 55.16 °, 62.79 °, 68.87 °, 70.42 °, and 75.07 ° with their corresponding crystal planes of (101), (103), (004),

(112), (200), (105), (211), (204), (116), (220), and (215), respectively, correspond to the TiO_2 crystal structure JCDPS card number of 78-2486 (Shimi *et al.*, 2022). The respective 2θ, Miller indices, average crystallite size, and d-spacings values are presented in Tables 7 and 8.

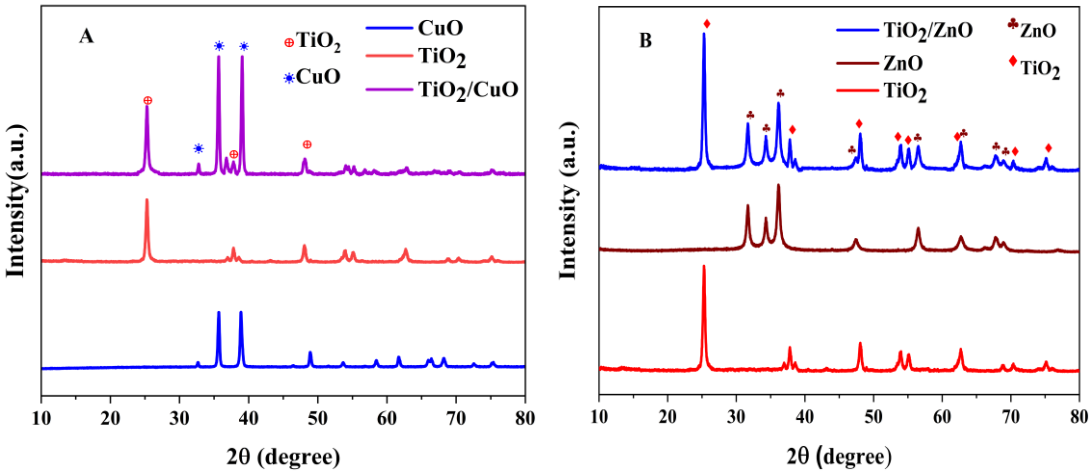

Figure 20. The XRD pattern of green synthesized (A) TiO_2 NPs, CuO NPs, and TiO_2/CuO (1:1) NCs and (B) TiO_2 NPs, ZnO NPs, and TiO_2/ZnO (1:1) NCs.

Table 7. The 2θ, d-spacing, miller indices, and average crystallite size of green synthesized TiO_2 NPs.

Sample	2θ (deg)	d-spacing (nm)	Miller indices	Ave. crystallite size(nm)
TiO_2	25.32	0.352	(101)	11.34
	37.02	0.243	(103)	
	37.99	0.238	(004)	
	38.58	0.233	(112)	
	48.12	0.189	(200)	
	53.97	0.170	(105)	
	55.16	0.167	(211)	
	62.79	0.148	(204)	
	68.87	0.137	(116)	
	70.42	0.134	(220)	
	75.07	0.127	(215)	

Table 8. The 2θ, d-spacing, miller indices, and average crystallite size of green synthesized TiO_2/CuO (1:1) NCs.

Sample	2θ (deg)	d-spacing (nm)	Miller indices	Ave. crystallite size (nm)
TiO_2/CuO (1:1)	25.28	0.352	(101)	13.91
	32.96	0.274	(110)	
	35.65	0.252	(11-1)	
	36.78	0.243	(103)	
	37.81	0.238	(004)	
	38.89	0.233	(111)	
	48.2	0.189	(200)	
	53.92	0.171	(105)	
	55.12	0.167	(211)	
	62.68	0.148	(204)	
	75.06	0.127	(215)	

Additional peaks are observed at 2θ of 32.52°, 35.65°, 38.84° and corresponding crystal plane values are (110), (11-1), and (111) in the XRD pattern of TiO_2/CuO (1:1) NCs, which are the characteristic diffraction peaks of CuO, confirming the formation of an interface between TiO_2 and CuO in TiO_2/CuO (1:1) NCs. The CuO phase is indexed to tenorite with the monoclinic structure and similar to the reported JCPDS reference #48-1548 (Ramírez *et al.*, 2020) (Figure 20A) (see the major peak data listed in Table 8). Besides, characteristic diffraction peaks of ZnO are also observed in TiO_2/ZnO (1:1) NCs at 2θ of 31.61°, 34.42°, 36.14°, 56.51°, 68.04° and corresponding crystal plane values (100), (002), (101), (110), and (112), respectively (Figure 20B and Table 9). The obtained diffraction angles and corresponding crystal planes are matched with the $P6_3mc$ space group and verify the formation of zincite with hexagonal structure (JCPDS reference #36–1451) (Jayswal & Moirangthem, 2018; Mendes *et al.*, 2022). In general, the average crystallite sizes for all TiO_2 NPs, TiO_2/CuO NCs, and TiO_2/ZnO NCs are less than 100 nm, which indicates the formation of nanomaterials.

Table 9. The 2θ, d-spacing, miller indices, and average crystallite size of green synthesized TiO_2/ZnO (1:1) NCs.

Sample	2θ (deg)	d-spacing (nm)	Miller indices	Ave. crystallite size(nm)
TiO_2/ZnO (1:1) NCs	25.31	0.352	(101)	13.35
	31.61	0.282	(100)	
	34.42	0.261	(002)	
	36.14	0.248	(101)	
	37.83	0.238	(004)	
	48.12	0.189	(200)	
	53.94	0.171	(105)	
	55.13	0.167	(211)	
	56.51	0.163	(110)	
	62.74	0.148	(204)	
	68.04	0.138	(112)	
	75.08	0.127	(215)	

4.2.3 UV–Vis–DRS Analysis

The UV-Vis-diffused reflectance spectra of the green synthesized TiO_2 NPs, TiO_2/CuO (1:1) NCs, and TiO_2/ZnO (1:1) NCs are shown in Figure 21A. The bandgap energy was determined using the Kubelka–Munk plot, as shown in Equation 28 (Makuła *et al.*, 2018; Zhao *et al.*, 2015).

$$(F(R).h\nu)^{\frac{1}{n}} = A(h\nu - E_g) \quad (28)$$

Where F(R) represents the Kubelka–Munk function, which is expressed in Equation 29, h is Planck`s constant, the power 1/n depends on the type of the electron transition (n = 2 and n = 1/2 for direct and indirect transitions, respectively), A is a constant, ν represents the frequency of light, E_g is the band gap energy.

$$F(R) = \frac{K}{S} = \frac{(1-R)^2}{2R} \quad (29)$$

R, K, and S are reflectance, absorption, and scattering coefficients, respectively. The Kubelka–Munk plot of the green synthesized TiO_2 NPs, TiO_2/CuO (1:1), and TiO_2/ZnO (1:1) NCs is shown in Figure 21B. The bandgap energies were estimated by the

extrapolation of the linear region toward the horizontal axis. The bandgap energies of TiO_2 NPs, TiO_2/CuO (1:1) NCs, and TiO_2/ZnO (1:1) NCs are found to be 3.39, 2.91, and 2.98 eV, respectively. The bandgap of the synthesized TiO_2 NPs is greater (by 0.19 eV), compared to the reported bulk anatase phase bandgap (3.2 eV) (Wach *et al.*, 2023). This increase in bandgap is due to the size reduction of the synthesized TiO_2 NPs (Abbood & Ali, 2023). The bandgaps of the composites showed redshifts, compared to the pristine TiO_2 NPs. This shift is attributed to the functional bandgap distinction of CuO and ZnO with TiO_2 (Yan *et al.*, 2012), and Fermi-level equalization arrangement (Kalanur *et al.*, 2017). A material with a lower bandgap is more efficient for photocatalytic dye degradation application reactions because it can absorb light at longer wavelengths (Hassaan *et al.*, 2023). It may be due to sufficient charge carrier (electron-hole) separation.

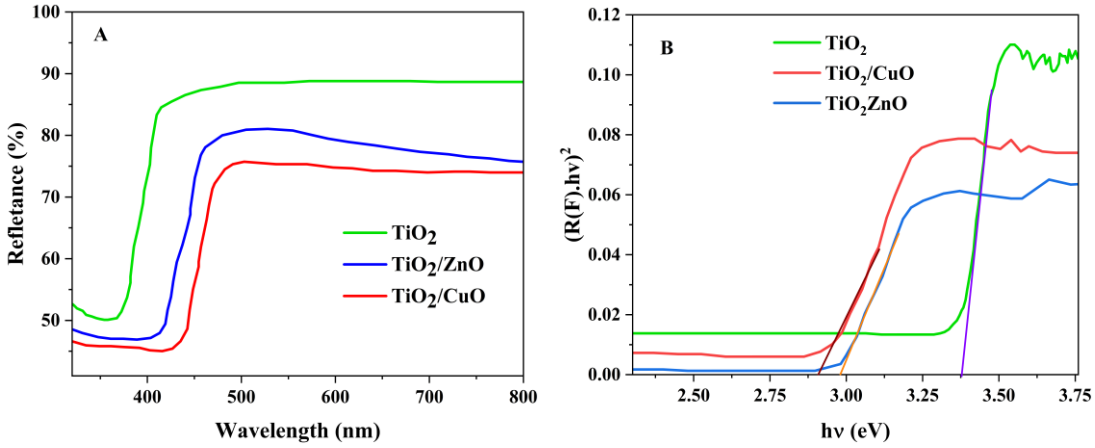

Figure 21. The UV-Vis DRS spectra (A) and Tauc`s plot (B) of green synthesized TiO_2 NPs, TiO_2/CuO (1:1) NCs, and TiO_2/ZnO (1:1) NCs.

4.2.4 FTIR Spectra Analysis

The FTIR spectra of TiO_2 NPs, TiO_2/CuO (1:1) NCs, and TiO_2/ZnO (1:1) NCs consist of the characteristic peaks of the green synthesized metal oxide nanomaterials (Figure 22). The broad band in the range of 3600 cm^{-1} – 3200 cm^{-1} is attributed to the hydroxyl group of the water molecule's intermolecular interaction with the surface of NMs (Alamier *et al.*, 2023; Nandiyanto *et al.*, 2019). The absorption peak at 1635 cm^{-1} is ascribed to the stretching vibration of the O–H bond. The vibrational band at 2343 cm^{-1} is related to the adsorption of atmospheric CO_2 on the surface of NPs (Ali *et al.*, 2022; Aravind *et al.*, 2021a; Farooq *et al.*, 2019; Liao *et al.*, 2023). The stretching band associated with the

metal-oxygen bond is responsible for the significant absorption peaks in the 1000–420 cm^{-1} region (Aravind *et al.*, 2021a; Mansour *et al.*, 2019). The peak at about 451 cm^{-1} is ascribed to the bending vibration of Ti–O (Mathew *et al.*, 2012; Sethy *et al.*, 2020). The band detected at about 876 cm^{-1} is associated with the Zn-O bending vibration in the sample (Abebe *et al.*, 2021; Bashir *et al.*, 2022; Sunaryono *et al.*, 2021). Moreover, the peak observed at 576 cm^{-1} can be ascribed to Cu-O vibration, indicating the presence of CuO in the synthesized NCs (Alhalili, 2022; Sayed *et al.*, 2024; Shawky *et al.*, 2024). The FTIR spectrum of both TiO_2/CuO (1:1) NCs and TiO_2/ZnO (1:1) NCs shows peak shifts towards high wavenumber, which is probably associated with ZnO and CuO interface formation on the TiO_2 surface (Lan *et al.*, 1993).

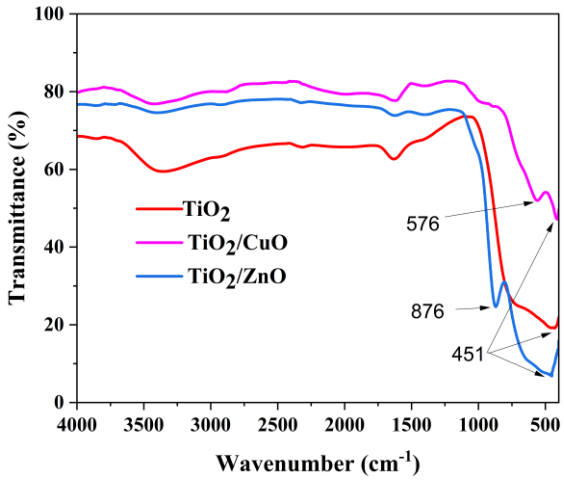

Figure 22. The FTIR spectra of green synthesized TiO_2 NPs, TiO_2/CuO NCs, and TiO_2/ZnO NCs.

4.2.5 Raman Spectra Analysis

The Raman spectroscopic technique was used for structural identification of the green synthesized TiO_2 NPs, TiO_2/CuO (1:1) NCs, and TiO_2/ZnO (1:1) NCs. The Raman spectral analysis of the green synthesized TiO_2 NPs showed tetragonal anatase Raman active modes of vibrational spectrum centered at $3E_g$ 515 cm^{-1} (A_{1g}), 399 cm^{-1} (B_{1g}), 519 cm^{-1} (B_{1g}), 144 cm^{-1} (E_g), 197 cm^{-1} (E_g), and 639 cm^{-1} (E_g) (Figure 23A), and similar results are also reported (Al-Taweel & Saud, 2016; El-Deen *et al.*, 2018; Kundu & Mondal, 2019; Raguram & Rajni, 2019; Wypych *et al.*, 2014). In the Raman spectra of TiO_2/CuO (1:1) NCs, the peaks detected at 296 cm^{-1}($A_{1}g$), 345 cm^{-1}($B_{1}g$), and 631 cm^{-1} ($B_{1}g$) correspond

to CuO modes of vibration (Figure 23B), which is in good agreement with the report by Deny and Murthy and their coworkers (Dey *et al.*, 2021; Murthy *et al.*, 2011).

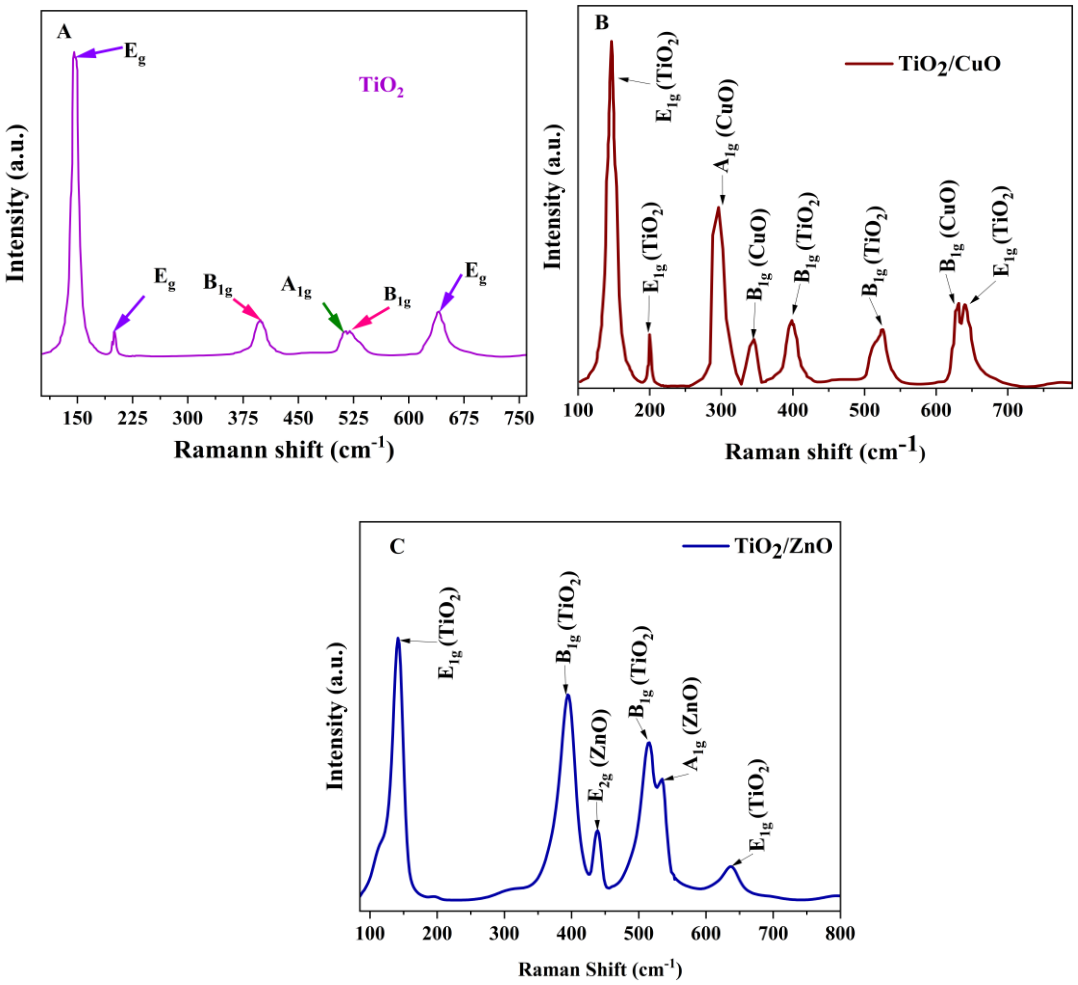

Figure 23. The Raman spectra of (A) TiO_2 NPs, (B) TiO_2/CuO (1:1) NCs, and (C) TiO_2/ZnO (1:1) NCs.

Moreover, $3E_g$ and $2B_{1g}$, vibrational spectra centered at 144, 197, 639, 399, and 519 cm^{-1}, respectively, suggest the presence of an anatase phase in the TiO_2/CuO (1:1) NCs composites (Antony *et al.*, 2015). In the Raman spectra of TiO_2/ZnO (1:1) NCs, where ZnO Raman modes that are located at 434 and 535 cm^{-1} correspond to the two typical vibrational modes E_2g and A_1g, confirming the hexagonal wurtzite structure of zinc oxide crystals, respectively (Figure 23C) (Zhang & Li, 2019). Additional peaks at 144 cm^{-1}, 339 cm^{-1}, 519 cm^{-1}, and 638 cm^{-1} are observed in the Raman spectrum of the TiO_2/ZnO (1:1) NCs, which are assigned to the E_{1g}, $2B_{1g}$, and E_g modes of the anatase phase of TiO_2, respectively.

4.2.6 PL Spectra Analysis

The optical properties of the TiO_2 NPs, TiO_2/CuO (1:1) NCs, and TiO_2/CuO (1:1) NCs were further characterized by PL techniques. The emission intensity of TiO_2/CuO (1:1) NCs and TiO_2/ZnO (1:1) NCs decreases significantly compared to the pristine TiO_2 NPs (Figure 24). TiO_2/CuO (1:1) NCs showed the weakest PL intensity, indicating the highest charge separation efficiency. This intensity reduction with the addition of CuO and ZnO corresponds to the increase in the lifetime of charge carriers, preventing the recombination of photogenerated electrons and holes (Dutta *et al.*, 2024; Li *et al.*, 2023).

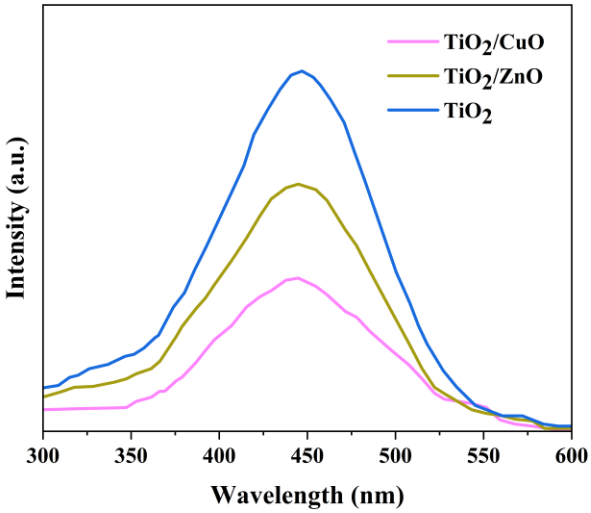

Figure 24. The PL spectra of TiO_2 NPs, TiO_2/ZnO (1:1) NCs, and TiO_2/ZnO (1:1) NCs.

4.2.7 BET Analysis

The N_2 adsorption-desorption isotherm technique was used for textural properties of the as-synthesized TiO_2 NPs, TiO_2/CuO (1:1) NCs, and TiO_2/ZnO (1:1) NCs (Figure 25A-C, respectively). The inset plots in Figure 25A-C correspond to the BJH pore size distribution curve of TiO_2 NPs, TiO_2/CuO (1:1) NCs, and TiO_2/ZnO (1:1) NCs. A typical isotherm plot of the N_2 adsorption-desorption plot seems a type IV isotherm with an H3 hysteresis loop in the relative pressure range of 0.57-0.9, indicating uniform surface areas with a mesoporous nature (Toncón-Leal *et al.*, 2021).

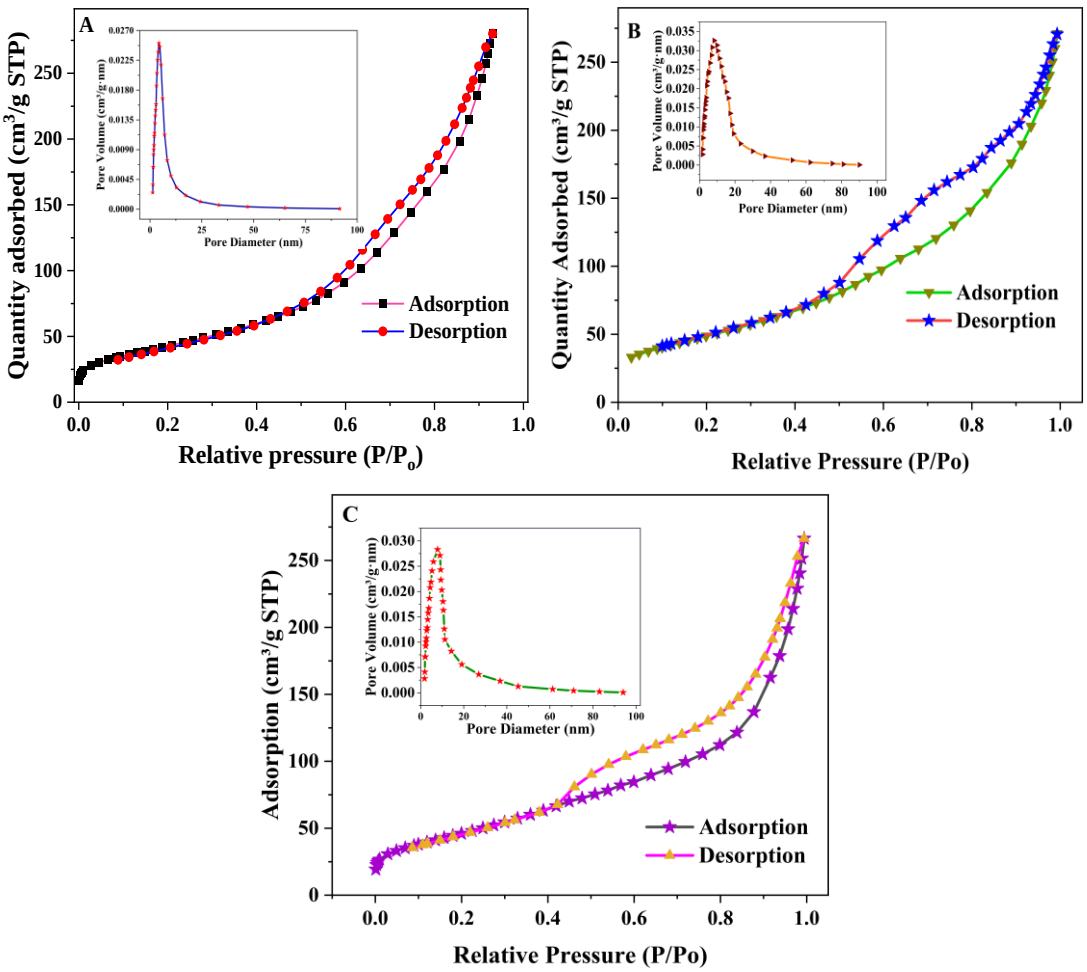

Figure 25. Nitrogen adsorption-desorption plots of TiO_2 NPs, TiO_2/ZnO (1:1) NCs, and TiO_2/ZnO (1:1) NCs.

The surface area, pore diameters, and pore volume of TiO_2 NPs are 65 m^2/g, 7.45 nm, and 0.026 cm^3/g, respectively, while for TiO_2/CuO (1:1) NCS, the values are 94 m^2/g, 0.032 cm^3/g, and 8.27 nm in that order. The respective specific surface area, pore volume, and pore diameters for TiO_2/ZnO (1:1) NCs are 91 m^2/g, 0.028 cm^3/g, and 7.85 nm (Table 10). Among the samples, TiO_2/CuO (1:1) showed the highest specific surface area and pore diameter, which is similar to the report by Lu (Lu *et al.*, 2019). A higher surface area provides more surface-active sites for the adsorption of more dyes, resulting in a more efficient photocatalytic degradation process and DSSC application (Baudys *et al.*, 2023; Masood *et al.*, 2023).

Table 10. Summary of pore diameter, pore volume, and surface area of the synthesized materials.

Photocatalyst	Surface area (m^2/g)	Pore diameter (nm)	Average Pore Volume (cc/g)
TiO_2 NPs	65	7.45	0.026
TiO_2/CuO (1:1) NCs	94	8.27	0.032
TiO_2/ZnO (1:1) NCs	91	7.85	0.028

4.2.8 XPS analysis

X-ray photoelectron spectroscopy (XPS) analysis was done to identify the oxidation states of the prepared samples. Figure 26A-C shows the survey spectra of TiO_2 NPs, TiO_2/CuO (1:1) NCs, and TiO_2/ZnO (1:1) NCs, respectively. In Figure 26A, the major peaks indicate the presence of the expected elements. Figure 26B displays the presence of Cu elements in addition to Ti, O, and C. Similarly, Figure 26C shows the presence of Zn, Ti, O, and C elements.

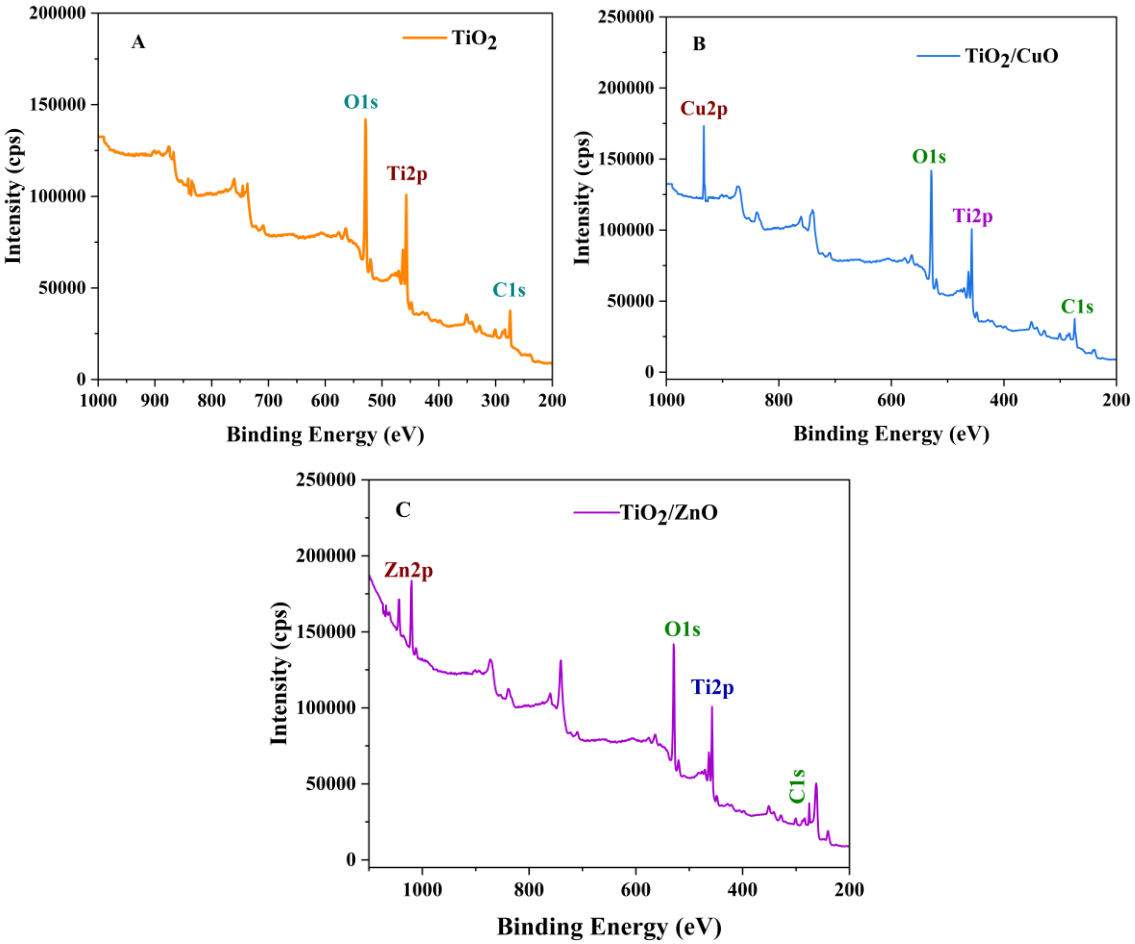

Figure 26. The XPS spectra of (A)TiO_2 NPs, (B)TiO_2/CuO (1:1) NCs, and (C) TiO_2/ZnO (1:1) NCs.

Figure 27 shows the deconvoluted XPS spectra of the samples using a Gaussian fit method. In the core-level XPS spectrum of Ti2p, the binding energy (BE) values for the $Ti^{4+}2p_{1/2}$ and $Ti^{4+}2p_{3/2}$ were observed at 464.14 eV and 458.66 eV, and these two peaks correspond to the Ti^{4+} of TiO_2 NPs (Figure 27A). The difference in binding energy due to the spin-orbit coupling was 5.7 eV, which is well-matched with the related literature report values (Azeez *et al.*, 2018; Bharti *et al.*, 2016). The O1s spectra of TiO_2 showed two peaks: a major peak at binding energies of 530.5 eV and a minor peak at 532.014 eV, which are attributed to oxygen anions (O-Ti-O) and surface hydroxyl (-OH) species, respectively (Figure 27B) (Matouk *et al.*, 2022).

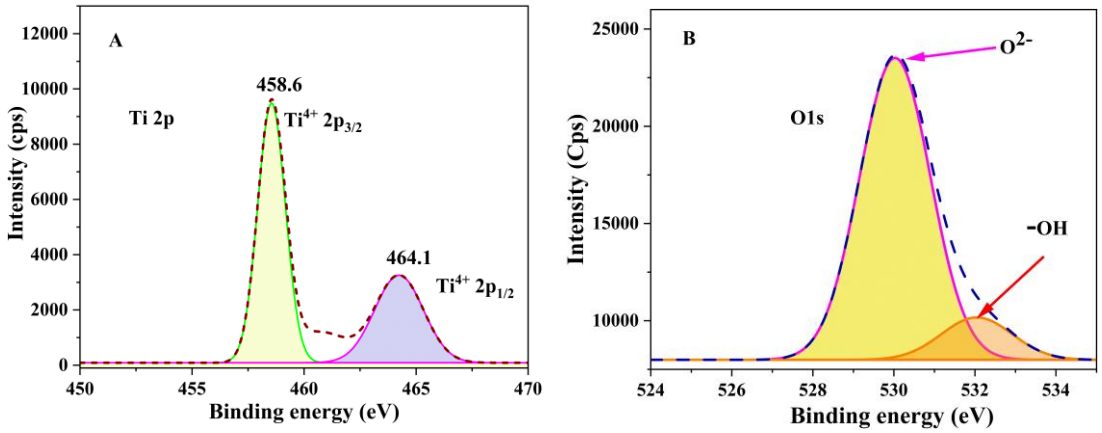

Figure 27. Deconvoluted Ti2p XPS spectra (A), O1s spectra (B) of TiO_2 NPs.

Figures 28A and 28B show the Ti2p and Cu2p core levels XPS spectra of TiO_2 and CuO, respectively, in TiO_2/CuO (1:1) NCs. The peaks corresponding to $Cu^{2+}2p_{1/2}$ and $Cu^{2+}2p_{3/2}$ are observed at 952.7 and 933.1 eV, respectively, which confirms the formation of CuO in the nanocomposites (Kumar *et al.*, 2017). The binding energy difference between the two peaks is about 20 eV. This value agrees with the previously reported values of CuO (Anand *et al.*, 2024; Boruban & Esenturk, 2018; Parhizkar *et al.*, 2005). Spin-orbit splitting of $Zn^{2+}2p_{3/2}$ (1021.9 eV) and $Zn^{2+}2p_{1/2}$ (1045.3 eV) is presented in Figure 28C, where the distance between these peaks is about 23.4 eV, which coincides well with the reported values of other researchers (Seleš *et al.*, 2024; Yildiz *et al.*, 2012). The O1s spectra of TiO_2 NPs showed two peaks: a major peak at binding energies of 530.5 eV and a minor peak at 532.02 eV (Figure 28D), which are attributed to oxygen anions of metal oxides and surface hydroxyl (-OH) species, respectively (Anand *et al.*, 2024; Matouk *et al.*, 2022; Sahai & Goswami, 2015). As shown in Figure 28E, the O1s spectra of TiO_2/CuO (1:1) NCs showed two peaks, a major peak at binding energies of 529.8 eV and a minor peak at 532.5 eV, which are attributed to oxygen anions and surface hydroxyl (-OH) species, respectively (Bharti *et al.*).

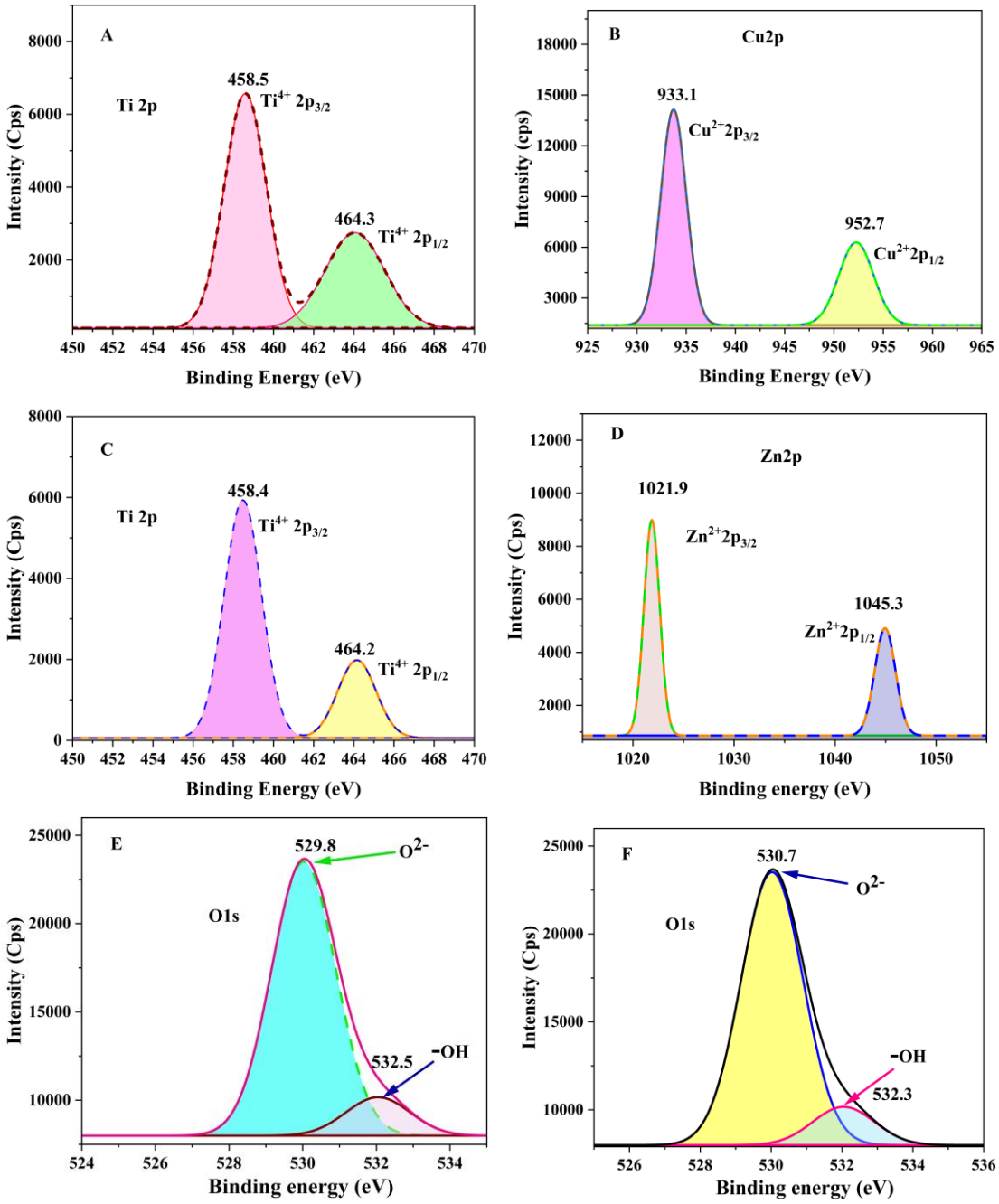

Figure 28. Deconvoluted XPS spectra of Ti2p (A) and (B) Cu2p of TiO_2/CuO (1:1) NCs, (C) Ti2p and Zn2p (D) of TiO_2/ZnO (1:1) NCs, and O1s of TiO_2/CuO (1:1) NCs, (E) and TiO_2/ZnO (1:1) NCs (F).

4.2.9 SEM/EDX Analysis

The SEM analysis technique determined the morphology of green synthesized TiO_2 NPs, TiO_2/CuO (1:1) NCs, and TiO_2/ZnO (1:1) NCs. The results show porous morphology with

a spherical shape for all TiO_2 NPs, TiO_2/CuO (1:1) NCs, and TiO_2/ZnO (1:1) NCs (Figure 29A-C). This porous nature of the materials is good for dye adsorption during the photocatalysis experiment (Purkait *et al.*, 2020). The particles are almost uniformly distributed with less aggregation. Reduced NP aggregation was a result of the plant extract's unique phytochemicals, including flavonoids, polyphenols, terpenoids, and alkaloids. The formation and development of nanoparticles during synthesis are impacted by the various ways in which these phytochemicals interact and stabilize the metal oxide precursors. (Atiek *et al.*, 2024; Rani *et al.*, 2023).

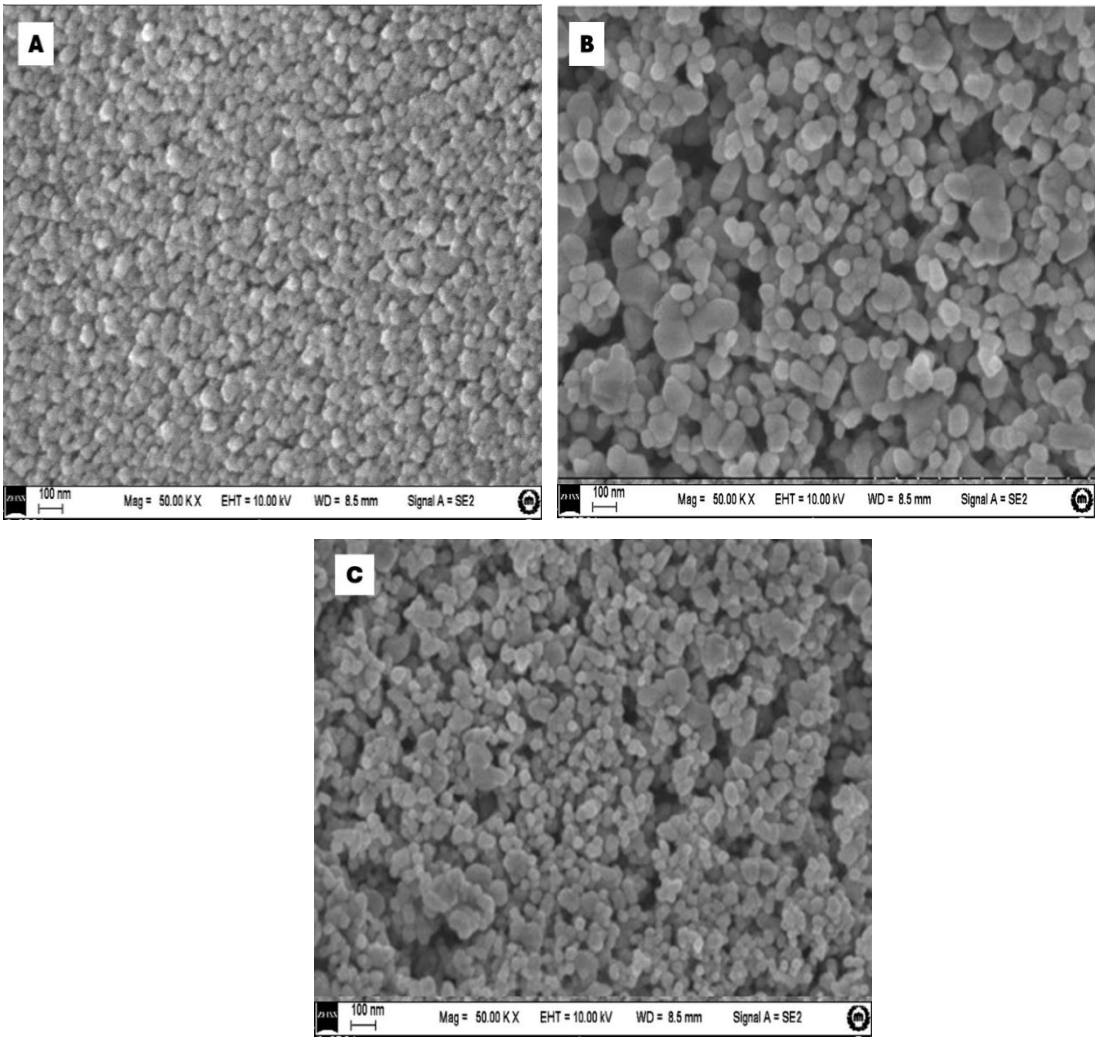

Figure 29. The SEM micrograph of (A) TiO_2 NPs, (B) TiO_2/CuO (1:1) NCs, and (C) TiO_2/ZnO (1:1) NCs.

The EDX analysis was done to reveal the elemental composition and percentages in TiO_2 NPs, TiO_2/CuO (1:1) NCs, and TiO_2/ZnO (1:1) NCs (Figure 30A-C). The EDX spectrum,

shown in Figure 30A, indicates the existence of only Ti and O in the as-synthesized TiO_2 NPs. The weight% of Ti and O are 54.33% and 45.67%, and their atomic% are 28.44 % and 71.56 %, respectively. The EDX spectrum, shown in Figure 30B, indicates the existence of only Ti, Cu, and O elements in the as-synthesized TiO_2/CuO (1:1) NCs. The weight% (40.42%, 33.25%, and 27.33%) and atomic% (69.33%, 19.01%, and 11.76%) values of the Ti, Cu, and O elements, respectively, are depicted in Figure 30B inset. The EDX spectrum, presented in Figure 30C, shows the presence of only Ti, Zn, and O elements in the green synthesized TiO_2/ZnO (1:1) NCs. The weight% (43.14% O, 32.54% Ti, and 24.32% Zn) and atomic% (71.95% O, 18.12% Ti, and 9.93% Zn) of the elements are also illustrated in Figure 30C inset.

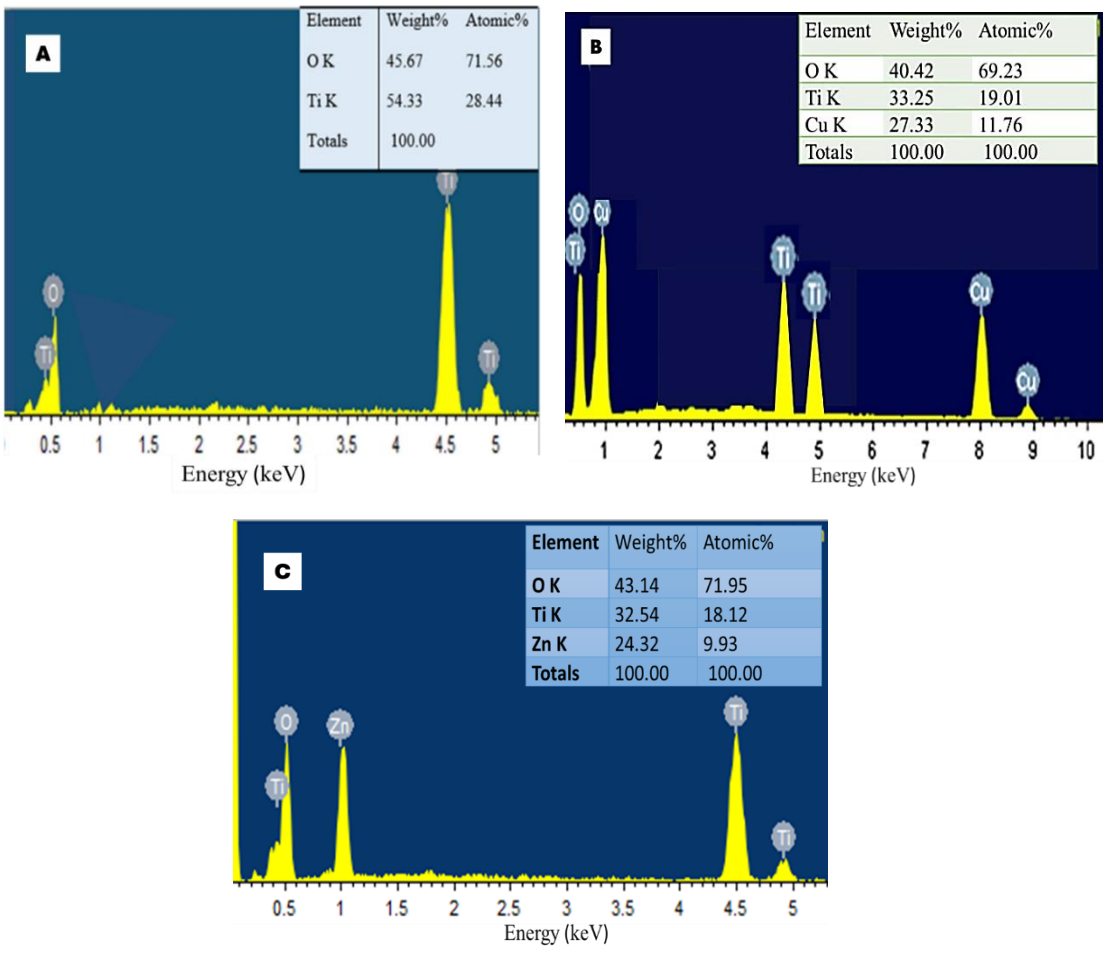

Figure 30. The EDX spectra of (A) TiO_2 NPs, (B) TiO_2/CuO (1:1) NCs, and (C) TiO_2/ZnO NCs.

4.2.10 TEM/HRTEM Analysis

The TEM image analysis of green synthesized TiO_2 NPs, TiO_2/CuO (1:1) NCs, and TiO_2/ZnO (1:1) NCs confirms the formation of nanostructures with less aggregation (Figures 31A, C, and E). The average particle size from the TEM micrographs using ImageJ software is depicted in Figures 31B, D, and F for TiO_2 NPs, TiO_2/CuO (1:1) NCs, and TiO_2/ZnO (1:1) NCs, respectively. The average particle sizes were 27, 23, and 21 nm, respectively.

Figure 32A revealed the HRTEM micrograph of green synthesized TiO_2 nanoparticles. The parallel lattice fringes of the NPs, as shown in Figure 32A insects, are visible. The d-spacing of the crystallites, which is determined using the Inverse Fast Fourier Transformation (IFFT) using Gatan software, confirms their single-crystallinity. The d-spacing values of 0.352 nm, 0.245 nm, and 0.191 nm are matching with the (101), (004), and (200) anatase phases, respectively, which are consistent with the XRD results. Similarly, Figure 32B revealed the HRTEM micrograph of green synthesized TiO_2/CuO (1:1) NCs. The obtained d-spacing values are 0.352 nm (101) and 0.171 nm (105), confirming the TiO_2 anatase phase, and 0.252 nm (11-1) and 0.233 nm (111), confirming monoclinic CuO. Thus, the d-spacing analysis from the HRTEM image confirms the formation of an interface between TiO_2 and CuO crystals (Thamaphat *et al.*, 2008). Likewise, the HRTEM micrograph of TiO_2/ZnO (1:1) NCs (Figure 32C) showed the formation of TiO_2/ZnO (1:1) NCs. The d-spacing values of 0.352 nm and 0.189 nm with Miller indices values of (101) and (200), respectively, indicate the formation of the anatase phase of TiO_2 in TiO_2/ZnO (1:1) NCs. In the same way, the d-spacing values of 0.248 nm and 0.282 nm with Miller indices of (101) and (100), respectively, indicate the presence of zincite phase in TiO_2/ZnO (1:1) NCs (Kumar *et al.*, 2014). In general, the lattice fringes of the synthesized nanomaterials from HRTEM analysis coincide with the values obtained from XRD analysis.

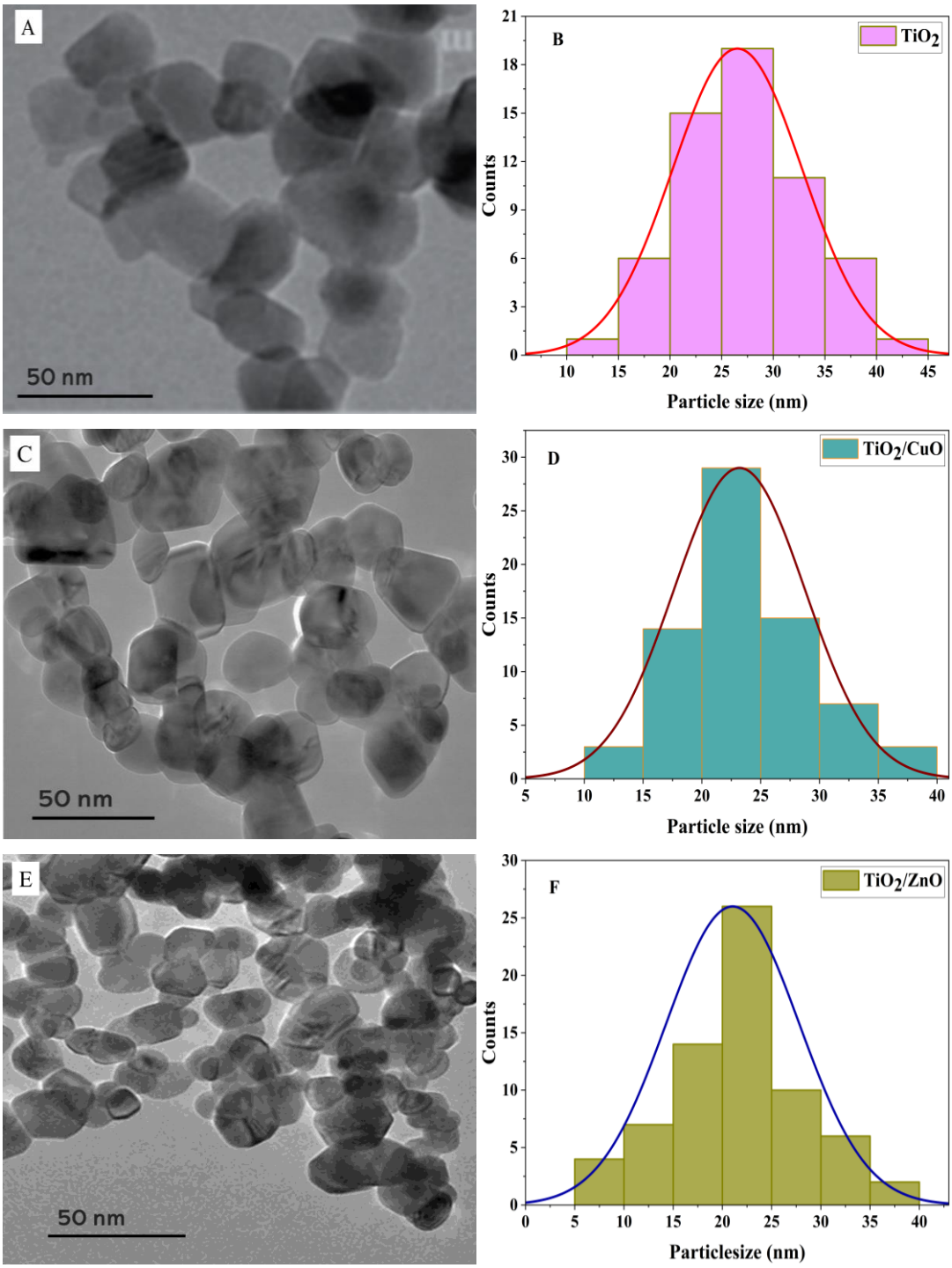

Figure 31. The TEM micrographs (A, C, and E) and the histograms of the particle size distributions (B, D, and F) for TiO_2, TiO_2/CuO (1:1) NCs, and TiO_2/ZnO (1:1) NCs, respectively.

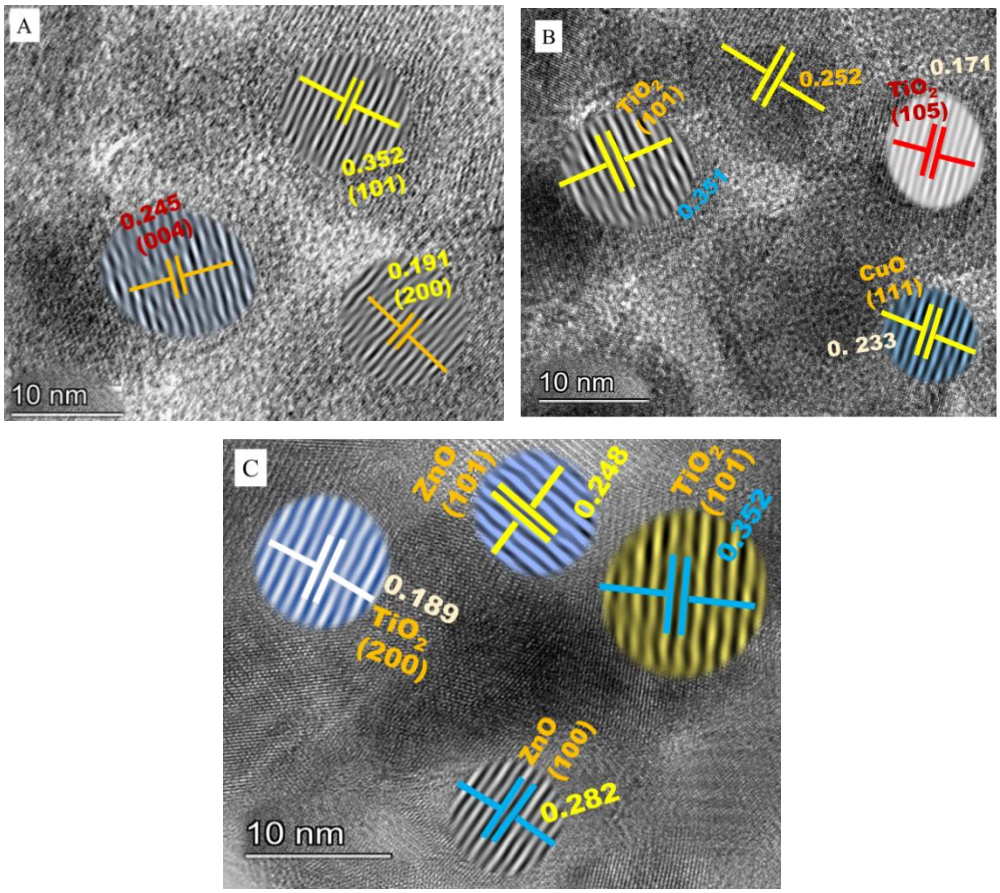

Figure 32. High-resolution images of (A) TiO_2 NPs, (B) TiO_2/CuO (1:1) NCs, and (C) TiO_2/ZnO (1:1) NCs.

4.2.11 Mott-Schottky Analysis

An energy barrier or band offset presented at an interface would have a large effect on electron transfer (Shen *et al.*, 2014). The Mott-Schottky plot analysis was used to experimentally determine the approximate positions of the conduction and valence bands of the semiconductors through the interpretation of impedance (Mott–Schottky) plots. The Mott–Schottky plots of TiO_2, TiO_2/CuO (1:1) NCs, and TiO_2/ZnO (1:1) NCs are given in Figure 33. The flat band potential was obtained by extrapolating the $1/C^2$ vs potential plot to the x-axis. As shown in Figure 33A, TiO_2 and TiO_2/ZnO (1:1) showed a positive slope, revealing an n-type semiconductor with a flat band potential of -0.33 V and -0.51 V vs Ag/AgCl, respectively. The Mott-Schottky plot of TiO_2/CuO (1:1) NCs shows both positive and negative slopes (Figure 33B). The positive slope is due to n-type TiO_2 with a flat band potential of -0.41 V vs Ag/AgCl, whereas a negative slope is associated with the p-type

CuO, a semiconductor with a flat band potential of 0.69 Vvs Ag/AgCl. The Nernst equation (Equation 30) can convert the potential measured with the Ag/AgCl reference electrode to the potential relative to the reversible hydrogen reference electrode (RHE) (Wei *et al.*, 2018).

$$E_{RHE} = E_{Ag/AgCl} + E^{\circ} + 0.059\, pH \qquad (30)$$

where E°Ag/AgCl(sat) = 0.197 V and the pH of the electrolyte is 7, thus, the flat band potentials relative to RHE could be 0.28 V for TiO_2 NPs, and 0.10 V for TiO_2/ZnO (1:1) NCs. For TiO_2/ZnO (1:1) NCs, the flat band potential is 0.2 V for TiO_2 (n-type) and 1.2 V for CuO (p-type). The conduction band edge and the valence band edge are near the flat band potentials of n-type and p-type semiconductors, respectively (F. Guo et al., 2021). Thus, the CB of TiO_2 NPs and TiO_2/ZnO (1:1) NCs could be 0.28 V and 0.10 V vs RHE, respectively. Similarly, the CB of TiO_2 and the VB of CuO in TiO_2/CuO NCs could be 0.20 V and 1.20 V vs RHE, respectively. A combination of these values with the bandgap energy obtained from the Kubelka–Munk plot is used to determine the band edge position using Equation 31 (Tian *et al.*, 2016; Wongsa *et al.*, 2022).

$$E_{VB} = E_{CB} + E_g \qquad (31)$$

The bandgap energies of TiO_2 NPs, TiO_2/CuO (1:1) NCs, and TiO_2/ZnO (1:1) NCs were found to be 3.39 eV, 2.91 eV, and 2.98 eV, respectively. Hence, the calculated VB edge positions of TiO_2 NPs and TiO_2/ZnO (1:1) NCs are 3.67 eV and 3.08 eV, respectively.

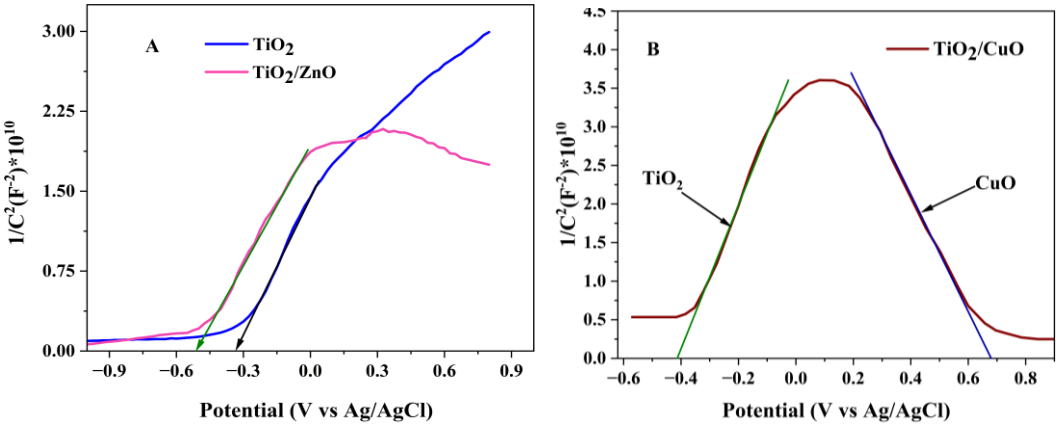

Figure 33. Mott-Schottky plots of green synthesized (A) TiO_2 NPs, TiO_2/ZnO (1:1) NCs,and (B) TiO_2/CuO (1:1) NCs *vs* Ag/AgCl.

The VB edge position of TiO_2 and the CB edge position of CuO for TiO_2/CuO (1:1) NCs are 3.11 and -1.71 eV, respectively. The bandgap diagram of these materials is displayed in Figure 34.

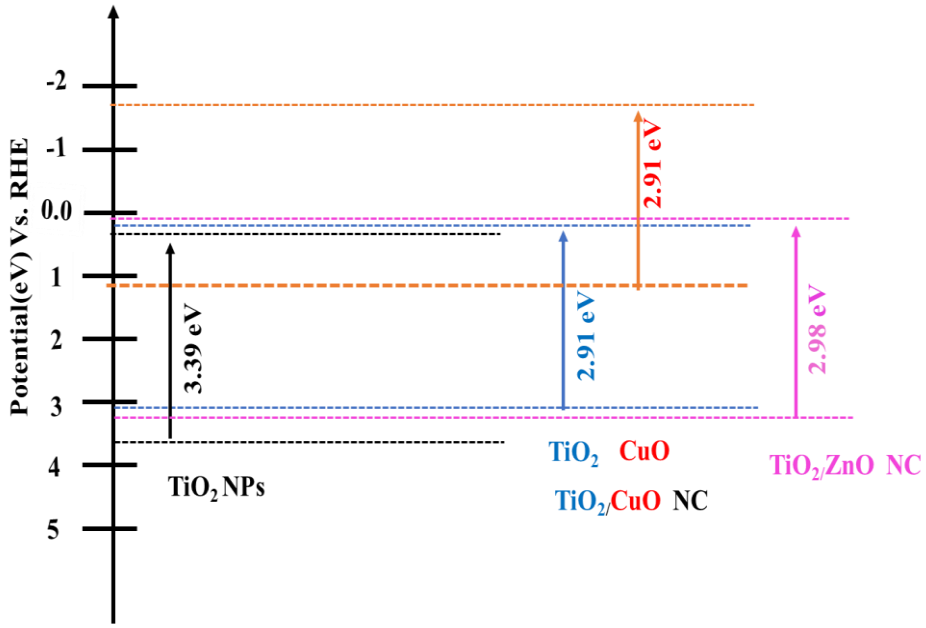

Figure 34. Energy diagram of green synthesized TiO_2 NPs, TiO_2/CuO (1:1) NCs, and TiO_2/ZnO (1:1) NCs depicted from the Mott-Schottky analysis.

4.3 Photocatalytic Performance of Synthesized Nanomaterials

4.3.1 Determination of pH_{PZC}

To conduct the photocatalytic performance experiment, it is important to know the surface charge of the photocatalyst and the nature of the pollutant in the solution. Since the charge of MB dye is cationic in an aqueous solution, it needs a negatively charged surface to be adsorbed before catalysis. Thus, the pH_{PZC} determination of the photocatalyst was done to know the point at which the photocatalyst surface becomes negative (Rahmani *et al.*, 2020; Zyoud *et al.*, 2023).

The pH_{PZC} for the surface of green synthesized TiO_2 NPs, TiO_2/CuO NCs, and TiO_2/ZnO NCs were found to be 7.32, 6.80, and 6.40, respectively (Figure 35A-C). Below pH_{PZC}, the surface of the adsorbent is positive and attracts anions, whereas above pH_{PZC}, the adsorbent's surface becomes negatively charged and attracts cationic species. An aqueous solution of MB dye is dominantly cationic and attracted towards the surface of the photocatalysts at the solution pH >pH_{PZC}.

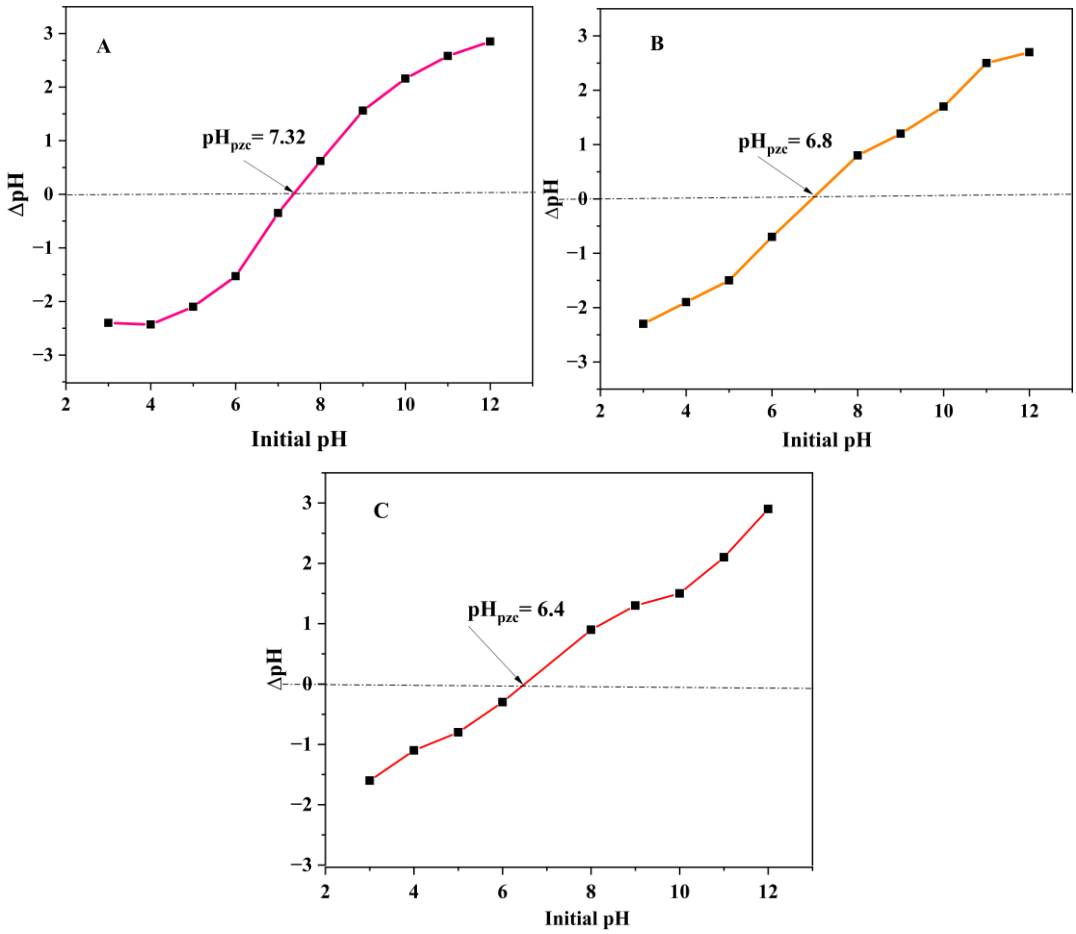

Figure 35. Point of zero charge determination of green synthesized (A) TiO_2 NPs, (B) TiO_2/CuO NCs, and (C) TiO_2/ZnO NCs.

4.3.2 Effect of Plant Extract Volume

To evaluate the amount of plant extract concentration on the photocatalytic efficiency of the synthesized nanomaterial, 25, 50, and 75 mL of IHL extracts were added separately to 15 mL of TTIP precursor. The photocatalytic performances of TiO_2 NPs synthesized using 25, 50, and 75 mL were tested against MB dye at constant parameters (pH of the solution 8, catalyst dose of 20 mg, dye concentration of 10 ppm, and 40 min contact time). The degradation efficiencies for 25, 50, and 75 mL of plant extract were found to be 40, 51, and 43%. The degradation efficiency of TiO_2 NPs synthesized using 50 mL plant extract was highest compared to others (Figure 36). The TiO_2 NPs synthesized using all volume ratios of plant extract showed higher regression constants in the pseudo-first-order kinetics model, indicating that the degradation of MB follows a pseudo-first-order reaction (Table 11). Among the synthesized TiO_2 NPs using the three ratios of plant extracts, TiO_2 NPs

synthesized using 50 mL showed the highest rate constant (0.014 min^{-1}). The pseudo-first-order kinetics model fitting indicates that the degradation of MB showed physisorption on the surface of the photocatalyst (Liu *et al.*, 2019).

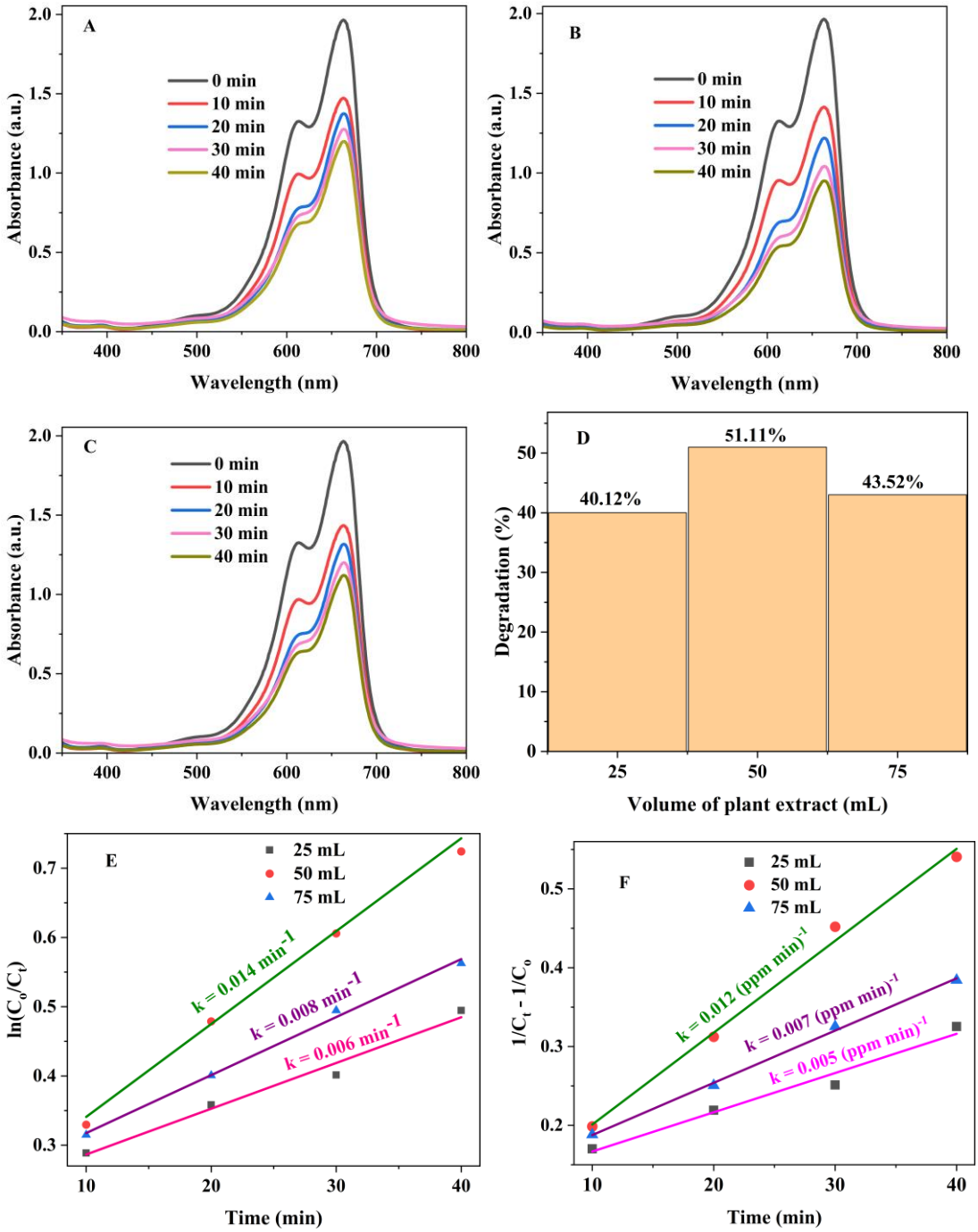

Figure 36. The UV-Vis absorption spectra of MB dye with TiO_2 synthesized using (A) 25 mL, (B) 50 mL, (C) 75 mL, (D) %degradation (E) pseudo-first order, and (F) pseudo-second-order kinetics.

Table 11. Degradation efficiency and rate of 20 mg TiO_2 NPs synthesized using 25, 50, and 75 mL of IHL extract against 10 ppm of MB at pH 8 and contact time of 40 min.

		Pseudo first order		Pseudo second order	
Volume of plant extract, mL	Degradation (%)	Regression coefficient	Rate constant (min^{-1})	Regression coefficient	Rate constant ($ppm^{-1}min^{-1}$)
25	40.12	0.997	0.006	0.995	0.005
50	51.11	0.994	0.014	0.989	0.012
75	43.52	0.996	0.008	0.992	0.007

4.3.3 Effect of Photocatalyst Ratio

Based on the optimization of the effect of plant extract volume, 50 mL of plant extract was selected for the synthesis of different ratios of NCs. The 2:1, 1:1, and 1:2 plant extract to photocatalyst ratios for TiO_2: CuO, and TiO_2: ZnO were synthesized by fixing the total volume of the precursor to 15 mL. The highest degradation efficiency values for TiO_2: CuO and TiO_2: ZnO (Figure 37) were obtained in a 1:1 ratio. The highest degradation percentage among all the ratios was 78.13% on a 1:1 ratio of TiO_2: CuO NCs. The kinetics analysis of the degradation of MB dye using TiO_2:CuO (1:1) NCS showed a better fit with the pseudo-first-order model (R^2 = 0.999 and k = 0.035 min^{-1}) as compared to the pseudo-second-order model (R^2 = 0.967 and k = 0.033 $ppm^{-1}min^{-1}$) (Figure 37 E & F, Table 12).

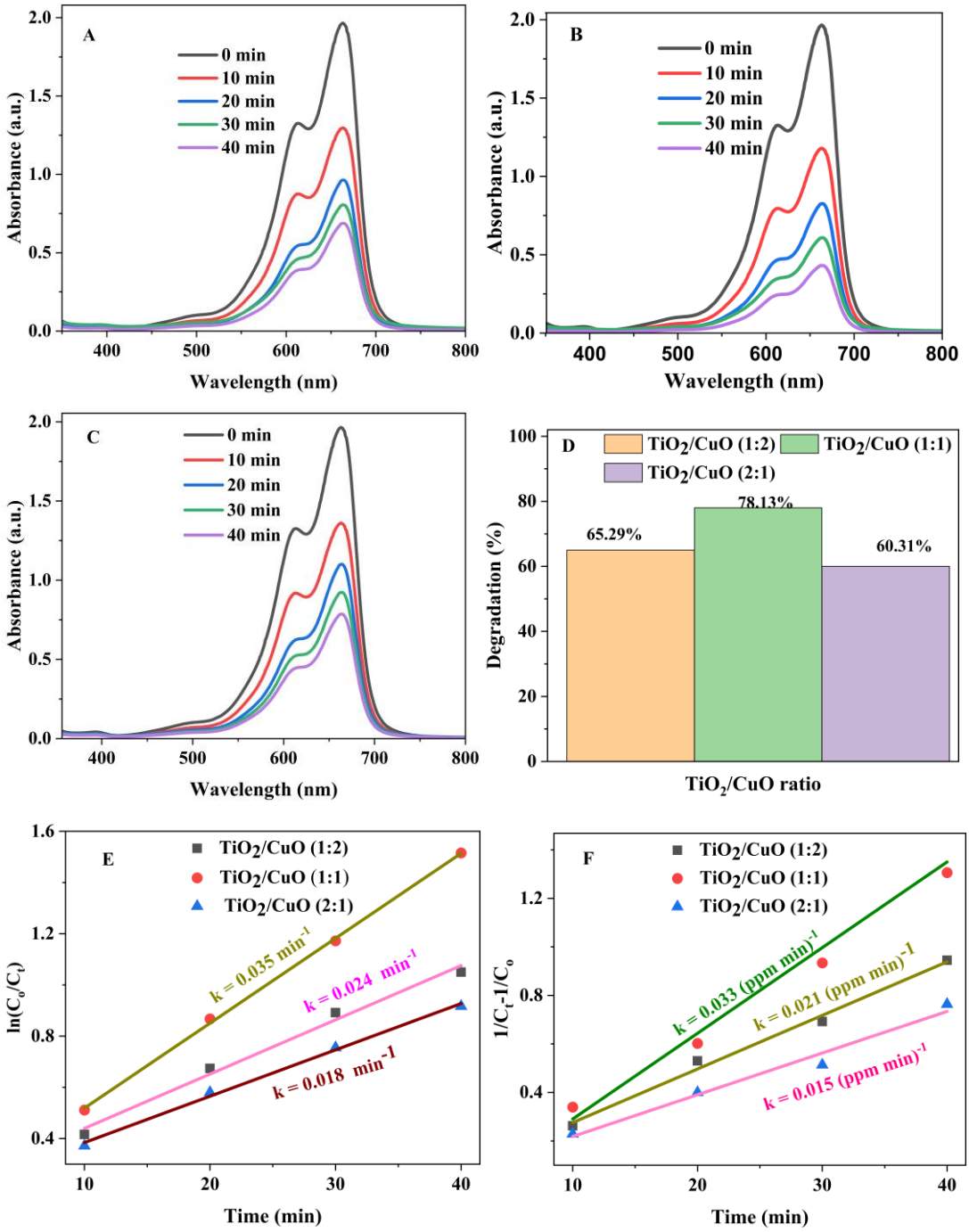

Figure 37. The UV-Vis absorption spectra of MB dye with (A) 1:2, (B) 1:1, (C) 2:1 TiO_2: CuO ratio, (D) %degradation (E) pseudo-first and (F) second order kinetics.

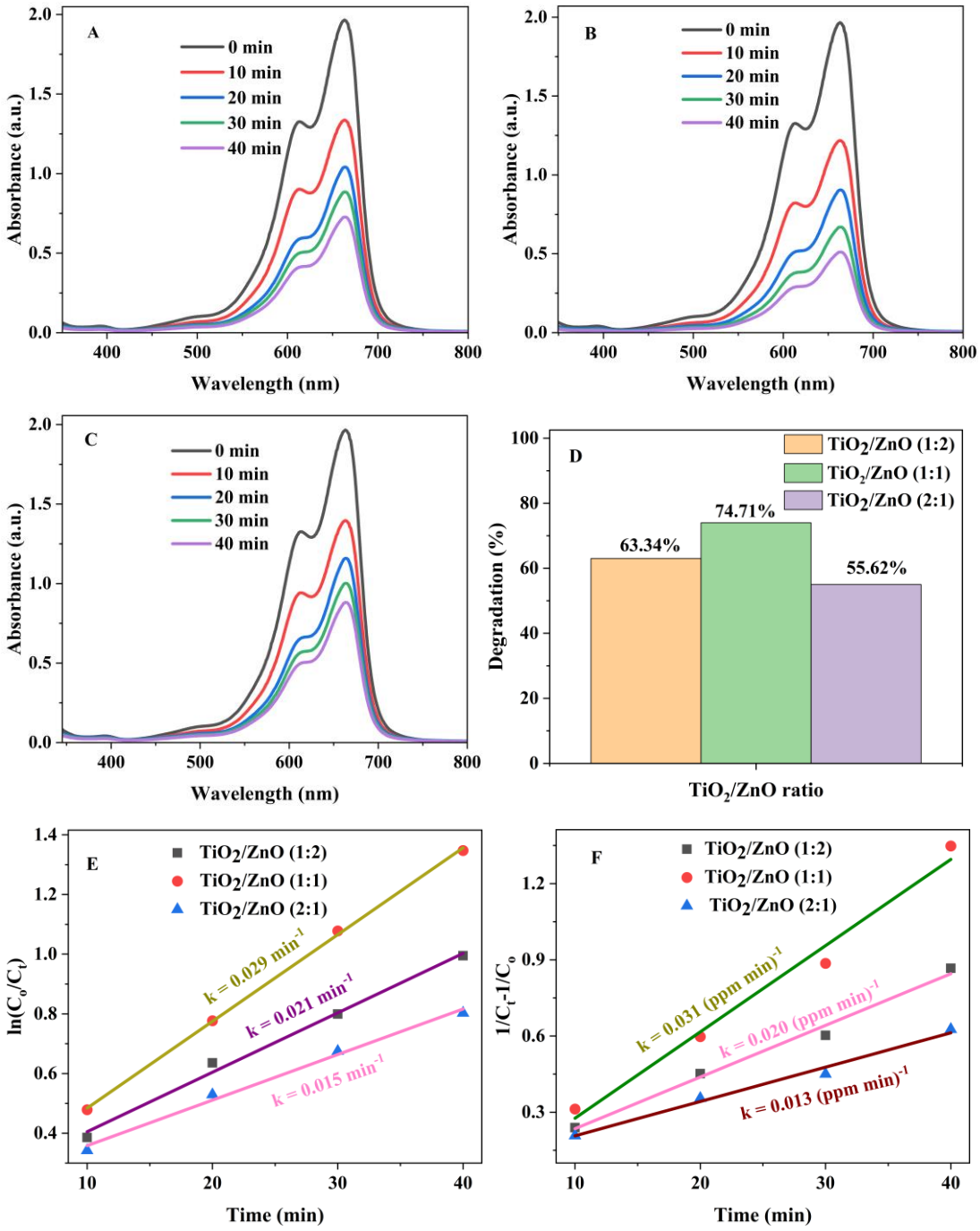

Figure 38. The UV-Vis absorption spectra of MB dye with (A) 1:2, (B) 1:1, (C) 2:1 TiO_2:ZnO ratio, (D) % degradation, (E) pseudo-first, and (F) second order kinetics.

Table 12. Degradation efficiency and rate of 20 mg of different precursors, Volume ratios (2:1, 1:1, and 1:2) TiO_2: CuO and TiO_2: ZnO synthesized using 50 mL of IHL extract against 10 ppm of MB at pH 8 and contact time of 40 min.

		Pseudo first order		Pseudo second order	
Nanocomposites	Degradation (%)	Regression coefficient	Rate constant (min^{-1})	Regression coefficient	Rate constant ($ppm^{-1}min^{-1}$)
TiO_2/CuO (1:2)	65.29	0.994	0.024	0.988	0.021
TiO_2/CuO (1:1)	78.13	0.999	0.035	0.967	0.033
TiO_2/CuO (2:1)	60.31	0.994	0.018	0.965	0.015
TiO_2/ZnO (1:2)	63.34	0.996	0.021	0.989	0.020
TiO_2/ZnO (1:1)	74.71	0.999	0.029	0.984	0.027
TiO_2/ZnO (2:1)	55.62	0.996	0.015	0.988	0.013

4.3.4 Effect of TiO_2/CuO (1:1) Dosage

Thus, the 1:1 ratio of TiO_2/CuO NCs was selected as the most effective among the rest, it was used to optimize other parameters. The photocatalyst dosage effect was performed using 10, 20, 30, and 40 mg of TiO_2/CuO (1:1) NCs at constant parameters of solution pH 8, dye concentration of 10 ppm, and 40 min contact time (Figure 38 and Table 13). The percentage degradation was maximum at the catalyst dosage of TiO_2/CuO (1:1) NCs 20 mg (78.13%), and the percentage decreased slightly with increasing the dosage amount. As the amount of TiO_2/CuO (1:1) NCs increases, the total active sites on the catalyst surface increase to some extent. However, a higher amount of catalyst dosage blocks the radiation from reaching the photocatalyst surface due to aggregation (Mortazavian *et al.*, 2019). The kinetics investigation of MB dye degradation employing 20 mg of TiO_2:CuO (1:1) NCs revealed a better fit with the pseudo-first-order model (R^2 = 0.999 and k = 0.034 min^{-1}) than with the pseudo-second-order model (R^2 = 0.967 and k = 0.033 $ppm^{-1}min^{-1}$) (Figure 39 E & F, Table 13),

Table 13. The degradation efficiency and rate of 10, 20, 30, and 40 mg TiO_2/CuO (1:1) NCs synthesized using 50 mL of IHL extract against 10 ppm of MB at pH 8 and contact time of 40 min.

		Pseudo first order		Pseudo second order	
Dosage (mg)	Degradation (%)	Regression coefficient	Rate constant (min^{-1})	Regression coefficient	Rate constant ($ppm^{-1}min^{-1}$)
10	68.89	0.999	0.026	0.985	0.007
20	78.13	0.999	0.033	0.993	0.014
30	74.49	0.997	0.028	0.983	0.009
40	72.98	0.996	0.026	0.987	0.011

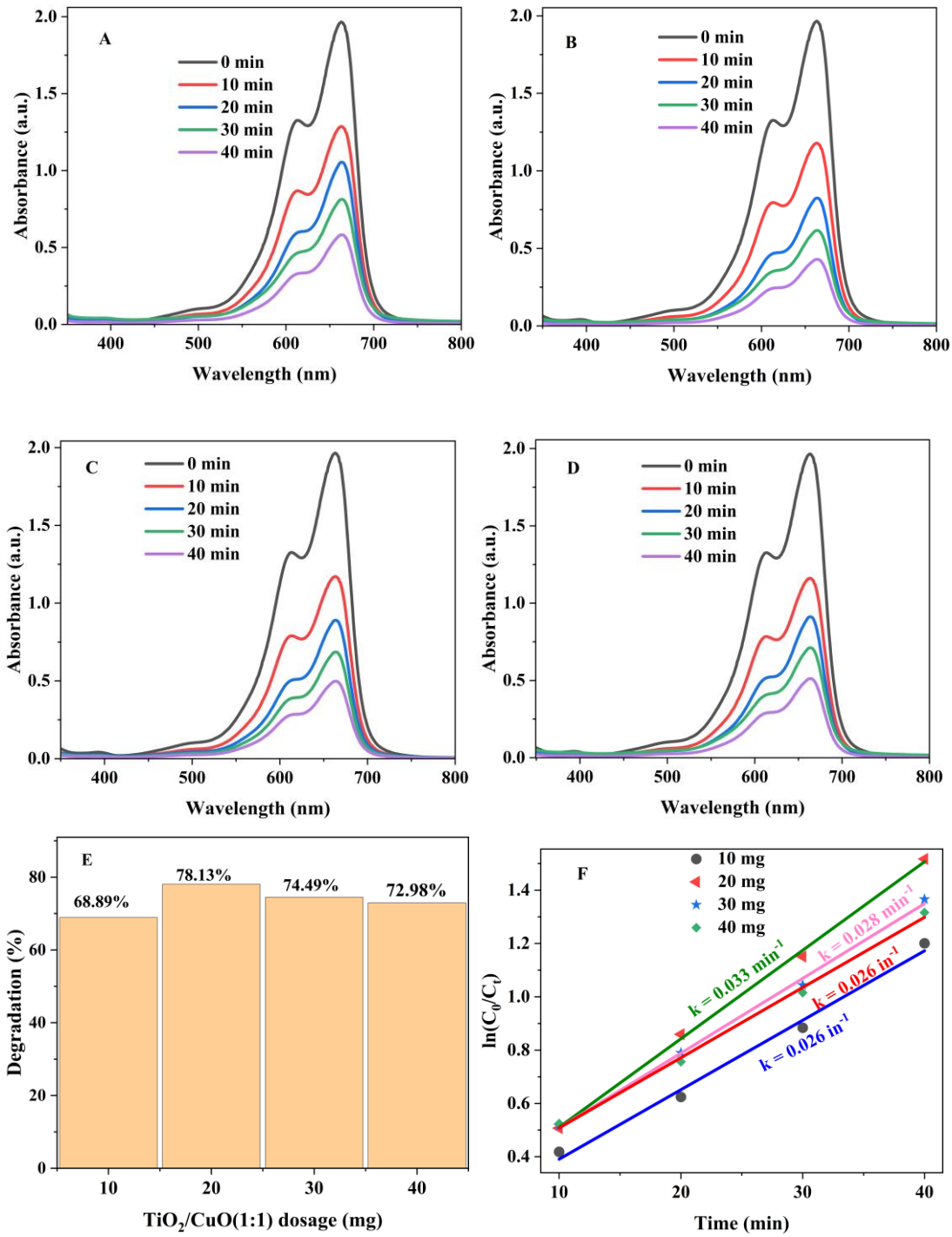

Figure 39. The UV-Vis absorption spectra of MB with (A) 10 mg, (B) 20 mg, (C) 30, (D) 40 mg of TiO_2/CuO (1:1), (E) %degradation (F) pseudo-first-order kinetics.

4.3.5 Effect of Initial Dye Concentration

The removal of MB dye from the aqueous solution was evaluated by varying MB initial concentration from 5 ppm to 20 ppm at a pre-optimized dose (20 mg), and constant solution pH and contact time of 8 and 40 min, respectively. The rate of MB degradation was evaluated when the concentration of MB dye was increased from 5 ppm to 20 ppm, and the degradation percentage was found to be 80.13 %, 78.06 %, 76.15 %, and 58.87 % for 5, 10, 15, and 20 ppm, respectively (Figure 40E). The maximum degradation efficacy was obtained at 15 ppm concentration. The kinetics investigation of MB dye degradation employing 20 mg of TiO_2/uO (1:1) NCs revealed a better fit with the pseudo-first-order model (R^2 = 0.991 and k = 0.034 min^{-1}) than with the pseudo-second-order model (R^2 = 0.989 and k = 0.016 $ppm^{-1}min^{-1}$) (Figure 40F and Table 14).

Table 14. The degradation efficiency and rate of 20 mg TiO_2/CuO (1:1) NCs synthesized using 50 mL of IHL extract against 5, 10, 15, and 20 ppm of MB at pH 8 and contact time of 40 min.

		Pseudo first order		Pseudo second order	
Dye concentration (ppm)	Degradation (%)	Regression coefficient	Rate constant (min^{-1})	Regression coefficient	Rate constant ($ppm^{-1}min^{-1}$)
5	80.13	0.993	0.031	0.984	0.012
10	78.13	0.999	0.033	0.988	0.013
15	76.15	0.991	0.034	0.989	0.016
20	58.87	0.997	0.017	0.990	0.012

A sudden decrease in the photodegradation efficiency (Table 14) to 58.87% as the amount of MB dye was increased to 20 ppm was ascribed to the accumulation of MB dye on the photocatalyst surface, which prevents the direct contact of light irradiation to the catalyst surface (Reza *et al.*, 2017).

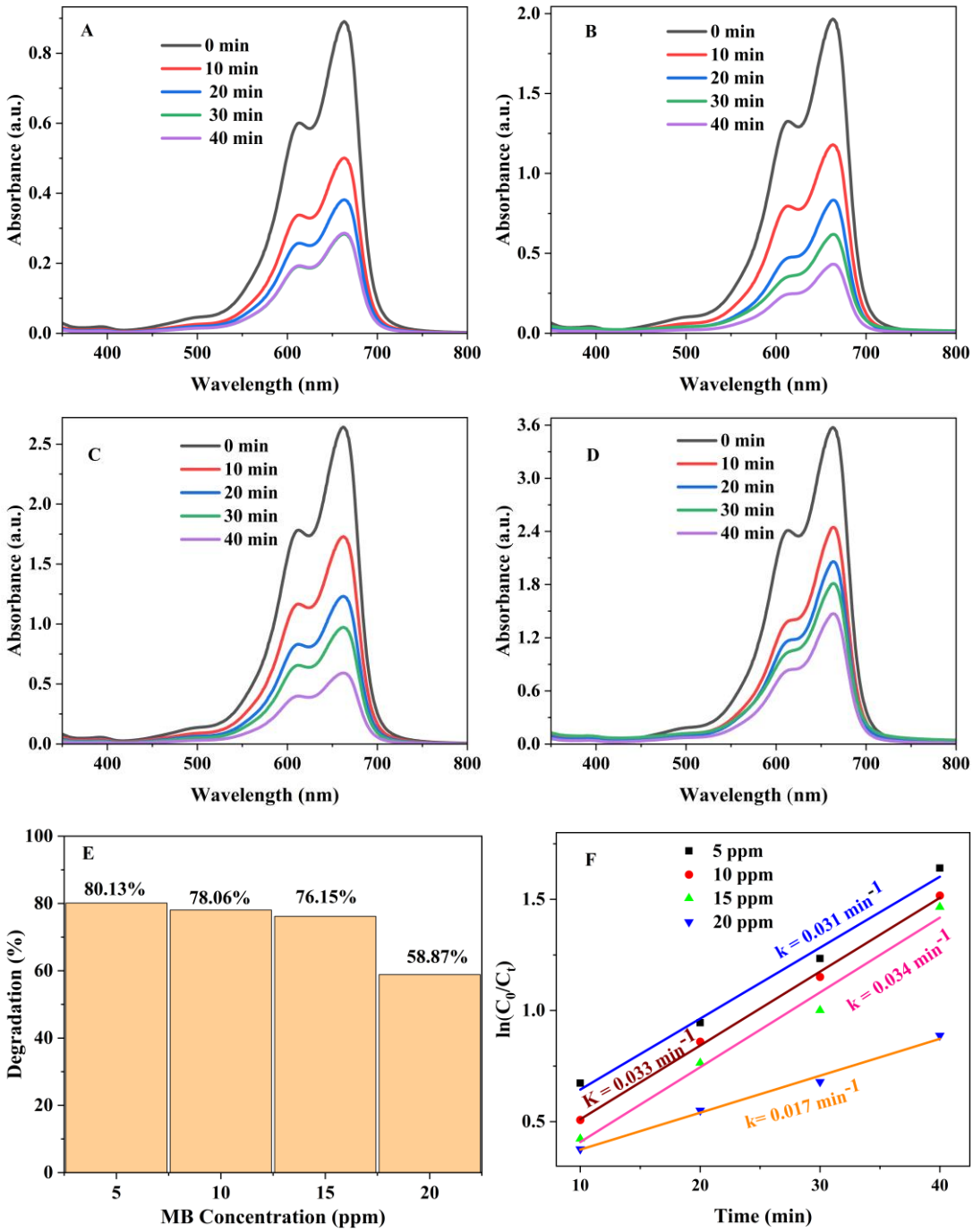

Figure 40. The UV-Vis absorption spectra of (A) 5 ppm, (B) 10 ppm, (C) 15 ppm, (D) 20 ppm of MB, (E) %degradation, and (F) pseudo-first-order kinetics.

4.3.6 Effect of Initial pH of the Solution

Another crucial factor in the photocatalytic removal of contaminants is the solution's pH. The pH of the solution has a substantial impact on the surface charge of the photocatalyst. To change its pH, 1 M NaOH solution was added to the MB dye solution.

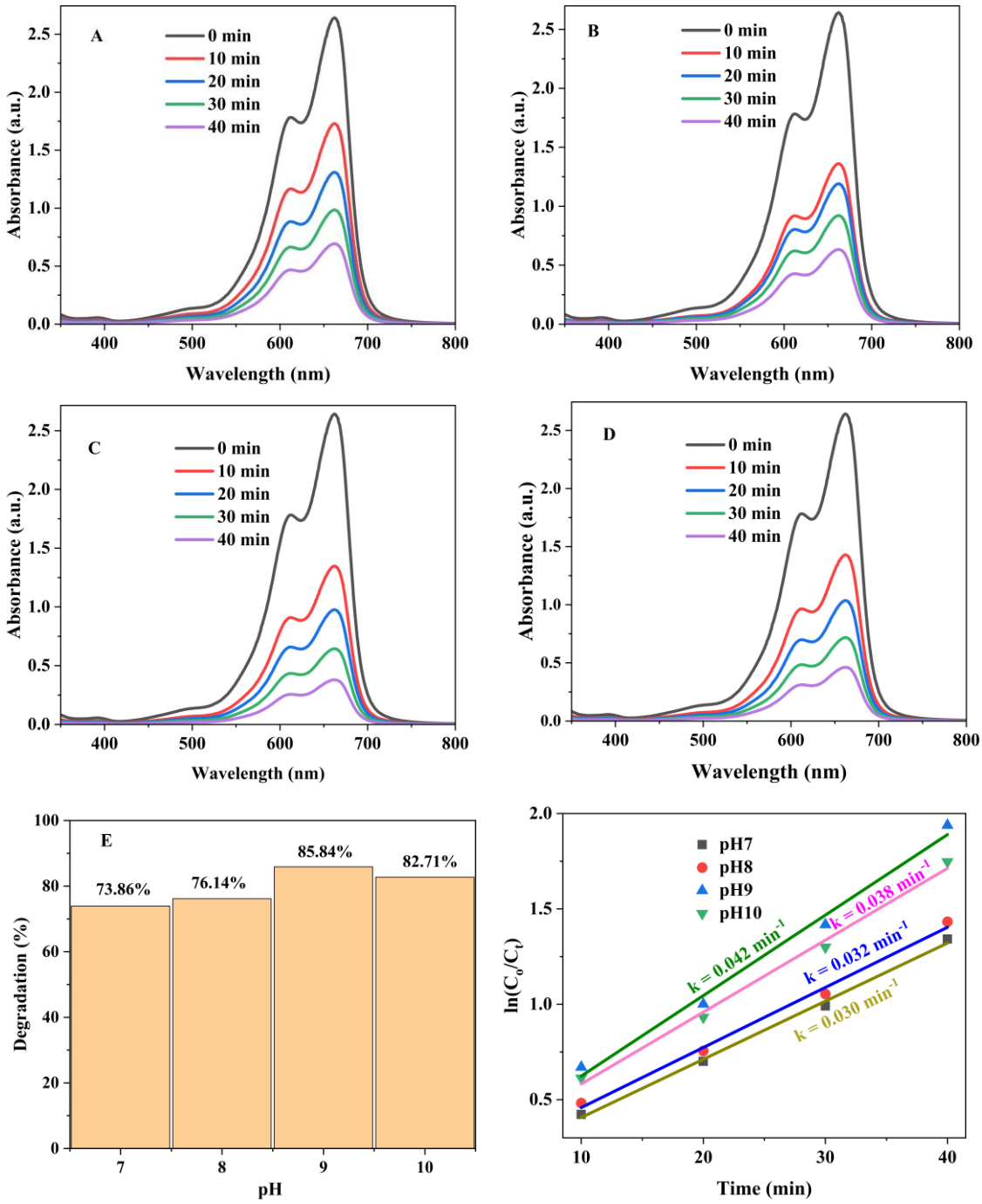

Figure 41. The UV-Vis absorption spectra for the degradation of MB dye at pH (A) 7, (B) 8, (C) 9, (D) 10, (E) %degradation, and (F) pseudo-first-order kinetics.

Then the effect of solution pH on the photocatalytic degradation activity was studied within the range of 7 – 10, based on the pH_{PZC} value of the adsorbent, at optimized dye concentration (15 ppm) and photocatalyst amount (20 mg/L) A greater photodegradation

efficiency was observed with increasing the pH of the solution from 7 to 9, then it decreased slightly. This could be because the TiO_2/CuO (1:1) NCs' surface strongly negative charge was protonated, losing its negatively charged surface property and decreasing in adsorbing cationic dye on the surface (Chaudhari *et al.*, 2018; Reza *et al.*, 2017; Tahir *et al.*, 2022). The maximum degradation efficacy was obtained at pH 9. The kinetics investigation of MB dye degradation employing 20 mg of TiO_2/CuO (1:1) NCs revealed a better fit with the pseudo-first-order model (R^2 = 0.994 and k = 0.042 min^{-1}) than with the pseudo-second-order model (R^2 = 0.991 and k = 0.021 $ppm^{-1}min^{-1}$(Figure 41 and Table 15).

Table 15. The degradation efficiency and rate of 20 mg TiO_2/CuO (1:1) NCs synthesized using 50 mL of IHL extract against 15 ppm of MB at pH 7, 8, 9, and 10 and a contact time of 40 min.

		Pseudo first order		Pseudo second order	
pH	Degradation (%)	Regression coefficient	Rate constant (min^{-1})	Regression coefficient	Rate constant ($ppm^{-1}min^{-1}$)
7	73.86	0.995	0.030	0.984	0.014
8	76.15	0.991	0.034	0.988	0.015
9	85.84	0.994	0.042	0.991	0.021
10	82.71	0.997	0.038	0.993	0.017

4.3.7 Effect of Contact Time

The results show the effect of contact time on the removal of MB at optimum conditions: 20 mg TiO_2/CuO (1:1) NCs dose, 15 ppm initial MB concentration, and pH 9 of the solution. The result shows that the rapid photodegradation of MB was observed in the first 60 min (Figure 42). The removal efficiency of MB using TiO_2/CuO (1:1) NCs was approximately 99 % at an irradiation time of 80 min. It was found that as the irradiation time increased, the percentage efficiency increased, and reached a maximum of 80 min. A similar result was reported by Bassim and his co-workers with a percentage degradation efficiency of 98.6% within 80 min of irradiation time on TiO_2/CuO (1:1) NC (Bassim *et al.*, 2023).

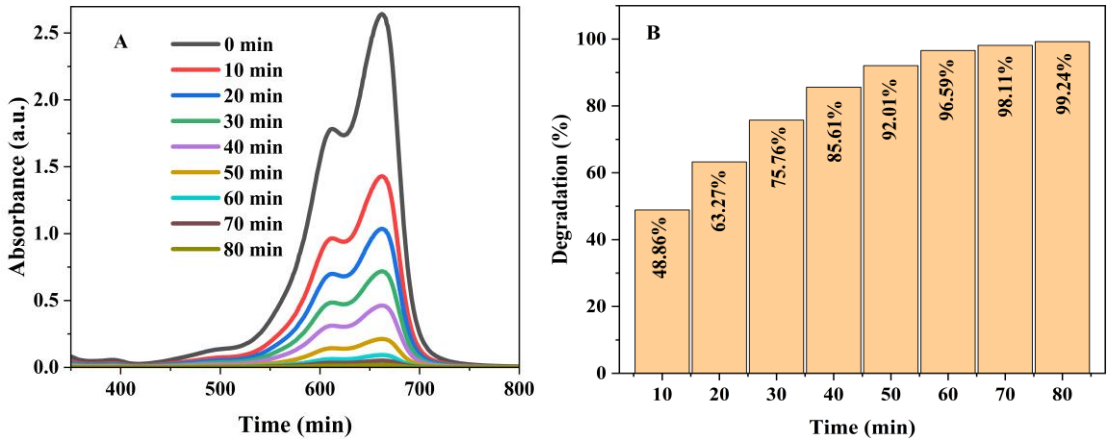

Figure 42. Effect of contact time on the degradation efficiency of 15 ppm of MB and catalyst dose of 20 mg at pH 9.

4.3.8 Degradation Efficiencies of TiO_2 NPs, TiO_2/CuO (1:1) NCs and TiO_2/ZnO (1:1) NCs

The photocatalytic performance efficiencies of TiO_2 NPs, TiO_2/CuO (1:1) NCs, and TiO_2/ZnO (1:1) NCs at the optimum initial MB dye concentration of 15 ppm, at pH 9 of the solution, and 20 mg catalyst dose were found to be 82%, 99%, and 94%, respectively (Figure 43). The result found that the TiO_2/CuO (1:1) NCs have greater degradation potential, compared to both TiO_2 NPs and TiO_2/ZnO (1:1) NCs. This could be attributed to good band edge alignment between CuO and TiO_2 in the nanocomposites. The degradation efficiency obtained using TiO_2/CuO (1:1) NCs agreed with the result reported by Kapoor & Rajput (Kapoor & Rajput, 2022). The kinetics investigation of MB dye degradation of TiO_2 NPs, TiO_2/CuO (1:1) NCs, and TiO2/ZnO (1:1) NCs showed a better fit with the pseudo-first-order model (Table 16).

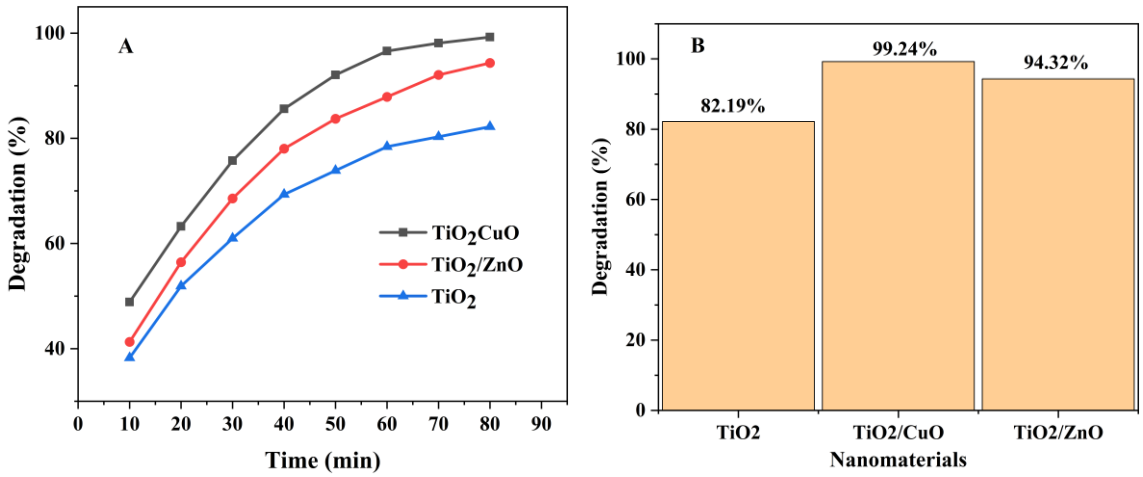

Figure 43. Degradation efficiency vs. time (A) and Degradation efficiency Vs. nanomaterials (B) of 20 mg TiO_2 NPs, TiO_2/CuO (1:1), and TiO_2/ZnO (1:1) NCs at 15 ppm initial MB concentration, 9 pH of the solution, and contact time of 80 min.

Table 16. Summary of rate constants and degradation efficiencies of TiO_2 NPs, TiO_2/CuO (1:1) NCs, and TiO_2/ZnO (1:1) NCs at optimized conditions.

		Pseudo first order		Pseudo second order	
Nanomaterials	Degradation (%)	Regression coefficient	Rate constant (min^{-1})	Regression coefficient	Rate constant ($ppm^{-1}min^{-1}$)
TiO_2	82.19	0.989	0.018	0.981	0.014
TiO_2/CuO (1:1)	99.24	0.997	0.059	0.992	0.0021
TiO_2/ZnO (1:1)	94.32	0.999	0.033	0.991	0.0018

4.3.9 Scavenging Test

When organic pollutants are photodegraded, reactive species such as holes (h+), superoxide radicals (O2−•), electrons (e^-), and hydroxyl radicals (OH•) are essential (Mugumo *et al.*, 2023). Therefore, the photocatalytic activities of TiO_2 NPs, TiO_2/ZnO (1:1) NCs, and TiO_2/CuO (1:1) NCs on the degradation of MB dye were studied in the presence of $AgNO_3$, EDTA-2Na (Bakry *et al.*, 2022), isopropanol (IPA) (Salesi & Nezamzadeh-Ejhieh, 2023), and acetonitrile (Saharudin *et al.*, 2018) as scavengers for e^-, h^+, $OH^•$ and $O_2^{-•}$, respectively. This experimental study was used to determine the relative contribution of reactive species.

Figure 44 displays the photocatalytic removal of MB dye using TiO_2 NPs, TiO_2/CuO (1:1) NCs, and TiO_2/ZnO (1:1) NCs in the presence of these radical scavengers at optimum conditions.

In the case of TiO_2 NPs, the results showed that $OH^{\bullet}$ were the main reactive species because of IPA decreased degradation efficiency by approximately 31%. Upon the addition of acetonitrile, the degradation efficiency decreased to 38%, which indicates superoxide radicals ($O_2^{-\bullet}$) played a major role in the photodegradation of MB. The decrement of degradation efficiency to 54% due to the addition of holes scavenger (EDTA-2Na) revealed the greater contribution of holes (h^+) in the degradation mechanism. In general, the photocatalytic activity of TiO_2 on MB dye was driven by the reactive species in a sequence of $OH^{\bullet} > O_2^{\bullet-} > h^+ > e^-$, and similar results were reported by Saharudin et al (Saharudin *et al.*, 2018). The scavenger test for TiO_2/CuO NCs showed the contributions of active species were in the order of $O_2^{\bullet-} > OH^{\bullet} > h^+ > e^-$, indicating the superoxide radicals played the major role. In another way, the radical scavengers revealed that the photocatalytic activity of TiO_2/ZnO NC was dominantly controlled by the holes in the order of $h^+ > OH^{\bullet} > O_2^{\bullet-} > e^-$ (Figure 44).

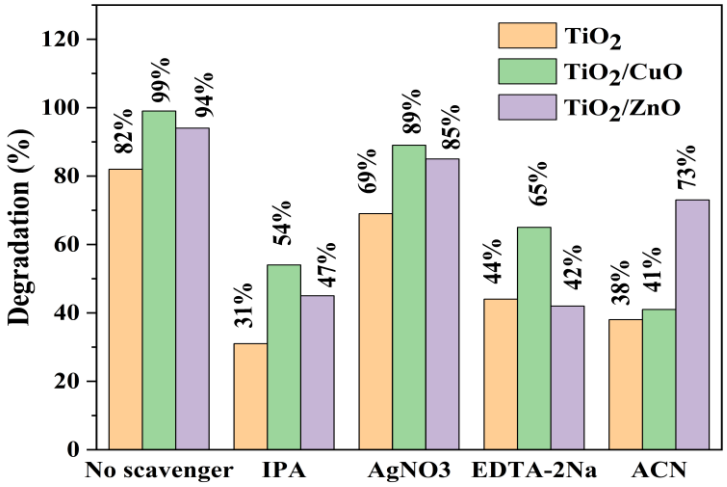

Figure 44. The effect of radical scavengers on the photodegradation ability of TiO_2 NPs, TiO_2/CuO (1:1) NCs, and TiO_2/ZnO (1:1) NCs.

4.3.10 Reusability Test

As presented in Figure 45, the reusability test of TiO_2 NPs, TiO_2/CuO, and TiO_2/ZnO NCs showed good stability in three cycles. The percent removal efficiencies for TiO_2 NPs in the 1st, 2nd, and 3rd cycles were found to be 78%, 75%, and 71%, respectively. Similarly,

TiO_2/CuO NCs showed 98%, 97%, and 95% degradation efficiency for 1st, 2nd, and 3rd cycles, respectively. The reusability test for TiO_2/ZnO NCs was recorded as 93%, 91%, and 89% for 1st, 2nd, and 3rd cycles, respectively.

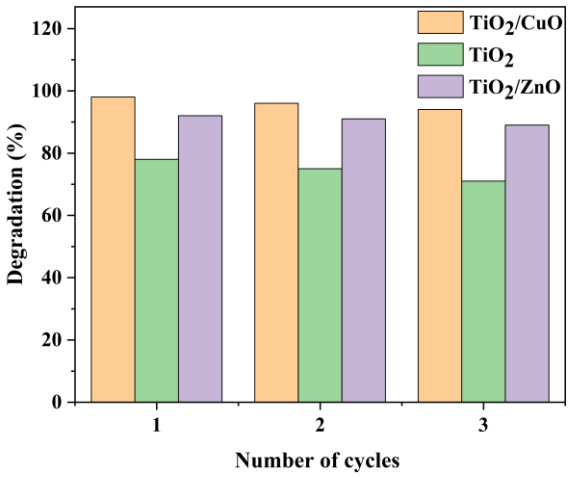

Figure 45. Reusability test of TiO_2 NPs, TiO_2/CuO (1:1) NCs, and TiO_2/CuO (1:1) NCs for photodegradation of MB dye.

4.3.11 Mechanism of Photocatalysis in TiO_2/CuO (1:1) NCs

Forming a heterojunction between metal oxide semiconductors can effectively aid charge transfer and prolong electron-hole relaxation without recombination. During contact, first, the Fermi level redistribution occurs until equilibration occurs due to differences in the work function. Then, the development of an internal electric field, or accumulated layer, between the two semiconductor interfaces, as well as band edge bending, occurred (G. Sun *et al.*, 2023). The proposed photocatalytic degradation mechanism for TiO_2/CuO NCs based on the Mott-Schottky and UV-vis-DRS analysis results is shown in Figure 46 and Equations 32-40. Here, the holes migrate from the more positive VB potential of TiO_2 to CuO's less positive VB potential. The electrons migrate from a more negative CB potential of CuO to a less negative CB potential of TiO_2, similar to the results reported by Solano (Solano *et al.*, 2024). Then, molecular oxygen reacts with the electron and is reduced to $^{\bullet}O_2^-$, while the holes from the valence band of TiO_2 react with water and produce OH radicals. Consecutively, the water molecules react with photogenerated h^+ or superoxide radicals (O_2^-) at the surface of the photocatalyst and change to OH^-. The holes react with the produced OH^- on the photocatalyst surface and generate OH radicals. The O_2 also

reacts with photoexcited electrons and converted to superoxide radicals, a highly oxidizing agent. The generated $^{\bullet}O_2^-$ radicals can directly react with MB dye or produce OH radicals by reacting with photogenerated electrons and hydrogen ions. Since $^{\bullet}OH$ is a strongly oxidizing agent, it finally degrades the MB dye (Kermani *et al.*, 2023; Kumari *et al.*, 2023; Salem *et al.*, 2023; Tahir *et al.*, 2022).

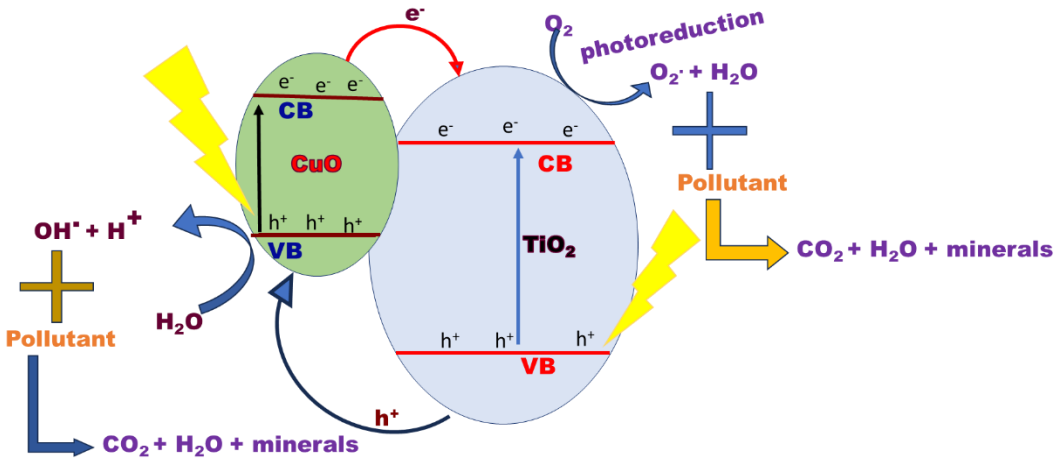

Figure 46. Mechanism of the photoexcited e^-/h^+ separation process of TiO_2/CuO NCs and its photocatalysis mechanism against MB dye.

$$TiO_2/\mathrm{CuO} + \mathrm{hv} \rightarrow TiO_2/\mathrm{CuO}\ (h^+_{VB} + e^-_{CB}) \quad (32)$$

$$e^-_{CB} + O_2 \rightarrow O_2^{\bullet -} \quad (33)$$

$$O_2^{\bullet -} + H^+ \rightarrow HO_2^{\bullet} \quad (34)$$

$$2HO_2^{\bullet} \rightarrow H_2O_2 + O_2 \quad (35)$$

$$2HO_2^{\bullet} \rightarrow H_2O_2 + O_2^{\bullet -} \rightarrow OH^{\bullet} + O_2 + OH^- \quad (36)$$

$$h^+_{VB} + OH^- \rightarrow OH^{\bullet} \quad (38)$$

$$h^+_{VB} + H_2O \rightarrow OH^{\bullet} + H^+ \quad (39)$$

$$OH^{\bullet} + \mathrm{MB} \rightarrow CO_2 + H_2O + other\ mineral\ ions \quad (40)$$

4.4 DSSC Devices Performance

The efficiencies of DSSC devices depend on different factors, such as the types of dye, counter electrode, electrolyte, and photoanode materials. In this work, the green synthesized TiO_2 NPs, TiO_2/CuO (1:1) NCs, and TiO_2/ZnO (1:1) NCs photoanodes were

used to fabricate four selected plant dye DSSC devices. Also, the standard paste photoanode was used for the comparison.

4.4.1 Performance of TiO_2 NPs Photoanode

Table 17 and the J-V curves in Figure 47 show the results obtained using different natural pigments. The DSSC performance of the dye extract of IHR (mix) showed the highest efficiency of 1.03% with V_{OC}, fill factor, and J_{sc} of 0.44 V, 45.97%, and 5.09 $mAcm^{-2}$, respectively, using synthesized TiO_2 NPs photoanode. In contrast, IHF(w) revealed the lowest efficiency of 0.53% with V_{OC} of 0.32 V, a fill factor of 48.47%, and J_{sc} of 3.39 $mAcm^{-2}$. However, both IHF(w) and IHR (mix) are extracted from the same flower and root, respectively, the DSSC devices performance of IHR (mix) is almost double that of IHF (w). This variation in efficiency is an implication of the variation of types and quantity of phytochemicals in different parts of a given plant (Akullo *et al.*, 2023; Okello *et al.*, 2021).

Table 17. The DSSC device performance of the TiO_2 photoanode.

Photoanode	Dye extract	J_{sc} ($mAcm^{-2}$)	Voc (V)	J_{max} ($mAcm^{-2}$)	V_{max} (V)	FF (%)	η (%)
TiO_2	TRF(w)	3.81	0.29	2.61	0.11	44.88	0.60
	TRF(mix)	3.95	0.33	2.71	0.22	45.74	0.61
	IHF(w)	3.39	0.32	2.39	0.22	48.47	0.53
	IHF(mix)	3.65	0.34	2.51	0.24	48.54	0.60
	IHR(w)	4.95	0.30	3.45	0.29	44.70	1.01
	IHR(mix)	5.09	0.44	3.55	0.29	45.97	1.03
	RSF(w)	4.28	0.35	2.97	0.24	47.58	0.71
	RSF(mix)	4.56	0.39	3.16	0.27	47.96	0.85

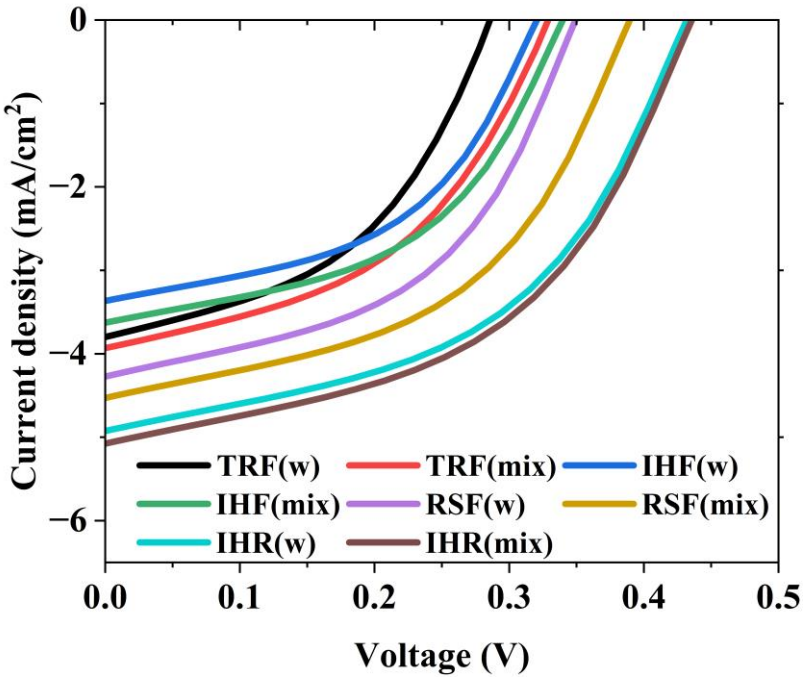

Figure 47. The J-V curves of DSSC devices for TiO_2 NPs photoanode sensitized with dye extracts.

In general, the measured DSSC devices efficiencies of IHF(w), IHF(mix), TRF(w), TRF(mix), RSF(w), RSF(mix) IHR(w), and IHR(mix) using the green synthesized TiO_2 NPs photoanode were found to be 0.53, 0.60, 0.60, 0.61, 0.71, 0.85, 1.01, and 1.03, respectively.

4.4.2 Performance of TiO_2/CuO (1:1) NC Photoanode

The photo-electrochemical performance of the dye extract of IHR (mix) obtained from the fabricated DSSC devices using green synthesized TiO_2/CuO (1:1) NCs photoanode showed the highest efficiency of 1.70% with V_{OC} of 0.47 V, a fill factor of 47.51%, and Jsc of 7.61 $mAcm^{-2}$ (Figure 48, Table 18). When compared to the TiO_2 NPs, the efficiency of TiO_2/CuO (1:1) NCs showed approximately 64% increment. This could be due to the larger surface area of TiO_2/CuO (1:1) NCs as discussed in the BET surface area analysis section.

Table 18. The DSSC devices performance of the TiO_2/CuO (1:1) photoanode.

Photoanode	Dye extract	J_{sc} ($mAcm^{-2}$)	Voc (V)	J_{max} ($mAcm^{-2}$)	V_{max} (V)	FF (%)	η (%)
TiO_2/CuO (1:1)	TRF(w)	6.56	0.29	4.56	0.19	45.54	0.87
	TRF(mix)	6.73	0.35	4.70	0.23	45.89	1.08
	IHF(W)	5.67	0.35	3.91	0.24	47.29	0.94
	IHF(mix)	6.25	0.37	4.39	0.25	47.46	1.10
	IHR(W)	7.55	0.46	5.22	0.31	46.59	1.62
	IHR(mix)	7.61	0.47	7.31	0.32	47.51	1.70
	RSF(w)	6.83	0.38	4.68	0.26	46.88	1.22
	RSF(mix)	7.22	0.42	4.98	0.29	47.63	1.44

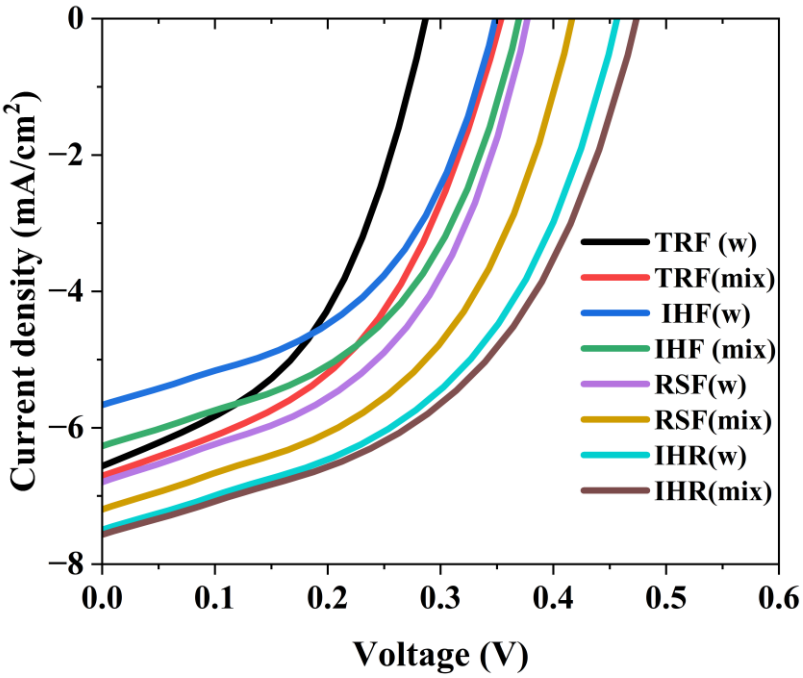

Figure 48. The J-V curves of DSSC devices of TiO_2/CuO (1:1) NCs photoanode sensitized dye extracts.

4.4.3 Performance of TiO_2/ZnO (1:1) NCs Photoanode

In the same way, the highest efficiency was recorded for the device sensitized with the dye extract of IHR (mix) having an efficiency of 1.43%. This value exceeds by 38% compared to the efficiency of the TiO_2 NPs photoanode (Figure 49, Table 19).

Table 19. The DSSC devices performance of the TiO_2/ZnO (1:1) photoanode.

Photoanode	Dye extract	J_{sc} ($mAcm^{-2}$)	Voc (V)	J_{max} ($mAcm^{-2}$)	V_{max} (V)	FF (%)	η (%)
TiO_2/ZnO (1:1)	TRF(w)	5.79	0.29	3.91	0.20	46.57	0.78
	TRF(mix)	5.93	0.35	4.03	0.24	46.60	0.97
	IHF(W)	5.07	0.34	3.48	0.23	46.43	0.80
	IHF(mix)	5.59	0.36	3.89	0.25	48.33	0.97
	IHR(W)	6.70	0.43	4.72	0.29	47.51	1.37
	IHR(mix)	6.75	0.44	4.77	0.30	48.18	1.43
	RSF(W)	6.07	0.37	4.20	0.25	46.75	1.05
	RSF(mix)	6.41	0.40	4.48	0.27	47.18	1.21

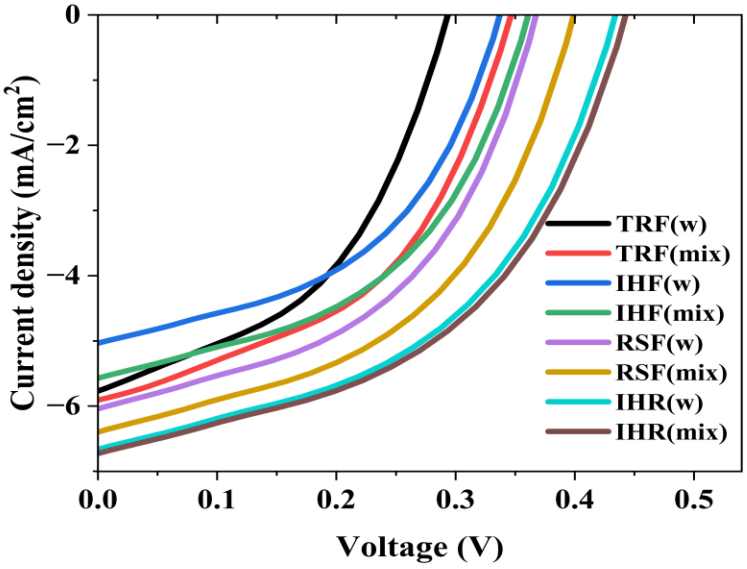

Figure 49. The J-V curves of DSSC devices of TiO_2/ZnO (1:1) NCs photoanode sensitized with dye extracts.

This performance improvement could be due to the deduced bandgap energy, compared to individual metal oxides (TiO_2 and ZnO), increasing the lifetime of charge carriers, and surface coverage of the sensitizing dye over TiO_2/ZnO (1:1) NCs (Mahmoudabadi & Eslami, 2019).

4.4.4 Performance of T/R Photoanode

The V_{oc} and J_{sc} of the T/R devices are the highest compared to the device fabricated from the green synthesized TiO_2 NPs, TiO_2/CuO (1:1) NCs, and TiO_2/ZnO (1:1) NCs (Figure 50, Table 20).

Table 20. The DSSC devices performance of the T/R photoanode.

Photoanode	Dye extract	J_{sc} ($mAcm^{-2}$)	Voc (V)	J_{max} ($mAcm^{-2}$)	V_{max} (V)	FF (%)	η (%)
T/R	TRF(w)	7.22	0.31	4.81	0.21	45.13	1.01
	TRF(mix)	7.35	0.39	5.09	0.27	47.94	1.37
	IHF(w)	4.56	0.36	4.34	0.25	66.06	1.09
	IHF(mix)	5.13	0.37	4.40	0.26	60.27	1.14
	IHR(w)	8.38	0.48	5.73	0.33	47.01	1.89
	IHR (mix)	8.43	0.49	5.83	0.34	47.99	1.99
	RSF(w)	7.96	0.39	5.71	0.27	49.66	1.54
	RSF(mix)	7.98	0.41	5.48	0.28	46.90	1.55

The DSSC conversion efficiency of this device has the highest record of 1.99% sensitized by IHR (mix) dye. This value exceeds 93%, 39%, and 23%, compared to TiO_2 NPs, TiO_2/ZnO (1:1) NCs, and TiO_2/CuO (1:1) NCs, respectively. This suggests that the TiO_2/CuO (1:1) NCs photoanode agreed well with the standard paste photoanode. The performance of the DSSC devices is also significantly influenced by the photoanode materials' surface area and porosity. The surface area and porosity of the charge transport layers regulate the dye loading capacity of the DSSC device. These factors improve the electrolyte injection and allow light trapping for a more effective charge transport process (Ramanathan *et al.*, 2022).

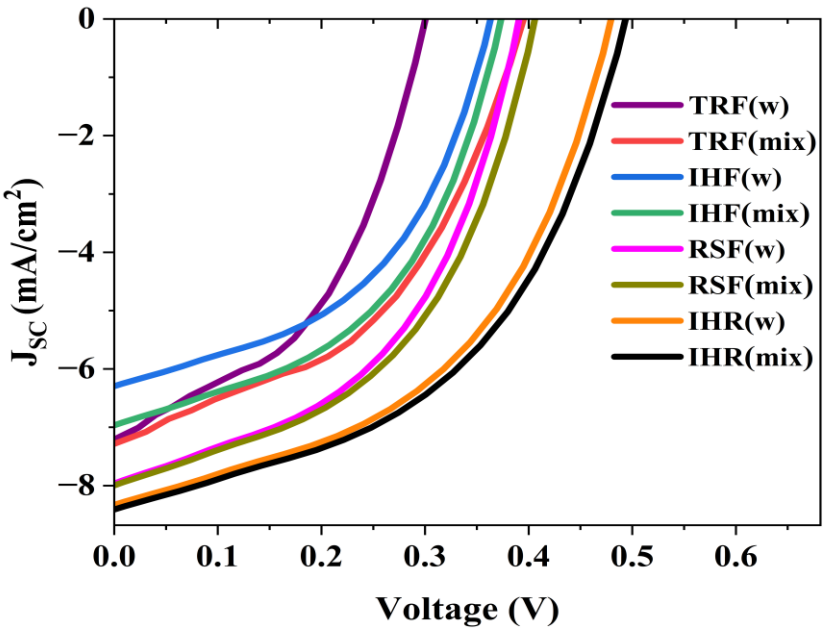

Figure 50. The J-V curves of DSSC devices of T/R paste photoanode sensitized with dye extracts.

4.4.5 Stability of DSSC Devices

The stability of the DSSC devices fabricated with a natural dye sensitizer is one of the most significant challenges. Among all the devices fabricated using synthesized nanomaterials and natural dye, IHR(mix) showed the highest stability. This could be attributed to the sticky nature of the extract of IHR. The PCE efficiencies of these devices were 0.76, 1.08, and 1.29 % after 72 hr for TiO_2 NPs, TiO_2 /ZnO (1:1) NCs, and TiO_2/CuO (1:1) NCs, respectively. In general, DSSC devices fabricated from TiO_2/CuO (1:1) NCs and IHR(mix) showed the highest stability as compared to TiO_2 NPs and TiO_2/ZnO (1:1) NCs. Tables 21-24 show the photovoltaic performance of the fabricated DSSCs stability for 24, 48, and 72 hr.

Table 21. The efficiencies of fabricated DSSC devices after 24, 48, and 72 hr for the TiO_2 NPs photoanode.

Photoanode	Dye extract	Efficiency η (%) after			
		0 hr	24 hr	48 hr	72 hr
TiO_2 NPs	TRF(w)	0.60	0.37	0.15	0.09
	TRF(mix)	0.61	0.38	0.21	0.12
	IHF(w)	0.53	0.28	0.19	0.10
	IHF(mix)	0.60	0.33	0.24	0.20
	IHR(w)	1.01	0.95	0.84	0.73
	IHR(mix)	1.03	0.95	0.87	0.76
	RSF(w)	0.71	0.43	0.24	0.12
	RSF(mix)	0.85	0.51	0.28	0.15

Table 22. The efficiencies of fabricated DSSC devices after 24, 48, and 72 hr for TiO_2 /CuO (1:1) NCs photoanode.

Photoanode	Dye extract	Efficiency η (%) after			
		0 hr	24 hr	48 hr	72 hr
TiO_2/CuO (1:1) NCs	TRF(w)	0.87	0.45	0.24	0.13
	TRF(mix)	1.08	0.56	0.32	0.18
	IHF(W)	0.94	0.65	0.38	0.29
	IHF(mix)	1.10	0.72	0.41	0.35
	IHR(W)	1.62	1.44	1.31	1.24
	IHR(mix)	1.70	1.53	1.42	1.29
	RSF(w)	1.22	1.08	0.75	0.23
	RSF(mix)	1.44	1.17	0.85	0.42

Table 23. The efficiencies of fabricated DSSC devices after 24, 48, and 72 hr for TiO_2/ZnO (1:1) NCs photoanode.

Photoanode	Dye extract	Efficiency η (%) after			
		0 hr	24 hr	48 hr	72 hr
TiO_2/ZnO (1:1) NCs	TRF(w)	0.78	0.42	0.21	0.11
	TRF(mix)	0.97	0.47	0.28	0.14
	IHF(W)	0.80	0.51	0.37	0.25
	IHF(mix)	0.97	0.53	0.41	0.31
	IHR(W)	1.37	1.24	1.17	1.01
	IHR(mix)	1.43	1.28	1.19	1.08
	RSF(W)	1.05	0.73	0.32	0.15
	RSF(mix)	1.21	0.78	0.37	0.21

Table 24. The efficiencies of fabricated DSSC devices after 24, 48, and 72 hr for T/R photoanode.

photoanode	Dye extract	Efficiency η (%) after			
		0 hr	24 hr	48 hr	72 hr
T/R	TRF(w)	1.01	0.63	0.31	0.18
	TRF(mix)	1.37	0.69	0.34	0.21
	IHF(w)	1.07	0.54	0.37	0.19
	IHF(mix)	1.09	0.56	0.41	0.23
	IHR(w)	1.89	1.68	1.53	1.47
	IHR (mix)	1.99	1.79	1.67	1.58
	RSF(w)	1.54	1.08	0.75	0.41
	RSF(mix)	1.55	1.12	0.81	0.43

4.4.6 IPCE

The quality of the solar cell's charge transport and absorption at a specific wavelength are measured by the incident monochromatic photon to current conversion efficiency, or IPCE (Tadesse, 2019). IPCE measurements were done to realize the photocurrent generation of

the cells based on different photoanodes. The plots of IPCE versus wavelength of the DSSC devices sensitized with IHR(mix) dye extract fabricated using TiO_2 NPs, TiO_2/CuO (1:1) NCs, and TiO_2/ZnO (1:1) NCs and T/R paste. IPCE measurements were done to realize the photocurrent generation of the cells based on different photoanodes. The percentage of the IPCE achieved by the cells showed an increment as the TiO_2 NPs photoanode was replaced by TiO_2/ZnO (1:1) NCs, TiO_2/CuO (1:1) NCs, and T/R paste, respectively (Figure 51 and Table 25). Among the synthesized nanomaterials in this work, the most efficient DSSC device with TiO_2/CuO (1:1) NCs photoanode has an IPCE% value of 56.71% at a wavelength of 453 nm. According to Shah et al., the enhancement of the DSSC performance might be because of the improvement of charge injection and photocurrent. Consequently, the electron recombination in the electrolyte is reduced, and efficiency increases (S. Shah *et al.*, 2019).

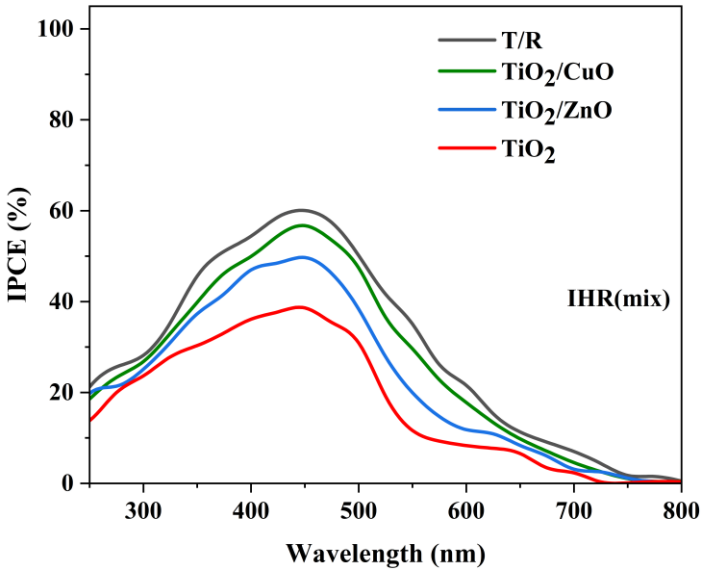

Figure 51. Effect of different photoanodes on the IPCE performance of DSSC devices sensitized with IHR(mix).

Table 25. Effect of different photoanodes on the IPCE performance of DSSC devices sensitized with IHR(mix).

Photoanode	Dye extract	Maximum IPCE (%)	Wavelength (nm)
TiO_2	IHR(mix)	39.12	448
TiO_2/CuO (1:1)	IHR(mix)	56.71	453
TiO_2/ZnO (1:1)	IHR(mix)	49.82	451
T/R	IHR(mix)	60.25	453

4.4.7 Mechanism of DSSC Devices

The possible mechanism of energy conversion in DSSC is shown in Figure 52A-C. The process of energy conversion begins with light absorption, in which photons from the sun are absorbed by a dye, which causes electronic excitation and generates an exciton (Equation 41). This is then followed by electron injection, whereby excited electrons are transported from the dye LUMO into the semiconductor's conduction band, assisting charge separation (Equation 42). After injection, the dye is oxidized and requires dye regeneration, which occurs when electrons from the electrolyte are transported back to the dye, restoring its initial condition (Equation 43). Meanwhile, the electron transport process comprises the passage of electrons via the semiconductor material towards the external circuit, providing an electric current (Equation 44). Finally, electrolyte reduction occurs when the electrolyte, a redox couple (iodide/triiodide), and accept electrons from the exterior circuit, in the DSSC at the counter electrode (Equation 45).

Light absorption :

$$Dye_{ad} + h\nu \rightarrow Dye_{ad}^{*} \quad (41)$$

Electron injection:

$$Dye_{ad}^{*} \rightarrow Dye_{ad}^{+} + e_{injected}^{-} \quad (42)$$

Dye regeneration:

$$Dye_{ad}^{+} + \frac{3}{2}I^{-} \rightarrow Dye_{ad} + \frac{1}{2}I_3^{-} \quad (43)$$

Electron transportation:

$$e_{TiO_2/CuO}^{-} + FTO \rightarrow e_{FTO}^{-} + TiO_2/\text{CuO} \quad (44)$$

Electrolyte reduction reaction:

$$I_3^{-} + e^{-} \rightarrow 3I^{-} \quad (45)$$

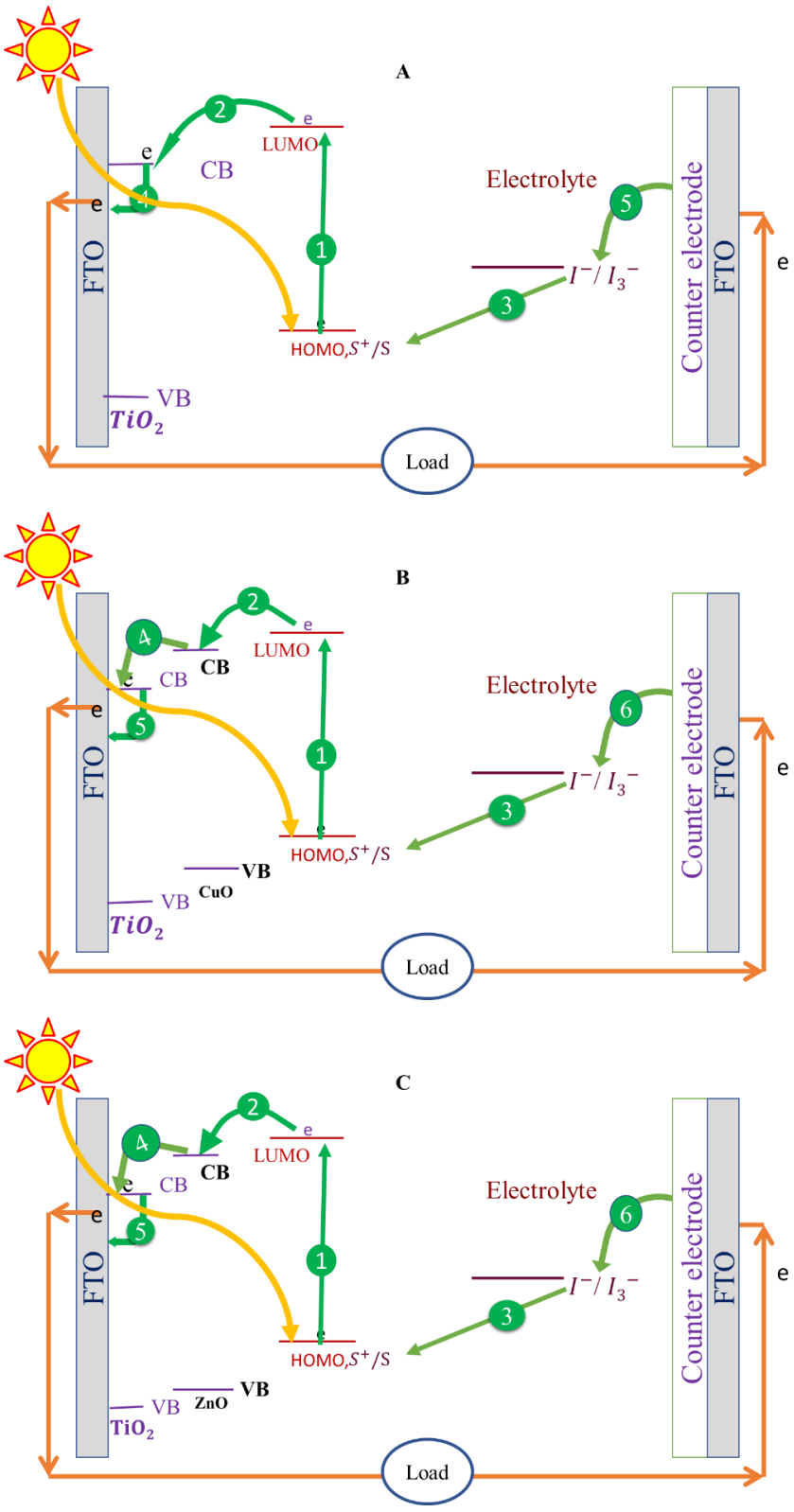

Figure 52. Proposed mechanism of DSSC energy conversion using (A)TiO_2 NPs, (B)TiO_2/CuO (1:1) NCs, and (C)TiO_2/CuO (1:1) NCs photoanodes

5 CONCLUSIONS AND RECOMMENDATIONS

5.1 Conclusions

In this work, TiO_2 NPs, TiO_2/CuO (1:1) NCs, and TiO_2/ZnO (1:1) NCs were synthesized using IHL extract. The optical, crystallinity, textural, morphological, and compositional properties of synthesized materials are also effectively characterized using advanced characterization techniques such as UV-Vis-DRS, XRD, FTIR, BET, SEM/EDX, HR/TEM, XPS, Raman, and electrochemical methods. The XRD pattern analysis revealed TiO_2 polymorphism with clear CuO and ZnO peaks, further confirmed by the Raman spectroscopic results. The XPS analysis confirms the existence of TiO_2, CuO, and ZnO phases in the NCs with oxidation states of +4, +2, and +2 for Ti, Cu, and Zn, respectively. The SEM and EDX mapping depicted some agglomerated spherical morphology, enhanced porosity, and the presence of Cu, Ti, Zn, and O elements. The average particle sizes from TEM analysis proved the formation of nanomaterials (<100 nm). From UV-Vis analysis, the NCs showed a redshift compared to pristine TiO_2 NPs. FTIR confirmed the presence of the O–H group and C–O carbonyl group in the extracted dyes, so the dye molecules can bond with synthesized nanostructures and transfer excited electrons from the sensitizer into the conduction band of metal oxides.

The potentials of the synthesized materials were tested for methylene blue dye degradation and DSSC applications. Under optimal conditions, the TiO_2/CuO (1:1) NCs exhibited the maximum degrading efficiency of 99% and showed better performance than the pristine TiO_2 NPs (82%) and TiO_2/ZnO (1:1) NCs (94%). It was found that the photodegradation activity of MB dye was better fitted with pseudo-first-order, and TiO_2/CuO (1:1) NCs showed the highest rate constant of 0.059 min^{-1} compared to TiO_2NPs (0.018 min^{-1}) TiO_2/ZnO (1:1) NCs (0.033 min^{-1}). The reusability test of the photocatalysts revealed promising stability in removing pollutants.

The increase in efficiency was observed when the DSSC devices were fabricated using the green synthesized photoanodes in the order of TiO_2 NPs < TiO_2/ZnO (1:1) NC< TiO_2/CuO (1:1) NCs for all dye extracts as sensitizers used in this work. Among all fabricated DSSCs using synthesized photoanodes, TiO_2/CuO (1:1) NCs sensitized with IHR(mix) showed the highest efficiency of 1.70% and IPCE of 56.71%. This result agrees with DSSC devices regarding the commercial T/R paste photoanode (60.25%). The improved performance of

DSSC devices in TiO_2/ZnO (1:1) NCs and TiO_2/CuO (1:1) NCs compared to the pristine TiO_2 NPs was also attributed to the formation of heterojunction structures and the good energy level alignments between the formed nanocomposites. In general, in this work, the green synthesized NCs using IHL extract showed good photocatalytic degradation of MB dye. In addition to photocatalytic application, they showed good DSSC energy conversion efficiency when used as photoanode materials.

5.2 Recommendations

The nanomaterials synthesized in this work should be tested for other applications like antimicrobial activity, sensor, and supercapacitor applications. DFT calculation should be performed to analyze the adsorption energy of dye on the nanostructure surface, binding sites of different natural dyes on TiO_2, TiO_2/CuO, and TiO_2/ZnO surfaces, and optimal orientation of nanostructure-dye. Understanding these interactions can lead to improved dye loading and efficiency. It is recommended to isolate phytochemicals to know exactly what structures are in each plant and draw the exact mechanism of interaction of each component with the nanostructures.

REFERENCES

Abbasi, Z., Shamsaei, E., Leong, S. K., Ladewig, B., Zhang, X., & Wang, H. (2016). Effect of carbonization temperature on adsorption property of ZIF-8 derived nanoporous carbon for water treatment. *Microporous and Mesoporous Materials*, *236*, 28-37.

Abbood, H. K., & Ali, N. A. (2023). Studying of the structural and optical properties of titanium dioxide nanoparticles prepared by chemical method. *Journal of Optics*, *22*(2), 381.

Abebe, B., Murthy, H. A., Zereffa, E. A., & Adimasu, Y. (2021). Synthesis and characterization of ZnO/PVA nanocomposites for antibacterial and electrochemical applications. *Inorganic and Nano-Metal Chemistry*, *51*(8), 1127-1138.

Abebe, B., Zereffa, E. A., & Murthy, H. A. (2020). Synthesis of poly (vinyl alcohol)-aided ZnO/Mn2O3 nanocomposites for acid orange-8 dye degradation: mechanism and antibacterial activity. *ACS omega*, *6*(1), 954-964.

Abrol, S., Bhargava, C., & Sharma, P. (2021). Efficiency enhancement of Dye-Sensitized Solar Cells using Gel Polymer Electrolytes.

Abrol, S. A., Bhargava, C., & Sharma, P. K. (2021). Fabrication of DSSC using doctor blades method incorporating polymer electrolytes. *Materials Research Express*, *8*(4), 045010.

Abu Talip, R. A., Yahya, W. Z. N., & Bustam, M. A. (2020). Ionic liquids roles and perspectives in electrolyte for dye-sensitized solar cells. *Sustainability*, *12*(18), 7598.

Aduloju, K. A., Shitta, M. B., & Simiyu, J. (2011). Effect of extracting solvents on the stability and performances of dye-sensitized solar cell prepared using extract from Lawsonia Inermis.

Afonso, A. F., Pereira, O. R., & Cardoso, S. M. (2020). Health-promoting effects of Thymus phenolic-rich extracts: Antioxidant, anti-inflammatory and antitumoral properties. *Antioxidants*, *9*(9), 814.

Agidew, M. G. (2022). Phytochemical analysis of some selected traditional medicinal plants in Ethiopia. *Bulletin of the National Research Centre*, *46*(1), 87.

Ahmad, M. S., Pandey, A. K., & Abd Rahim, N. (2017). Advancements in the development of TiO2 photoanodes and its fabrication methods for dye sensitized solar cell (DSSC) applications. A review. *Renewable and Sustainable Energy Reviews*, *77*, 89-108.

Ahmad, W., Jaiswal, K. K., & Soni, S. (2020). Green synthesis of titanium dioxide (TiO_2) nanoparticles by using Mentha arvensis leaves extract and its antimicrobial properties. *Inorganic and Nano-Metal Chemistry*, *50*(10), 1032-1038.

Akerdi, A. G., Bahrami, S. H., & Pajootan, E. (2020). Modeling and optimization of Photocatalytic Decolorization of binary dye solution using graphite electrode modified with Graphene oxide and TiO_2. *Journal of Environmental Health Science and Engineering*, *18*, 51-62.

Akullo, J. O., Kiage-Mokua, B. N., Nakimbugwe, D., & Kinyuru, J. (2023). Phytochemical profile and antioxidant activity of various solvent extracts of two varieties of ginger and garlic. *Heliyon*, *9*(8).

Al-Alwani, M. A., Mohamad, A. B., Kadhum, A. A. H., Ludin, N. A., Safie, N., Razali, M.,…Sopian, K. (2017). Natural dye extracted from Pandannus amaryllifolius leaves as sensitizer in fabrication of dye-sensitized solar cells. *Int. J. Electrochem. Sci*, *12*(1), 747-761.

Al-Maliky, E. A., Gzar, H. A., & Al-Azawy, M. G. (2021). Determination of point of zero charge (PZC) of concrete particle adsorbents. *IOP Conference Series: Materials Science and Engineering*, *31*(1), 841-860.

Al-Musawi, T. J., Yilmaz, M., Mohebi, S., & Balarak, D. (2022). Ultraviolet radiation/persulfate/hydrogen peroxide treatment system for the degradation of acid blue 80 dye from a batch flow chemical reactor: effects of operational parameters, mineralization, energy consumption, and kinetic studies. *Energy, Ecology and Environment*, *7*(6), 630-640.

Al-Taweel, S. S., & Saud, H. R. (2016). New route for synthesis of pure anatase TiO_2 nanoparticles via utrasound-assisted sol-gel method. *J. Chem. Pharm. Res*, *8*(2), 620-626.

Alami, A. H., Aokal, K., Zhang, D., Taieb, A., Faraj, M., Alhammadi, A.,…Irimia-Vladu, M. (2019). Low-cost dye-sensitized solar cells with ball-milled tellurium-doped graphene as counter electrodes and a natural sensitizer dye. *International Journal of Energy Research*, *43*(11), 5824-5833.

Alamier, W. M., DY Oteef, M., Bakry, A. M., Hasan, N., Ismail, K. S., & Awad, F. S. (2023). Green Synthesis of Silver Nanoparticles Using Acacia ehrenbergiana Plant Cortex Extract for Efficient Removal of Rhodamine B Cationic Dye from Wastewater and the Evaluation of Antimicrobial Activity. *ACS omega*, *33*(21), 6823-6834.

Alhalili, Z. (2022). Green synthesis of copper oxide nanoparticles CuO NPs from Eucalyptus Globoulus leaf extract: Adsorption and design of experiments. *Arabian Journal of Chemistry*, *15*(5), 103739.

Ali, A., Sadia, M., Azeem, M., Ahmad, M. Z., Umar, M., & Abbas, Z. U. (2023). Ion Exchange Resins and their Applications in Water Treatment and Pollutants Removal from Environment: A Review: Ion Exchange Resins and their Applications. *Futuristic Biotechnology*, 12-19.

Ali, A. H. (2022). An Efficient photocatalyst based on Polyaniline Decorated MWCNT/CeO_2 for degradation of Methylene Blue (MB) Dye. *RSC advances* *171*(6), 77509.

Ali, H. M., Ibrahim, S. M., Zeid, E. F. A., Al-Hossainy, A. F., & Abd El-Aal, M. (2022). A comparative study of Cu-anchored 0D and 1D ZnO nanostructures for the reduction of organic pollutants in water. *RSC advances*, *12*(26), 16496-16509.

Ali, I., Suhail, M., Alothman, Z. A., & Alwarthan, A. (2018). Recent advances in syntheses, properties and applications of TiO_2 nanostructures. *RSC advances*, *8*(53), 30125-30147.

Ali, R. A. M., & Nayan, N. (2010). Fabrication and analysis of dye-sensitized solar cell using natural dye extracted from dragon fruit. *International Journal of Integrated Engineering*, *2*(3).

Ali, S., Ismail, P. M., Khan, M., Dang, A., Ali, S., Zada, A.,…Ateeq, M. (2024). Charge transfer in TiO 2-based photocatalysis: fundamental mechanisms to material strategies. *Nanoscale*.

Ali, S., Khan, M. R., Irfanullah, Sajid, M., & Zahra, Z. (2018). Phytochemical investigation and antimicrobial appraisal of Parrotiopsis jacquemontiana (Decne) Rehder. *BMC complementary and alternative medicine*, *18*, 1-15.

Alp, E., & Borazan, İ. (2023). The production of highly efficient visible-light-driven electrospun α-Fe2O3 photocatalyst through modifying iron source material for wastewater treatment applications. *Journal of the Chinese Chemical Society*, *70*(7), 1510-1520.

Álvarez-Chimal, R., & Arenas-Alatorre, J. Á. (2023). Green synthesis of nanoparticles. *A biological approach*, *2*, 100178.

Aly, A. A., Ali, H. G., & Eliwa, N. E. (2019). Phytochemical screening, anthocyanins and antimicrobial activities in some berries fruits. *Journal of Food Measurement and Characterization*, *13*, 911-920.

Anand, A. M., Raj, A., Salam, J. A., Adithya Nath, R., & Jayakrishnan, R. (2024). Photoconductivity in self-assembled CuO thin films. *Materials for Renewable and Sustainable Energy*, *13*(1), 45-58.

Anigol, L. B., Charantimath, J. S., & Gurubasavaraj, P. M. (2017). Effect of concentration and pH on the size of silver nanoparticles synthesized by green chemistry. *Org. Med. Chem. Int. J*, *3*(5), 1-5.

Annu, A. A., & Ahmed, S. (2018). Green synthesis of metal, metal oxide nanoparticles, and their various applications. *Handbook of Ecomaterials*, *2018*, 1-45.

Antony, R. P., Dasgupta, A., Mahana, S., Topwal, D., Mathews, T., & Dhara, S. (2015). Resonance Raman spectroscopic study for radial vibrational modes in ultra-thin walled TiO2 nanotubes. *Journal of Raman Spectroscopy*, *46*(2), 231-235.

Araújo, E. S., Pereira, M. F., da Silva, G. M., Tavares, G. F., Oliveira, C. Y., & Faia, P. M. (2023). A Review on the Use of Metal Oxide-Based Nanocomposites for the Remediation of Organics-Contaminated Water via Photocatalysis: Fundamentals, Bibliometric Study and Recent Advances. *Toxics*, *11*(8), 658.

Aravind, M., Amalanathan, M., & Mary, M. S. M. (2021). Synthesis of TiO_2 nanoparticles by chemical and green synthesis methods and their multifaceted properties. *SN Applied Sciences*, *3*, 1-10.

Ardeshirfard, H., & Elhamifar, D. (2023). Magnetic cobalt oxide supported organosilica-sulfonic acid as a powerful nanocatalyst for the synthesis of tetrahydrobenzo [a] xanthen-11-ones. *Scientific Reports*, *13*(1), 14134.

Arof, A. K., & Ping, T. L. (2017). *Chlorophyll as Photosensitizer in Dye-Sensitized Solar Cells*. InTech: Rijeka.

Arulraj, A., Senguttuvan, G., Veeramani, S., Sivakumar, V., & Subramanian, B. (2019). Photovoltaic performance of natural metal free photo-sensitizer for TiO_2 based dye-sensitized solar cells. *Optik*, *181*, 619-626.

Arun, J., Nachiappan, S., Rangarajan, G., Alagappan, R. P., Gopinath, K., & Lichtfouse, E. (2023). Synthesis and application of titanium dioxide photocatalysis for energy, decontamination and viral disinfection: A review. *Environmental Chemistry Letters*, *21*(1), 339-362.

Ashenafi, E. L., Nyman, M. C., Shelley, J. T., & Mattson, N. S. (2023). Spectral properties and stability of selected carotenoid and chlorophyll compounds in different solvent systems. *Food Chemistry Advances*, *2*, 100178.

Ashok, A., Beula, R. J., Magesh, R., Unnikrishnan, G., Paul, P. M., Bennett, H. C.,…Abiram, A. (2024). Bandgap engineering of CuO/TiO_2 nanocomposites and their synergistic effect on the performance of dye-sensitized solar cells. *Optical Materials*, *148*, 114896.

Aslam, A., Mehmood, U., Arshad, M. H., Ishfaq, A., Zaheer, J., Khan, A. U. H., & Sufyan, M. (2020). Dye-sensitized solar cells (DSSCs) as a potential photovoltaic technology for the self-powered internet of things (IoTs) applications. *Solar Energy*, *207*, 874-892.

Atiek, E., Matebu, A., Tsegaye, D., Behailu, G., & Abebe, B. (2024). Green synthesis of TiO2/ZnO heterostructure using Urtica Smensis leaf extract for antibacterial activity. *Results in Chemistry*, *13*(2), 281.

Atış, H. E., Turan, K., & Tığ, G. A. (2024). Development of a Cu@ ERGO-p (L-Lys) Modified GCE Electrochemical Sensor for the Simultaneous Detection of Ascorbic Acid, Dopamine, and Uric Acid. *Journal of The Electrochemical Society*, *171*(7), 077503.

Ayub, M., & Othman, M. H. D. (2023). Graphene oxide-based nanofiltration membranes for separation of heavy metals. In *Emerging Techniques for Treatment of Toxic Metals from Wastewater* (pp. 231-288). Elsevier.

Azeez, F., Al-Hetlani, E., Arafa, M., Abdelmonem, Y., Nazeer, A. A., Amin, M. O., & Madkour, M. (2018). The effect of surface charge on photocatalytic degradation of methylene blue dye using chargeable titania nanoparticles. *Scientific reports*, *8*(1), 7104.

Azmi, N., & Fatmiyah, S. (2021). Synthesis of TiO2-based photoelectrode and natural dye for dye sensitized solar cell (DSSC). Journal of Physics: Conference Series,

Bakry, A. M., Alamier, W. M., El-Shall, M. S., & Awad, F. S. (2022). Facile synthesis of amorphous zirconium phosphate graphitic carbon nitride composite and its high performance for photocatalytic degradation of indigo carmine dye in water. *Journal of Materials Research and Technology*, *20*, 1456-1469.

Balachandran, K., Kalaivani, T., Thangaraju, D., Mageswari, S., Senan, M. V., & Preethi, A. (2021). Fabrication of photoanodes using sol-gel synthesized Ag-doped TiO2 for enhanced DSSC efficiency. *Materials Today: Proceedings*, *37*, 515-521.

Baral, S. C., Maneesha, P., Datta, S., Dukiya, K., Sasmal, D., Samantaray, K. S., & Sen, S. (2024). Enhanced photocatalytic degradation of organic pollutants in water using

copper oxide (CuO) nanosheets for environmental application. *JCIS Open*, *13*, 100102.

Bashir, S., Awan, M. S., Farrukh, M. A., Naidu, R., Khan, S. A., Rafique, N.,…Khan, M. Z. (2022). In-vivo (Albino Mice) and in-vitro assimilation and toxicity of zinc oxide nanoparticles in food materials. *International Journal of Nanomedicine*, *17*, 4073.

Basit, R. A., Abbasi, Z., Hafeez, M., Ahmad, P., Khan, J., Khandaker, M. U.,…Khalid, A. (2023). Successive photocatalytic degradation of methylene blue by ZnO, CuO and ZnO/CuO synthesized from coriandrum sativum plant extract via green synthesis technique. *Crystals*, *13*(2), 281.

Bassim, S., Mageed, A. K., AbdulRazak, A. A., & Al-Sheikh, F. (2023). Photodegradation of methylene blue with aid of green synthesis of CuO/TiO2 nanoparticles from extract of citrus aurantium juice. *Bulletin of Chemical Reaction Engineering & Catalysis*, *18*(1), 1-16.

Baudys, M., Berthet, E., Macak, J. M., Lhotka, M., & Krýsa, J. (2023). Photocatalytic degradation of gaseous pollutants on nanostructured TiO2 films of various thickness and surface area. *Photochemical & Photobiological Sciences*, 1-10.

Behera, M., Alqahtani, F. O., Chakrabortty, S., Nayak, J., Banerjee, S., Kumar, R., & Tripathy, S. K. (2023). CuO/TiO_2/ZnO NPs Anchored Hydrogen Exfoliated Graphene: To Comprehend the Role of Graphene in Catalytic Reduction of p-Nitrophenol. *ACS omega*, *8*(45), 42164-42176.

Bekele, E. T., Zereffa, E. A., Gultom, N. S., Kuo, D.-H., Gonfa, B. A., & Sabir, F. K. (2021). Biotemplated synthesis of titanium oxide nanoparticles in the presence of root extract of Kniphofia schemperi and its application for dye sensitized solar cells. *International Journal of Photoenergy*, *2021*.

Bera, S., Sengupta, D., Roy, S., & Mukherjee, K. (2021). Research on dye sensitized solar cell: A review highlighting the progress in India. *Journal of Physics: Energy*.

Bharti, B., Kumar, S., Lee, H.-N., & Kumar, R. (2016). Formation of oxygen vacancies and Ti^{3+} state in TiO_2 thin film and enhanced optical properties by air plasma treatment. *Scientific reports*, *6*(1), 32355.

Bhattacharya, S., & Datta, J. (2020). Wide-low energy coupled semi-conductor layers of TiO2 – CdX boosting the performance of DSSC. *Solar Energy*, *208*, 674-687. https://doi.org/10.1016/j.solener.2020.08.024

Bisht, S., Ghalwan, M., Oza, A. D., Saxena, K. K., & Prakash, C. (2023). Green synthesis of CuO/TiO2 nanocomposite based photo catalyst and its applications in treatment of waste water. *International Journal on Interactive Design and Manufacturing (IJIDeM)*, 1-6.

Bisrat, D., Begna, T., Ulziibayar, D., & Jung, C. (2022). Acaricidal activity of essential oil-derived components from Thymus schimperi Ronninger against Varroa destructor Anderson and Trueman. *Journal of Apicultural Research*, 1-7.

Bonkerud, J., Zimmermann, C., Weiser, P. M., Vines, L., & Monakhov, E. V. (2021). On the dielectric constant of titanium dioxide.

Bopape, D. A., Mathobela, S., Matinise, N., Motaung, D. E., & Hintsho-Mbita, N. C. (2023). Green synthesis of CuO-TiO_2 nanoparticles for the degradation of organic pollutants: physical, optical and electrochemical properties. *Catalysts*, *13*(1), 163.

Boruban, C., & Esenturk, E. N. (2018). Activated carbon-supported CuO nanoparticles: a hybrid material for carbon dioxide adsorption. *Journal of Nanoparticle Research*, *20*, 1-9.

Boukoussa, B., Hakiki, A., Moulai, S., Chikh, K., Kherroub, D. E., Bouhadjar, L., & Hamacha, R. (2018). Adsorption behaviors of cationic and anionic dyes from aqueous solution on nanocomposite polypyrrole/SBA-15. *Journal of materials science*, *53*(10), 7372-7386.

Bykkam, S., Prasad, D., Maurya, M., Sadasivuni, K., & Cabibihan, J. (2021). Comparison Study of Metal Oxides (CeO_2, CuO, SnO_2, CdO, ZnO and TiO_2) Decked Few Layered Graphene Nanocomposites for Dye-Sensitized Solar Cells. Sustainability 2021, 13, 7685.

Carella, A., Borbone, F., & Centore, R. (2018). Research progress on photosensitizers for DSSC. *Front Chem*, *6*, 481.

Celik, E., Gokcen, Z., Azem, N. A., Tanoglu, M., & Emrullahoglu, O. (2006). Processing, characterization and photocatalytic properties of Cu doped TiO2 thin films on glass substrate by sol–gel technique. *Materials Science and Engineering: B*, *132*(3), 258-265.

Chatterjee, S. (2018). Performance of Dye-Sensitized Solar Cells (DSSCs) Fabricated with Zinc Oxide (ZnO) Nanpowders and Nanorods. *Journal of Materials Engineering and Performance*, *27*(6), 2713-2718.

Chaudhari, S. M., Gawal, P. M., Sane, P. K., Sontakke, S. M., & Nemade, P. R. (2018). Solar light-assisted photocatalytic degradation of methylene blue with Mo/TiO_2: A comparison with Cr-and Ni-doped TiO_2. *Research on Chemical Intermediates*, *44*, 3115-3134.

Chazaux, M., Schiphorst, C., Lazzari, G., & Caffarri, S. (2022). Precise estimation of chlorophyll a, b and carotenoid content by deconvolution of the absorption spectrum and new simultaneous equations for Chl determination. *The Plant Journal*, *109*(6), 1630-1648.

Cheng, F., Ou, Y., Liu, G., Zhao, L., Dong, B., Wang, S., & Wen, S. (2019). Novel Quasi-Solid-State Electrolytes based on Electrospun Poly(vinylidene fluoride) Fiber Membranes for Highly Efficient and Stable Dye-Sensitized Solar Cells. *Nanomaterials*, *9*(5), 783. https://doi.org/10.3390/nano9050783

Chi, N., & Wang, Y. (2022). Synthesis and application of CuO-TiO_2 hybrid nanostructures as Photocatalytst for degradation of p-nitrophenol in wastewater. *INTERNATIONAL JOURNAL OF ELECTROCHEMICAL SCIENCE*, *17*(10).

Chougala, L., Yatnatti, M., Linganagoudar, R., Kamble, R., & Kadadevarmath, J. (2017). A simple approach on synthesis of TiO_2 nanoparticles and its application in dye sensitized solar cells.

Colombo, A., Dragonetti, C., Fagnani, F., Roberto, D., Melchiorre, F., & Biagini, P. (2019). Improving the efficiency of copper-dye-sensitized solar cells by manipulating the electrolyte solution. *Dalton Transactions*, *48*(26), 9818-9823.

Conradie, J. (2024). Effective dyes for DSSCs–important experimental and calculated parameters. *Energy Nexus*, 100282.

Dahanayake, J. M., Perera, P. K., Galappatty, P., Perera, H. D. S. M., & Arawwawala, L. D. A. M. (2019). Comparative phytochemical analysis and antioxidant activities of Tamalakyadi decoction with its modified dosage forms. *Evidence-Based Complementary and Alternative Medicine*, *2019*(1), 6037137.

Das, R., Ambardekar, V., & Bandyopadhyay, P. P. (2021). Titanium dioxide and its applications in mechanical, electrical, optical, and biomedical fields. *Titanium Dioxide-Advances and Applications*.

Datta, S., Dey, A., Singha, N. R., & Roy, S. (2020). Enhanced performance of dye-sensitized solar cell with thermally stable natural dye-assisted TiO_2/MnO_2 bilayer-assembled photoanode. *Materials for Renewable and Sustainable Energy*, *9*(4), 1-11.

Debnath, D., Sen, D., Neog, T. T., Saha, B., & Ghosh, S. K. (2024). Growth of ZnO polytypes: Multiple facets of diverse applications. *Crystal Growth & Design*, *24*(3), 871-885.

Desta, K. T., Kim, G. S., Abd El-Aty, A., Raha, S., Kim, M.-B., Jeong, J. H., & Shim, J.-H. (2017). Flavone polyphenols dominate in Thymus schimperi Ronniger: LC–ESI–MS/MS characterization and study of anti-proliferative effects of plant extract on AGS and HepG2 cancer cells. *Journal of Chromatography B*, *1053*, 1-8.

Devia, P., & Singh, J. (2020). Role of Oxygen Vacancies in In_2O_3 Nanostructures towards Enhancement of Photocatalytic Activity. 2020 5th IEEE International Conference on Emerging Electronics (ICEE),

Dey, A., Chandrabose, G., Ghosh, P., Damptey, L. A., Clark, A. H., Selvaraj, V., & Dalapati, G. K. (2021). Atmospheric pressure plasma engineered superhydrophilic CuO surfaces with enhanced catalytic activities. *Applied surface science*, *564*, 150413.

Diantoro, M., Maftuha, D., Suprayogi, T., Iqbal, M. R., Mufti, N., Taufiq, A., & Hidayat, R. (2019). Performance of pterocarpus indicus willd leaf extract as natural dye TiO_2-Dye/ITO DSSC. *Materials Today: Proceedings*, *17*, 1268-1276.

Dias, M. C., Pinto, D. C., & Silva, A. M. (2021). Plant flavonoids: Chemical characteristics and biological activity. *Molecules*, *26*(17), 5377.

Duan, Y., Tang, Q., Chen, Y., Zhao, Z., Lv, Y., Hou, M.,…Yu, L. (2015). Solid-state dye-sensitized solar cells from poly (ethylene oxide)/polyaniline electrolytes with catalytic and hole-transporting characteristics. *Journal of Materials Chemistry A*, *3*(10), 5368-5374.

Dubale, S., Kebebe, D., Zeynudin, A., Abdissa, N., & Suleman, S. (2023). Phytochemical screening and antimicrobial activity evaluation of selected medicinal plants in Ethiopia. *Journal of Experimental Pharmacology*, 51-62.

Dudek, B., Warskulat, A.-C., & Schneider, B. (2016). The occurrence of flavonoids and related compounds in flower sections of Papaver nudicaule. *Plants*, *5*(2), 28.

Dulta, K., Koşarsoy Ağçeli, G., Chauhan, P., Jasrotia, R., Chauhan, P., & Ighalo, J. O. (2022). Multifunctional CuO nanoparticles with enhanced photocatalytic dye degradation and antibacterial activity. *Sustainable Environment Research*, *32*, 1-15.

Dutta, A., Nayak, M., Nag, R., Bera, A., Bhaumik, S., Akhtar, A. J., & Saha, S. K. (2024). Precipitation-assisted, low-temperature-annealed TiO2 and its nanocomposites-based photoanode for DSSCs. *Journal of Materials Science: Materials in Electronics*, *35*(4), 292.

Ealia, S. A. M., & Saravanakumar, M. (2017). A review on the classification, characterisation, synthesis of nanoparticles and their application. *IOP Conference Series: Materials Science and Engineering*,

El-Agez, T. M., Taya, S. A., Elrefi, K. S., & Abdel-Latif, M. S. (2014). Dye-sensitized solar cells using some organic dyes as photosensitizers. *Optica applicata*, *44*(2), 345-351.

El-Awady, M., Elmansi, H., Belal, F., & Shabana, R. A. (2022). Insights on the quantitative concurrent fluorescence-based analysis of anti-COVID-19 drugs remdesivir and favipiravir. *Journal of fluorescence*, *32*(5), 1941-1948.

El-Deen, S., Hashem, A., Abdel Ghany, A., Indris, S., Ehrenberg, H., Mauger, A., & Julien, C. (2018). Anatase TiO_2 nanoparticles for lithium-ion batteries. *Ionics*, *24*, 2925-2934.

El-Ghamri, H. S., El-Agez, T. M., Taya, S. A., Abdel-Latif, M. S., & Batniji, A. Y. (2014). Dye-sensitized solar cells with natural dyes extracted from plant seeds. *Materials Science-Poland*, *32*(4), 547-554.

El-Ghamri, H. S., Taya, S. A., El-Agez, T. M., Al-Kahlout, A. M., Al Dahoudi, N., & Abdel-Latif, M. S. (2015). Natural dyes as photosensitizers for dye-sensitized solar cells.

El Shafey, A. M. (2020). Green synthesis of metal and metal oxide nanoparticles from plant leaf extracts and their applications: A review. *Green Processing and Synthesis*, *9*(1), 304-339.

Etape, E. P., Ngolui, L. J., Foba-Tendo, J., Yufanyi, D. M., & Namondo, B. V. (2017). Synthesis and characterization of CuO, TiO2, and CuO-TiO_2 mixed oxide by a modified oxalate route. *J. Appl. Chem*, *2017*, 1-10.

Fan, Y.-H., Ho, C.-Y., & Chang, Y.-J. (2017). Enhancement of dye-sensitized solar cells efficiency using mixed-phase TiO2 nanoparticles as photoanode. *Scanning*, *2017*.

Farooq, U., Ahmed, J., Alshehri, S. M., & Ahmad, T. (2019). High-surface-area sodium tantalate nanoparticles with enhanced photocatalytic and electrical properties prepared through polymeric citrate precursor route. *ACS omega*, *4*(21), 19408-19419.

Fito, J., Abewaa, M., Mengistu, A., Angassa, K., Ambaye, A. D., Moyo, W., & Nkambule, T. (2023). Adsorption of methylene blue from textile industrial wastewater using activated carbon developed from Rumex abyssinicus plant. *Scientific Reports*, *13*(1), 5427.

García-Salinas, M. J., & Ariza, M. J. (2019). Optimizing a simple natural dye production method for dye-sensitized solar cells: Examples for betalain (bougainvillea and beetroot extracts) and anthocyanin dyes. *Applied Sciences*, *9*(12), 2515.

George, G., Yendaluru, R. S., & Mary Ealias, A. (2020). Fabrication of Dye-Sensitized Solar Cells using natural flower dye extracts: A study on performance analysis and solar dye degradation. *Energy Sources, Part A: Recovery, Utilization, and Environmental Effects*, 1-15.

Ghann, W., Kang, H., Sheikh, T., Yadav, S., Chavez-Gil, T., Nesbitt, F., & Uddin, J. (2017). Fabrication, Optimization and Characterization of Natural Dye Sensitized Solar Cell. *Sci Rep*, *7*, 41470.

Gnanasangeetha, D., & Suresh, M. (2020). A Review on Green Synthesis of Metal and Metal Oxide Nanoparticles. *Nature Environment and Pollution Technology*, *19*(5), 1789-1800.

Gnanasekar, S., Kollu, P., Jeong, S. K., & Grace, A. N. (2019). Pt-free, low-cost and efficient counter electrode with carbon wrapped VO_2 (M) nanofiber for dye-sensitized solar cells. *Sci Rep*, *9*(1), 1-12.

Gnida, P., Jarka, P., Chulkin, P., Drygała, A., Libera, M., Tański, T., & Schab-Balcerzak, E. (2021). Impact of TiO2 Nanostructures on Dye-Sensitized Solar Cells Performance. *Materials (Basel)*, *14*(7), 1633.

Godibo, D. J., Anshebo, S. T., & Anshebo, T. Y. (2015). Dye sensitized solar cells using natural pigments from five plants and quasi-solid state electrolyte. *Journal of the Brazilian Chemical Society*, *26*, 92-101.

Gonfa, Y. H., Beshah, F., Tadesse, M. G., Bachheti, A., & Bachheti, R. K. (2021). Phytochemical investigation and potential pharmacologically active compounds of Rumex nepalensis: an appraisal. *Beni-Suef University Journal of Basic and Applied Sciences*, *10*, 1-11.

Gong, J., Sumathy, K., Qiao, Q., & Zhou, Z. (2017). Review on dye-sensitized solar cells (DSSCs): Advanced techniques and research trends. *Renewable and Sustainable Energy Reviews*, *68*, 234-246.

Gouasmia, A., Zouaoui, E., Mekkaoui, A. A., Haddad, A., & Bousba, D. (2022). Highly efficient photocatalytic degradation of malachite green dye over copper oxide and copper cobaltite photocatalysts under solar or microwave irradiation. *Inorganic Chemistry Communications*, *145*, 110066.

Guo, X., Wang, X., & Niu, Y. (2023). Visible Light Driven Photocatalytic Degradation of Norfloxacin Using 3D Supramolecular Compounds. *Journal of Cluster Science*, 1-10.

Haleem, A., Javaid, M., Singh, R. P., Rab, S., & Suman, R. (2023). Applications of Nanotechnology in Medical field. *Global Health Journal*.

Hassaan, M. A., El-Nemr, M. A., Elkatory, M. R., Ragab, S., Niculescu, V.-C., & El Nemr, A. (2023). Principles of photocatalysts and their different applications: a review. *Topics in Current Chemistry*, *381*(6), 31.

Hatamvand, M., Kamrani, E., Lira-Cantu, M., Madsen, M., Patil, B. R., Vivo, P.,…Zhan, Y. (2020). Recent advances in fiber-shaped and planar-shaped textile solar cells. *Nano Energy*, *71*, 104609.

Hidayat, A., Taufiq, A., Supardi, Z., Jayadininggar, S., Sa'adah, U., Astarini, N., & Diantoro, M. (2021). Synthesis and characterization of TiO2/ZnO-Ag@ TiO2 nanocomposite and their performance as photoanode of organic Dye-Sensitized Solar Cell. *Materials Today: Proceedings*.

Hosseini, H., Zirakjou, A., McClements, D. J., Goodarzi, V., & Chen, W.-H. (2022). Removal of methylene blue from wastewater using ternary nanocomposite aerogel systems: Carboxymethyl cellulose grafted by polyacrylic acid and decorated with graphene oxide. *Journal of Hazardous Materials*, *421*, 126752.

Hu, M., Yao, Z., & Wang, X. (2017). Characterization techniques for graphene-based materials in catalysis. *AIMS Materials Science*, *4*(3), 755-788.

Isah, K., Sadik, A., & Jolayemi, B. (2017). Effect of Natural Dye Co-Sensitization on the Performance of Dye-Sensitized Solar Cells (DSSCS) Based on Anthocyanin and Betalain Pigments Sensitisation. *European Journal of Applied Sciences*, *9*(3), 140-146.

Ito, S., Murakami, T. N., Comte, P., Liska, P., Grätzel, C., Nazeeruddin, M. K., & Grätzel, M. (2008). Fabrication of thin film dye sensitized solar cells with solar to electric power conversion efficiency over 10%. *Thin solid films*, *516*(14), 4613-4619.

Jayachithra, J., Elampari, K., & Meena, M. (2022). Fabrication of TiO2 based Dye-Sensitized Solar Cell using Nerium oleander as a sensitizer. IOP Conference Series: Materials Science and Engineering,

Jayswal, S., & Moirangthem, R. S. (2018). Thermal decomposition route to synthesize ZnO nanoparticles for photocatalytic application. AIP Conference Proceedings,

Kakiage, K., Aoyama, Y., Yano, T., Oya, K., Fujisawa, J.-i., & Hanaya, M. (2015). Highly-efficient dye-sensitized solar cells with collaborative sensitization by silyl-anchor and carboxy-anchor dyes. *Chemical communications*, *51*(88), 15894-15897.

Kalanur, S. S., Yoo, I.-H., Park, J., & Seo, H. (2017). Insights into the electronic bands of WO 3/BiVO 4/TiO 2, revealing high solar water splitting efficiency. *Journal of Materials Chemistry A*, *5*(4), 1455-1461.

Kalaycıoğlu, Z., Özuğur Uysal, B., Pekcan, O. n., & Erim, F. B. (2023). Efficient photocatalytic degradation of methylene blue dye from aqueous solution with cerium oxide nanoparticles and graphene oxide-doped polyacrylamide. *ACS omega*, *8*(14), 13004-13015.

Kamble, G. S., Natarajan, T. S., Patil, S. S., Thomas, M., Chougale, R. K., Sanadi, P. D.,…Ling, Y.-C. (2023). BiVO4 as a sustainable and emerging photocatalyst: Synthesis methodologies, engineering properties, and its volatile organic compounds degradation efficiency. *Nanomaterials*, *13*(9), 1528.

Kang, S., Zhao, Y., Wang, W., Zhang, T., Chen, T., Yi, H., & Song, S. (2018). Removal of methylene blue from water with montmorillonite nanosheets/chitosan hydrogels as adsorbent. *Applied surface science*, *448*, 203-211.

Kannan, K., Radhika, D., Gnanasangeetha, D., Lakkaboyana, S. K., Sadasivuni, K. K., Gurushankar, K., & Hanafiah, M. M. (2021). Photocatalytic and antimicrobial properties of microwave synthesized mixed metal oxide nanocomposite. *Inorganic Chemistry Communications*, *125*, 108429.

Kapoor, A., & Rajput, J. K. (2022). Solar light photocatalytic activity of CuO/TiO2 mixed oxide derived from conjugated azomethine metal complex for degradation of food colorants. *Journal of Molecular Liquids, 366*, 120280.

Karim, N. A., Mehmood, U., Zahid, H. F., & Asif, T. (2019). Nanostructured photoanode and counter electrode materials for efficient Dye-Sensitized Solar Cells (DSSCs). *Solar Energy, 185*, 165-188.

Kermani, M., Mostafapour, A., Sabouri, Z., Gheibihayat, S. M., & Darroudi, M. (2023). The photocatalytic, cytotoxicity, and antibacterial properties of zinc oxide nanoparticles synthesized using Trigonella foenum-graecum L extract. *Environmental Science and Pollution Research, 30*(7), 19313-19325.

Khan, I., Saeed, K., Zekker, I., Zhang, B., Hendi, A. H., Ahmad, A.,…Shah, L. A. (2022). Review on methylene blue: Its properties, uses, toxicity and photodegradation. *Water, 14*(2), 242.

Khan, M., Al-Mamun, M., Al-Amin, M., Moniruzzaman, M., & Hasan, M. (2017). Dye-sensitized solar cell using used semiconductor glass and natural dye: towards alternative energy challenge. *International Journal of Renewable Energy Resources*, *5*(2), 38-44.

Khan, M., Al-Mamun, M., Halder, P., & Aziz, M. (2017). Performance improvement of modified dye-sensitized solar cells. *Renewable and Sustainable Energy Reviews*, *71*, 602-617.

Khoroshko, L., Borisenko, V., Baltrukovich, P., Nurmonov, S., & Ruzimuradov, O. (2023). One-step sol-gel fabrication of TiO2/(CuO+ Cu2O) photocatalysts. *Journal of Sol-Gel Science and Technology*, *108*(2), 320-324.

Kibria, M. T., Ahammed, A., Sony, S. M., Hossain, F., & Islam, S. (2014). A Review: Comparative studies on different generation solar cells technology. Proc. of 5th International Conference on Environmental Aspects of Bangladesh,

Konstantinova, E., Kushnikov, M., Zaitsev, V., Kytin, V., Marikutsa, A., Trusov, G.,…Kashkarov, P. (2019). High photocatalytic activity nanomaterials based on titanium dioxide. *Nanotechnologies in Russia*, *14*, 190-196.

Krawczak, E. (2019). Dye photosensitizers and their influence on DSSC efficiency: a review. *Informatyka, Automatyka, Pomiary w Gospodarce i Ochronie Środowiska*, *9*.

Kubiak, A., Bielan, Z., Kubacka, M., Gabała, E., Zgoła-Grześkowiak, A., Janczarek, M.,…Jesionowski, T. (2020). Microwave-assisted synthesis of a TiO2-CuO heterojunction with enhanced photocatalytic activity against tetracycline. *Applied Surface Science, 520,* 146344.

Kubiak, A., Siwińska-Ciesielczyk, K., Goscianska, J., Dobrowolska, A., Gabała, E., Czaczyk, K., & Jesionowski, T. (2019). Hydrothermal-assisted synthesis of highly crystalline titania–copper oxide binary systems with enhanced antibacterial properties. *Materials Science and Engineering: C, 104,* 109839.

Kučerík, J., Tokarski, D., Demyan, M. S., Merbach, I., & Siewert, C. (2018). Linking soil organic matter thermal stability with contents of clay, bound water, organic carbon and nitrogen. *Geoderma*, *316*, 38-46.

Kuei, B., Aplan, M. P., Litofsky, J. H., & Gomez, E. D. (2020). New opportunities in transmission electron microscopy of polymers. *Materials Science and Engineering: R: Reports*, *139*, 100516.

Kumar, D. K., Kříž, J., Bennett, N., Chen, B., Upadhayaya, H., Reddy, K. R., & Sadhu, V. (2020). Functionalized metal oxide nanoparticles for efficient dye-sensitized solar cells (DSSCs): A review. *Materials Science for Energy Technologies*, *3*, 472-481.

Kumar, M., Bhatt, V., Nayal, O. S., Sharma, S., Kumar, V., Thakur, M. S.,…Sharma, U. (2017). CuI nanoparticles as recyclable heterogeneous catalysts for C–N bond formation reactions. *Catalysis Science & Technology*, *7*(13), 2857-2864.

Kumar, R., Sahajwalla, V., & Bhargava, P. (2019). Fabrication of a counter electrode for dye-sensitized solar cells (DSSCs) using a carbon material produced with the organic ligand 2-methyl-8-hydroxyquinolinol (Mq). *nanoscale advances*, *1*(8), 3192-3199.

Kumar, S., Asokan, K., Singh, R. K., Chatterjee, S., Kanjilal, D., & Ghosh, A. K. (2014). Investigations on structural and optical properties of ZnO and ZnO: Co

nanoparticles under dense electronic excitations. *RSC Advances*, *4*(107), 62123-62131.

Kumar, T. N., Yuvaraj, S., Kavitha, P., Sudhakar, V., Krishnamoorthy, K., & Neppolian, B. (2020). Aromatic amine passivated TiO2 for dye-sensitized solar cells (DSSC) with~ 9.8% efficiency. *Solar Energy*, *201*, 965-971.

Kumara, N., Ekanayake, P., Lim, A., Liew, L. Y. C., Iskandar, M., Ming, L. C., & Senadeera, G. (2013). Layered co-sensitization for enhancement of conversion efficiency of natural dye sensitized solar cells. *Journal of alloys and compounds*, *581*, 186-191.

Kumara, N., Lim, A., Lim, C. M., Petra, M. I., & Ekanayake, P. (2017). Recent progress and utilization of natural pigments in dye sensitized solar cells: A review. *Renewable and Sustainable Energy Reviews*, *78*, 301-317.

Kumari, H., Sonia, Suman, Ranga, R., Chahal, S., Devi, S.,…Kumar, S. (2023). A Review on Photocatalysis Used For Wastewater Treatment: Dye Degradation. *Water, Air, & Soil Pollution*, *234*(6), 349.

Kundu, A., & Mondal, A. (2019). Photodegradation of methylene blue under direct sunbeams by synthesized anatase titania nanoparticles. *SN Applied Sciences*, *1*, 1-17.

Kusmierek, E. (2020). A CeO_2 semiconductor as a photocatalytic and photoelectrocatalytic material for the remediation of pollutants in industrial wastewater: a review. *Catalysts*, *10*(12), 1435.

Lal, M., Chhabra, V., Ayyub, P., & Maitra, A. (1998). Preparation and characterization of ultrafine TiO_2 particles in reverse micelles by hydrolysis of titanium di-ethylhexyl sulfosuccinate. *Journal of materials research*, *13*(5), 1249-1254.

Lan, L., Gnappi, G., & Montenero, A. (1993). Infrared study of EPOXS-TEOS-TPOT gels. *Journal of materials science*, *28*, 2119-2123.

Lee, C.-P., Chu, T.-C., Chang, L.-Y., Lin, J.-J., & Ho, K.-C. (2013). Solid-state ionic liquid based electrolytes for dye-sensitized solar cells. In *Ionic Liquids-New Aspects for the Future*. IntechOpen.

Li, D., Qin, D., Deng, M., Luo, Y., & Meng, Q. (2009). Optimization the solid-state electrolytes for dye-sensitized solar cells. *Energy & Environmental Science*, *2*(3), 283-291.

Li, J., Lu, L., Jiang, Y., Tang, F., Wu, Q., Liu, H., & Zeng, Q. (2024). Evaluation of antibacterial activity and influencing factors of normal and nanostructured copper-based materials. *Heliyon*, *10*(6).

Li, L., Chen, X., Quan, X., Qiu, F., & Zhang, X. (2023). Synthesis of CuO x/TiO_2 photocatalysts with enhanced photocatalytic performance. *ACS omega*, *8*(2), 2723-2732.

Liao, D., Zhi, J., Wang, Q., Yan, W., Guo, Y., Han, Y., & Liang, W. (2023). Efficient photoelectrochemical aptasensing of di-2-ethylhexyl phthalate in environmental samples based on N, S co-doped graphene quantum dots/TiO_2 nanorods. *Analytica Chimica Acta*, 341477.

Liga, S., Paul, C., & Péter, F. (2023). Flavonoids: Overview of biosynthesis, biological activity, and current extraction techniques. *Plants*, *12*(14), 2732.

Liu, B., Luo, H., Rong, H., Zeng, X., Wu, K., Chen, Z.,…Xu, D. (2019). Temperature-induced adsorption and desorption of phosphate on poly (acrylic acid-co-N-[3-(dimethylamino) propyl] acrylamide) hydrogels in aqueous solutions. *Desalination and Water Treatment*, *160*, 260-267.

Liu, Z., Yu, X., Wang, K., Yu, H., Wang, T., Zhao, N., & Zhang, J. (2023). Preparation of WO_3 Particles and Their Photocatalytic Properties. Journal of Physics: Conference Series,

Lu, D., Zelekew, O. A., Abay, A. K., Huang, Q., Chen, X., & Zheng, Y. (2019). Synthesis and photocatalytic activities of a CuO/TiO 2 composite catalyst using aquatic plants with accumulated copper as a template. *RSC advances*, *9*(4), 2018-2025.

Ludin, N. A., Mahmoud, A. A.-A., Mohamad, A. B., Kadhum, A. A. H., Sopian, K., & Karim, N. S. A. (2014). Review on the development of natural dye photosensitizer for dye-sensitized solar cells. *Renewable and Sustainable Energy Reviews*, *31*, 386-396.

Luthfiah, A., Permana, M. D., Deawati, Y., Firdaus, M. L., Rahayu, I., & Eddy, D. R. (2021). Photocatalysis of nanocomposite titania–natural silica as antibacterial against Staphylococcus aureus and Pseudomonas aeruginosa. *RSC advances*, *11*(61), 38528-38536.

Mabadahanye, K., Bhembe, N. L., & Green, E. (2022). Crude extracts activity of three selected medicinal plants from the Venda region against some pathogenic organisms. *African Health Sciences, 22*(2), 717-727.

Machut, C., Kania, N., Léger, B., Wyrwalski, F., Noël, S., Addad, A.,…Ponchel, A. (2020). Fast Microwave Synthesis of Gold-Doped TiO2 Assisted by Modified Cyclodextrins for Photocatalytic Degradation of Dye and Hydrogen Production. *Catalysts*, *10*(7), 801.

Mahmoudabadi, Z. D., & Eslami, E. (2019). One-step synthesis of CuO/TiO2 nanocomposite by atmospheric microplasma electrochemistry–Its application as photoanode in dye-sensitized solar cell. *Journal of Alloys and Compounds*, *793*, 336-342.

Makuła, P., Pacia, M., & Macyk, W. (2018). How to correctly determine the band gap energy of modified semiconductor photocatalysts based on UV–Vis spectra. In (Vol. 9, pp. 6814-6817): ACS Publications.

Mansour, S. A., Farha, A., & Kotkata, M. (2019). Sol–Gel Synthesized Co-Doped Anatase TiO 2 Nanoparticles: Structural, Optical, and Magnetic Characterization. *Journal of Inorganic and Organometallic Polymers and Materials*, *29*, 1375-1382.

Masood, A., Iqbal, T., Ashraf, M., Nazir, A., Ali, F., Ranjha, Q. A.,…Galal, A. M. (2023). Synthesis and characterization of cadmium doped zinc oxide nanoparticles for visible light driven catalytic removal of MB and RhB dye: experimental and

computational analysis. *Journal of Inorganic and Organometallic Polymers and Materials*, *33*(7), 1841-1854.

Masoudian, N., Rajabi, M., & Ghaedi, M. (2019). Titanium oxide nanoparticles loaded onto activated carbon prepared from bio-waste watermelon rind for the efficient ultrasonic-assisted adsorption of congo red and phenol red dyes from wastewaters. *Polyhedron*, *173*, 114105.

Mathew, S., kumar Prasad, A., Benoy, T., Rakesh, P., Hari, M., Libish, T.,…Vallabhan, C. (2012). UV-visible photoluminescence of TiO 2 nanoparticles prepared by hydrothermal method. *Journal of fluorescence, 22*, 1563-1569.

Matouk, Z., Islam, M., Gutiérrez, M., Pireaux, J.-J., & Achour, A. (2022). X-ray Photoelectron Spectroscopy (XPS) Analysis of Ultrafine Au Nanoparticles Supported over Reactively Sputtered TiO2 Films. *Nanomaterials, 12*(20), 3692.

Matshitse, R. (2010). Brunauer-Emmett-Teller (BET) surface area analysis, Rhodes Univ. *Natl. Res. Found*.

May-Masnou, A., Soler, L., Torras, M., Salles, P., Llorca, J., & Roig, A. (2018). Fast and simple microwave synthesis of TiO2/Au nanoparticles for gas-phase photocatalytic hydrogen generation. *Frontiers in chemistry, 6*, 110.

Mehmood, U., Rahman, S.-u., Harrabi, K., Hussein, I. A., & Reddy, B. (2014). Recent advances in dye sensitized solar cells. *Advances in Materials Science and Engineering, 2014*.

Mendes, C. R., Dilarri, G., Forsan, C. F., Sapata, V. d. M. R., Lopes, P. R. M., de Moraes, P. B., & Bidoia, E. D. (2022). Antibacterial action and target mechanisms of zinc oxide nanoparticles against bacterial pathogens. *Scientific Reports, 12*(1), 2658.

Mezzomo, N., & Ferreira, S. R. (2016). Carotenoids functionality, sources, and processing by supercritical technology: a review. *Journal of Chemistry, 2016*.

Mohamed, A., & Selim, Y. (2017). Factors Affect Dye Sensitized Solar Cells performance. *Renewable Energy and Sustainable Development*, *3*(1), 83-86.

Moon, J., Shin, W., Park, J. T., & Jang, H. (2019). Solid-state solar energy conversion from WO3 nano and microstructures with charge transportation and light-scattering characteristics. *Nanomaterials (Basel)*, *9*(12), 1797.

Mortazavian, S., Saber, A., & James, D. E. (2019). Optimization of photocatalytic degradation of acid blue 113 and acid red 88 textile dyes in a UV-C/TiO_2 suspension system: application of response surface methodology (RSM). *Catalysts*, *9*(4), 360.

Mugumo, R., Ichipi, E., Tichapondwa, S. M., & Chirwa, E. M. N. (2023). Visible-Light-Induced Photocatalytic Degradation of Rhodamine B Dye Using CuS/ZnS PN Heterojunction Nanocomposite under Visible Light Irradiation.

Muniz, E. C., Góes, M. S., Silva, J. J., Varela, J. A., Joanni, E., Parra, R., & Bueno, P. R. (2011). Synthesis and characterization of mesoporous TiO2 nanostructured films prepared by a modified sol–gel method for application in dye solar cells. *Ceramics International*, *37*(3), 1017-1024.

Murthy, P. S., Venugopalan, V., Arunya, D. D., Dhara, S., Pandiyan, R., & Tyagi, A. (2011). Antibiofilm activity of nano sized CuO. International conference on nanoscience, engineering and technology (ICONSET 2011),

Muzakki, A., Shabrany, H., & Saleh, R. (2016). Synthesis of ZnO/CuO and TiO_2/CuO nanocomposites for light and ultrasound assisted degradation of a textile dye in aqueous solution. AIP Conference Proceedings,

Nabi, F., Arain, M. A., Rajput, N., Alagawany, M., Soomro, J., Umer, M.,…Liu, J. (2020). Health benefits of carotenoids and potential application in poultry industry: A review. *Journal of animal physiology and animal nutrition*, *104*(6), 1809-1818.

Najm, A. S., Alwash, S. A., Sulaiman, N. H., Chowdhury, M., & Techato, K. (2023). N719 dye as a sensitizer for dye-sensitized solar cells (DSSCs): A review of its functions and certain rudimentary principles. *Environmental Progress & Sustainable Energy*, *42*(1), e13955.

Naldoni, A., Altomare, M., Zoppellaro, G., Liu, N., Kment, S., Zboril, R., & Schmuki, P. (2018). Photocatalysis with reduced TiO2: from black TiO2 to cocatalyst-free hydrogen production. *ACS catalysis*, *9*(1), 345-364.

Nandiyanto, A. B. D., Oktiani, R., & Ragadhita, R. (2019). How to read and interpret FTIR spectroscope of organic material. *Indonesian Journal of Science and Technology*, *4*(1), 97-118.

Nassour, R., Ayash, A., & Al-Tameemi, K. (2020). Anthocyanin pigments: structure and biological importance. *J Chem Pharm Sci*, *13*(4), 45-57.

Nguyen, T. H., Nguyen, T. L., Ung, T. D. T., & Nguyen, Q. L. (2013). Synthesis and characterization of nano-CuO and CuO/TiO_2 photocatalysts. *Advances in Natural Sciences: Nanoscience and Nanotechnology*, *4*(2), 025002.

Ninnes, S., Meyer-Jacob, C., Tolu, J., Bindler, R., & Cortizas, A. M. (2024). Application of mid-infrared spectroscopy for the quantitative and qualitative analysis of organic matter in Holocene sediment records. *The Holocene*, *34*(3), 259-273.

Niu, B., Wang, X., Wu, K., He, X., & Zhang, R. (2018). Mesoporous Titanium Dioxide: Synthesis and Applications in Photocatalysis, Energy and Biology. *Materials (Basel)*, *11*(10).

Nunes, D., Fortunato, E., & Martins, R. (2022). Flexible nanostructured TiO_2-based gas and UV sensors: A review. *Discover Materials*, *2*(1), 2.

Nyamukamba, P., Okoh, O., Mungondori, H., Taziwa, R., & Zinya, S. (2018). Synthetic methods for titanium dioxide nanoparticles: a review. *Titanium Dioxide—Material for a Sustainable Environment; Yang, D., Ed*, 151-175.

Okello, A., Owuor, B. O., Namukobe, J., Okello, D., & Mwabora, J. (2021). Influence of concentration of anthocyanins on electron transport in dye sensitized solar cells. *Heliyon*, *7*(3).

Oloya, B., Namukobe, J., Ssengooba, W., Afayoa, M., & Byamukama, R. (2022). Phytochemical screening, antimycobacterial activity and acute toxicity of crude

extracts of selected medicinal plant species used locally in the treatment of tuberculosis in Uganda. *Tropical medicine and health*, *50*(1), 16.

Omar, A., Ali, M. S., & Abd Rahim, N. (2020). Electron transport properties analysis of titanium dioxide dye-sensitized solar cells (TiO_2-DSSCs) based natural dyes using electrochemical impedance spectroscopy concept: A review. *Solar Energy*, *207*, 1088-1121.

Ortiz-Quiñonez, J.-L., & Pal, U. (2024). Interface engineered metal oxide heterojunction nanostructures in photocatalytic CO_2 reduction: Progress and prospects. *Coordination Chemistry Reviews*, *516*, 215967.

Parhizkar, M., Singh, S., Nayak, P., Kumar, N., Muthe, K., Gupta, S.,…Major, S. (2005). Nanocrystalline CuO films prepared by pyrolysis of Cu-arachidate LB multilayers. *Colloids and Surfaces A: Physicochemical and Engineering Aspects*, *257*, 277-282.

Park, J., Deshmukh, P., Sohn, Y., & Shin, W. G. (2019). ZnO-TiO_2 core-shell nanowires decorated with Au nanoparticles for plasmon-enhanced photoelectrochemical water splitting. *Journal of Alloys and Compounds*, *787*, 1310-1319.

Park, Y.-S., Im, M. H., Ham, K.-S., Kang, S.-G., Park, Y.-K., Namiesnik, J., & Gorinstein, S. (2015). Quantitative assessment of the main antioxidant compounds, antioxidant activities and FTIR spectra from commonly consumed fruits, compared to standard kiwi fruit. *LWT-Food Science and Technology*, *63*(1), 346-352.

Patra, J. K., & Baek, K.-H. (2014). Green nanobiotechnology: factors affecting synthesis and characterization techniques. *Journal of Nanomaterials*, *2014*.

Pavel, M., Anastasescu, C., State, R.-N., Vasile, A., Papa, F., & Balint, I. (2023). Photocatalytic degradation of organic and inorganic pollutants to harmless end products: assessment of practical application potential for water and air cleaning. *Catalysts*, *13*(2), 380.

Pawar, M., Gaonar, M., Khajone, A., & Malasane, P. (2023). Green Synthesis of Nb_2O_5 Nanoparticles and Photodegradation of Remazol Yellow RR Dye.

Peev, G., Penchev, P., Peshev, D., & Angelov, G. (2011). Solvent extraction of rosmarinic acid from lemon balm and concentration of extracts by nanofiltration: Effect of plant pre-treatment by supercritical carbon dioxide. *Chemical Engineering Research and Design*, *89*(11), 2236-2243.

Pervaiz, T., Songtao, J., Faghihi, F., Haider, M. S., & Fang, J. (2017). Naturally occurring anthocyanin, structure, functions and biosynthetic pathway in fruit plants. *J. Plant Biochem. Physiol*, *5*(2), 1-9.

Prakash, P., Balasundaram, J., Al-Enizi, A. M., Ubaidullah, M., & Pandit, B. (2022). Effect of photovoltaic performance of plant-based cocktail DSSCs and adsorption of nano TiO2 onto the solvent-influenced dye sensitizers. *Optical Materials*, *133*, 113031.

Pramananda, V., Fityay, T. A. H., & Misran, E. (2021). Anthocyanin as natural dye in DSSC fabrication: A review. IOP Conference Series: Materials Science and Engineering,

Pratiwi, D., Nurosyid, F., Supriyanto, A., & Suryana, R. (2017). Efficiency enhancement of dye-sensitized solar cells (DSSC) by addition of synthetic dye into natural dye (anthocyanin). IOP Conference Series: Materials Science and Engineering,

Pujiarti, H., Arsyad, W. S., Shobih, Muliani, L., & Hidayat, R. (2018). Efficient and Stable Photovoltaic Characteristics of Quasi-Solid State DSSC using Polymer Gel Electrolyte Based on Ionic Liquid in Organosiloxane Polymer Gels. *Journal of Physics: Conference Series*, *1011*, 012020.

Purkait, P., Bhattacharyya, A., Roy, S., Maitra, S., Das, G., & Ghosh Chaudhuri, M. (2020). Green synthesis of TiO2 nanoparticle: its characterization and potential application in Zoxamide photodegradation. *Journal of Water and Environmental Nanotechnology*, *5*(3), 191-203.

Raguram, T., & Rajni, K. (2019). Synthesis and analysing the structural, optical, morphological, photocatalytic and magnetic properties of TiO_2 and doped (Ni and Cu) TiO2 nanoparticles by sol–gel technique. *Applied Physics A*, *125*, 1-11.

Rahman, S., Haleem, A., Siddiq, M., Hussain, M. K., Qamar, S., Hameed, S., & Waris, M. (2023). Research on dye sensitized solar cells: recent advancement toward the

various constituents of dye sensitized solar cells for efficiency enhancement and future prospects. *RSC advances*, *13*(28), 19508-19529.

Rahmani, S., Zeynizadeh, B., & Karami, S. (2020). Removal of cationic methylene blue dye using magnetic and anionic-cationic modified montmorillonite: kinetic, isotherm and thermodynamic studies. *Applied Clay Science*, *184*, 105391.

Raizada, P., Soni, V., Kumar, A., Singh, P., Khan, A. A. P., Asiri, A. M.,…Nguyen, V.-H. (2021). Surface defect engineering of metal oxides photocatalyst for energy application and water treatment. *Journal of Materiomics*, *7*(2), 388-418.

Raizada, P., Sudhaik, A., Patial, S., Hasija, V., Khan, A. A. P., Singh, P., & Nguyen, V.-H. (2020). Engineering nanostructures of CuO-based photocatalysts for water treatment: current progress and future challenges. *Arabian Journal of Chemistry*, *13*(11), 8424-8457.

Ramakrishnan, A., Neubert, S., Mei, B., Strunk, J., Wang, L., Bledowski, M., & Beranek, R. (2012). Enhanced performance of surface-modified TiO_2 photocatalysts prepared via a visible-light photosynthetic route. *Chemical Communications*, *48*(68), 8556-8558.

Ramanathan, R., Zinigrad, M., Kasinathan, D., & Poobalan, R. K. (2022). Zinc stannate (Zn_2SnO_4)-based hybrid composite photoanode for dye-sensitized solar cell application. *ACS Applied Energy Materials*, *5*(9), 11506-11516.

Ramírez, S., Wang, J., Valenzuela, M., Chen, L., & Dalai, A. (2020). CuO@ TiO_2 and NiO@ TiO_2 core-shell catalysts for hydrogen production from the photocatalytic reforming of glycerol aqueous solution. *Journal of applied research and technology*, *18*(6), 390-409.

Rani, N., Singh, P., Kumar, S., Kumar, P., Bhankar, V., & Kumar, K. (2023). Plant-mediated synthesis of nanoparticles and their applications: A review. *Materials Research Bulletin*, *163*, 112233.

Rao, M., Ravindranadh, K., & Shekhawat, M. (2016). Structural and electrical properties of TiO2 thin films. AIP Conference Proceedings,

Rehman, Z. U., Bilal, M., Hou, J., Butt, F. K., Ahmad, J., Ali, S., & Hussain, A. (2022). Photocatalytic CO2 reduction using TiO2-based photocatalysts and TiO2 z-scheme heterojunction composites: A review. *Molecules*, *27*(7), 2069.

Reza, K. M., Kurny, A., & Gulshan, F. (2017). Parameters affecting the photocatalytic degradation of dyes using TiO 2: a review. *Applied Water Science*, *7*, 1569-1578.

Rezaei, M., Mengelizadeh, N., Berizi, Z., Salehnia, S., Asgari, M., & Balarak, D. (2023). Synthesis of MMT− $CuFe_2O_4$ Composite as a Peroxymonosulfate Activator for the Degradation of Reactive Black 5. *ChemistrySelect*, *8*(2), e202201729.

Robledo, A. F., Enríquez, J. P., Avendaño, C. M., Hernández, G. P., & Gutiérrez, P. J. (2023). Characterization of natural dyes on ZnO and TiO2 thin films for applications in DSSC. *Journal of Materials Science: Materials in Electronics*, *34*(11), 980.

Rostami, M., Badiei, A., Ganjali, M. R., Rahimi-Nasrabadi, M., Naddafi, M., & Karimi-Maleh, H. (2022). Nano-architectural design of TiO_2 for high performance photocatalytic degradation of organic pollutant: A review. *Environmental Research*, *212*, 113347.

Roy, J. (2022). The synthesis and applications of TiO2 nanoparticles derived from phytochemical sources. *Journal of Industrial and Engineering Chemistry*, *106*, 1-19.

Rudrapal, M., Khairnar, S. J., Khan, J., Dukhyil, A. B., Ansari, M. A., Alomary, M. N.,…Devi, R. (2022). Dietary polyphenols and their role in oxidative stress-induced human diseases: Insights into protective effects, antioxidant potentials and mechanism (s) of action. *Frontiers in pharmacology*, *13*, 806470.

Rusman, E., Heryanto, H., Nurul Fahri, A., Tahir, D., & Mutmainna, I. (2021). Green Synthesis ZnO/TiO_2 for High Recyclability Rapid Sunlight Photodegradation Textile Dyes Applications. In: ResearchSquare.

Sacco, A. (2017). Electrochemical impedance spectroscopy: Fundamentals and application in dye-sensitized solar cells. *Renewable and Sustainable Energy Reviews*, *79*, 814-829.

Saha, K., Proma, R. Z., & Khan, N. (2020). Phytochemical screening of plant extracts and GC-MS analysis of n-hexane extract of the leaves of Cassia alata Linn. *The Journal of Phytopharmacology*, *9*(5), 342-347.

Sahai, A., & Goswami, N. (2015). Structural and optical investigations of oxygen defects in zinc oxide nanoparticles. AIP Conference Proceedings,

Saharudin, K. A., Sreekantan, S., Basiron, N., Khor, Y. L., Harun, N. H., SMN Mydin, R. B.,…Vignesh, K. (2018). Bacteriostatic Activity of LLDPE Nanocomposite Embedded with Sol–Gel Synthesized TiO2/ZnO Coupled Oxides at Various Ratios. *Polymers*, *10*(8), 878.

Sahoo, S., Wickramathilaka, K. Y., Njeri, E., Silva, D., & Suib, S. L. (2024). A review on transition metal oxides in catalysis. *Frontiers in chemistry*, *12*, 1374878.

Sakib, A. A. M., Masum, S. M., Hoinkis, J., Islam, R., & Molla, M. A. I. (2019). Synthesis of CuO/ZnO nanocomposites and their application in photodegradation of toxic textile dye. *Journal of Composites Science*, *3*(3), 91.

Saleh, T. A. (2020). Nanomaterials: Classification, properties, and environmental toxicities. *Environmental Technology & Innovation*, 101067.

Salem, B. B., Essalah, G., Ameur, S. B., Duponchel, B., Guermazi, H., Guermazi, S., & Leroy, G. (2023). Synthesis and comparative study of the structural and optical properties of binary ZnO-based composites for environmental applications. *RSC advances*, *13*(9), 6287-6303.

Salesi, S., & Nezamzadeh-Ejhieh, A. (2023). An experimental design study of photocatalytic activity of the Z-scheme silver iodide/tungstate binary nano photocatalyst. *Environmental Science and Pollution Research*, 1-17.

Salleh, M. A. M., Mahmoud, D. K., Karim, W. A. W. A., & Idris, A. (2011). Cationic and anionic dye adsorption by agricultural solid wastes: a comprehensive review. *Desalination*, *280*(1-3), 1-13.

Sayed, M. E., Ghouch, N. E., Younes, G., Noun, M., & Awad, R. (2024). Tailoring the Structural, Optical and Anti-corrosion Effect of Synthesized Sn-Doped CuO

Nanoparticles on Mild Steel in 0.5 M HCl Solution. *Journal of Materials Engineering and Performance*, 1-16.

Seleš, P., Vengust, D., Radošević, T., Kocijan, M., Einfalt, L., Kurtjak, M., & Omerzu, A. (2024). Altering defect population during the solvothermal growth of ZnO nanorods for photocatalytic applications. *Ceramics international*.

Sethy, N. K., Arif, Z., Mishra, P. K., & Kumar, P. (2020). Green synthesis of TiO_2 nanoparticles from Syzygium cumini extract for photo-catalytic removal of lead (Pb) in explosive industrial wastewater. *Green Processing and Synthesis*, *9*(1), 171-181.

Shabna, S., Dhas, S. S. J., & Biju, C. (2023). Potential progress in SnO_2 nanostructures for enhancing photocatalytic degradation of organic pollutants. *Catalysis Communications*, 106642.

Shah, S., Baharun, N., Yusuf, S., & Arof, A. (2019). Efficiency enhancement of dye-sensitized solar cells (DSSCs) using copper nanopowder (CuNW) in TiO_2 as photoanode. IOP Conference Series: Materials Science and Engineering,

Shah, T. K., Kumar, A., Tandel, R., Bhat, R. A. H., & Sarma, D. (2019). Identification of functional groups in Thymus linearis ethanol leaf extract through fourier transform infrared spectroscopy (FTIR). *J Pharmocognosy Phyochemistr*, *8*(4), 3013-3015.

Shaikh, J. S., Shaikh, N. S., Mali, S. S., Patil, J. V., Pawar, K. K., Kanjanaboos, P., & Patil, P. S. (2018). Nanoarchitectures in dye-sensitized solar cells: metal oxides, oxide perovskites and carbon-based materials. *Nanoscale*, *10*(11), 4987-5034.

Shalini, S., Balasundaraprabhu, R., Kumar, T. S., Prabavathy, N., Senthilarasu, S., & Prasanna, S. (2016). Status and outlook of sensitizers/dyes used in dye sensitized solar cells (DSSC): a review. *International journal of energy research*, *40*(10), 1303-1320.

Shalini, S., Kumar, T. S., Prasanna, S., & Balasundaraprabhu, R. (2020). Investigations on the effect of co-doping in enhancing the performance of nanostructured TiO_2 based DSSC sensitized using extracts of Hibiscus Sabdariffa calyx. *Optik*, *212*, 164672.

Sharma, G., Poudel, P., Thapa, R., Lamichhane, S., Poudel, H. R., Devkota, H. P., & Ur Rahman, I. (2021). Rumex nepalensis Spreng. Rumex hastatus D. Don Rumex longifolius DC. Polygonaceae. In *Ethnobotany of the Himalayas* (pp. 1-19). Springer.

Sharma, K., Sharma, V., & Sharma, S. (2018). Dye-sensitized solar cells: fundamentals and current status. *Nanoscale research letters*, *13*(1), 1-46.

Sharma, S., Jain, K. K., & Sharma, A. (2015). Solar cells: in research and applications—a review. *Materials Sciences and Applications*, *6*(12), 1145.

Shawky, A. M., Elshypany, R., El Sharkawy, H. M., Mubarak, M. F., & Selim, H. (2024). Emerald eco-synthesis: harnessing oleander for green silver nanoparticle production and advancing photocatalytic MB degradation with TiO_2&CuO nanocomposite. *Scientific Reports*, *14*(1), 2456.

Shen, K., Wu, K., & Wang, D. (2014). Band alignment of ultra-thin hetero-structure ZnO/TiO2 junction. *Materials Research Bulletin*, *51*, 141-144.

Shewasinad, A., Bhoumik, D., ZERO HISHE, H., & Masresha, B. (2018). Antidiabetic activity of methanol extract and fractions of Thymus schimperi ronniger leaves in normal and streptozotocin induce diabetic mice. *Iranian Journal of Pharmacology and Therapeutics*, *16*(1), 1-8.

Shi, L.-Y., Chen, T.-L., Chen, C.-H., & Cho, K.-C. (2013). Synthesis and characterization of a gel-type electrolyte with ionic liquid added for dye-sensitized solar cells. *International Journal of Photoenergy*, *2013*.

Shimi, A. K., Ahmed, H. M., Wahab, M., Katheria, S., Wabaidur, S. M., Eldesoky, G. E.,…Rane, K. P. (2022). Synthesis and applications of green synthesized TiO_2 nanoparticles for photocatalytic dye degradation and antibacterial activity. *Journal of Nanomaterials*, *2022*.

Shoshaa, R., Ashfaq, M. Y., & Al-Ghouti, M. A. (2023). Recent developments in ultrafiltration membrane technology for the removal of potentially toxic elements, and enhanced antifouling performance: A review. *Environmental Technology & Innovation*, 103162.

Singh, J., Dutta, T., Kim, K.-H., Rawat, M., Samddar, P., & Kumar, P. (2018). 'Green'synthesis of metals and their oxide nanoparticles: applications for environmental remediation. *Journal of Nanobiotechnology*, *16*(1), 1-24.

Sofyan, N., Ridhova, A., Yuwono, A. H., & Udhiarto, A. (2017). Fabrication of solar cells with TiO2 nanoparticles sensitized using natural dye extracted from mangosteen pericarps. *International Journal of Technology*, *8*(7), 1229-1238.

Solano, R., Maestre, D., Mueses, M., & Herrera, A. (2023). TiO_2-CuO heterojunction nanoparticles synthesized by green chemistry supported on beach sand granules: optical, morphological and structural characterization. *Nano-Structures & Nano-Objects*, *35*, 101024.

Solano, R., Mallarino, L., Mueses, M., & Herrera, A. (2024). Photocatalytic degradation of metformin using TiO_2-CuO heterojunctions synthesized by green chemistry and immobilized on beach sand granules in fluidized bed annular photoreactor (FBAP). *Journal of environmental chemical engineering*, *12*(5), 113576.

Solymos, K., Babcsányi, I., Ariya, B., Gyulavári, T., Ágoston, Á., Szamosvölgyi, Á.,…Pap, Z. (2024). Photocatalytic and surface properties of titanium dioxide nanoparticles in soil solutions. *Environmental Science: Nano*.

Song, Y., Mendes, P. C., & Kozlov, S. M. (2023). Tunable properties and composition of ZnO films supported on metal surfaces. *Journal of Materials Chemistry A*, *11*(25), 13665-13676.

Sowmya, S., Ruba, N., Inbarajan, K., Prakash, P., & Janarthanan, B. (2021). Dye-sensitized solar cells concocted with dyes extracted from fresh and dried leaves of Henna using different solvents. *Optical and Quantum Electronics*, *53*(5), 274.

Srivastava, R. (2012). Synthesis and characterization techniques of nanomaterials. *International Journal of Green Nanotechnology*, *4*(1), 17-27.

Su'ait, M. S., Rahman, M. Y. A., & Ahmad, A. (2015). Review on polymer electrolyte in dye-sensitized solar cells (DSSCs). *Solar Energy*, *115*, 452-470. https://doi.org/10.1016/j.solener.2015.02.043

Subodro, R., Kristiawan, B., Ramelan, A. H., Wahyuningsih, S., Munawaroh, H., Hanif, Q. A., & Saputri, L. N. M. Z. (2017). Dye-Sensitized Solar Cells (DSSCs) reengineering using TiO2 with natural dye (anthocyanin). AIP Conference Proceedings,

Suhaimi, S., Shahimin, M. M., Alahmed, Z., Chyský, J., & Reshak, A. (2015). Materials for enhanced dye-sensitized solar cell performance: Electrochemical application. *Int. J. Electrochem. Sci*, *10*(4), 2859-2871.

Sullivan, H., Wang, B., & Jiang, L. (2022). Investigation of tropical plant-based natural dyes combination and adsorption optimization for natural dye-sensitized solar cell. *Environmental Progress & Sustainable Energy*, *41*(4), e13809.

Sun, G., Tai, Z., Li, F., Ye, Q., Wang, T., Fang, Z., & Wang, H. (2023). Construction of ZnIn2S4/CdS/PdS S-scheme heterostructure for efficient photocatalytic H2 production. *Small*, *19*(27), 2207758.

Sun, Y., Zhang, W., Li, Q., Liu, H., & Wang, X. (2023). Preparations and applications of zinc oxide based photocatalytic materials. *Advanced Sensor and Energy Materials*, 100069.

Sunaryono, S., Halizah, S. N., Zulaikah, S., Susanto, H., Mufti, N., & Taufiq, A. (2021). Contribution of ZnO/TiO_2 nanocomposite particles towards bacterial growth inhibition. AIP conference Proceedings,

Sundaram, M., Kalpana, S., Sivaganesan, V., & Nandhakumar, E. (2019). Studies on the catalytic activity of $CuO/TiO_2/ZnO$ ternary nanocomposites prepared via one step hydrothermal green approach. *Materials Research Express*, *6*(12), 125043.

Suresh, R., Gnanasekaran, L., Rajendran, S., Soto-Moscoso, M., Chen, W.-H., Show, P. L., & Khoo, K. S. (2023). Application of nanocomposites in integrated photocatalytic techniques for water pollution remediation. *Environmental Technology & Innovation*, *31*, 103149.

Susanti, D., Nafi, M., Purwaningsih, H., Fajarin, R., & Kusuma, G. E. (2014). The Preparation of Dye Sensitized Solar Cell (DSSC) from TiO2 and Tamarillo Extract. *Procedia Chemistry*, *9*, 3-10.

Tadesse, S. (2019). Photovoltaic performance of dye-sensitized solar cell based on eosin-Y photosensitizer and quasi-solid state electrolyte. *Ethiopian Journal of Science and Technology*, *12*(1), 93-105.

Tadesse, S., Abebe, A., Chebude, Y., Garcia, I. V., & Yohannes, T. (2012). Natural dye-sensitized solar cells using pigments extracted from Syzygium guineense. *Journal of Photonics for Energy*, *2*(1), 027001-027001.

Tahir, D., Satriani, W., Gareso, P., & Abdullah, B. (2018). Dye sensitized solar cell (DSSC) with natural dyes extracted from Jatropha leaves and purple Chrysanthemum flowers as sensitizer. Journal of Physics: Conference Series,

Tahir, M. B., Sohaib, M., Sagir, M., & Rafique, M. (2022). Role of nanotechnology in photocatalysis. *Encyclopedia of smart materials*, 578.

Taniguchi, M., LaRocca, C. A., Bernat, J. D., & Lindsey, J. S. (2023). Digital database of absorption spectra of diverse flavonoids enables structural comparisons and quantitative evaluations. *Journal of Natural Products*, *86*(4), 1087-1119.

Taya, S. A., El-Agez, T. M., Elrefi, K. S., & Abdel-Latif, M. S. (2015). Dye-sensitized solar cells based on dyes extracted from dried plant leaves. *Turkish Journal of Physics*, *39*(1), 24-30.

Thamaphat, K., Limsuwan, P., & Ngotawornchai, B. (2008). Phase characterization of TiO_2 powder by XRD and TEM. *Agriculture and Natural Resources*, *42*(5), 357-361.

Thomas, M. R. N., Lourdusamy, V. J. K., Dhandayuthapani, A. A., & Jayakumar, V. (2021). Non-metallic organic dyes as photosensitizers for dye-sensitized solar cells: a review. *Environmental Science and Pollution Research*, 1-15.

Thomas, S., Deepak, T., Anjusree, G., Arun, T., Nair, S. V., & Nair, A. S. (2014). A review on counter electrode materials in dye-sensitized solar cells. *Journal of Materials Chemistry A*, *2*(13), 4474-4490.

Tian, J., Hu, X., Wei, N., Zhou, Y., Xu, X., Cui, H., & Liu, H. (2016). RuO2/TiO2 nanobelt heterostructures with enhanced photocatalytic activity and gas-phase selective oxidation of benzyl alcohol. *Solar Energy Materials and Solar Cells*, *151*, 7-13.

Tomar, N., Agrawal, A., Dhaka, V. S., & Surolia, P. K. (2020). Ruthenium complexes based dye sensitized solar cells: Fundamentals and research trends. *Solar Energy*, *207*, 59-76.

Toncón-Leal, C. F., Villarroel-Rocha, J., Silva, M. T. P. d., Braga, T. P., & Sapag, K. (2021). Characterization of mesoporous region by the scanning of the hysteresis loop in adsorption–desorption isotherms. *Adsorption*, *27*(7), 1109-1122.

Topoglidis, E. (2020). Mesoporous Metal Oxide Films. In: Multidisciplinary Digital Publishing Institute.

Trihutomo, P., Soeparman, S., Widhiyanuriyawan, D., & Yuliati, L. (2019). Performance improvement of dye-sensitized solar cell-(DSSC-) based natural dyes by clathrin protein. *International Journal of Photoenergy*, *2019*.

Tripathi, N. (2013). Cationic and anionic dye adsorption by agricultural solid wastes: A comprehensive review. *Journal of Applied Chemistry*, *5*(9995335), 108.

Valenzano, L., Civalleri, B., Chavan, S., Palomino, G. T., Areán, C. O., & Bordiga, S. (2010). Computational and Experimental Studies on the Adsorption of CO, N2, and CO2 on Mg-MOF-74. *The Journal of Physical Chemistry C*, *114*(25), 11185-11191.

Velázquez-Martínez, S., Silva-Martínez, S., Jiménez-González, A., & Maldonado Álvarez, A. (2019). Synthesis of Mesoporous TiO2 Spheres via the Solvothermal Process and Its Application in the Development of DSSC. *Advances in Materials Science and Engineering*, *2019*.

Venkatesan, S., & Lee, Y.-L. (2017). Nanofillers in the electrolytes of dye-sensitized solar cells–A short review. *Coordination Chemistry Reviews*, *353*, 58-112.

Verma, V., Al-Dossari, M., Singh, J., Rawat, M., Kordy, M. G., & Shaban, M. (2022). A review on green synthesis of TiO2 NPs: photocatalysis and antimicrobial applications. *Polymers*, *14*(7), 1444.

Wach, A., Zou, X., Wojtaszek, K., Kayser, Y., Garlisi, C., Palmisano, G.,…Szlachetko, J. (2023). Towards understanding the TiO2 doping at the surface and bulk. *X-Ray Spectrometry*, *52*(5), 261-268.

Wei, Q., Wang, Y., Qin, H., Wu, J., Lu, Y., Chi, H.,…Liu, J. (2018). Construction of rGO wrapping octahedral Ag-Cu_2O heterostructure for enhanced visible light photocatalytic activity. *Applied Catalysis B: Environmental*, *227*, 132-144.

Wittkamp, B. L., Hawthorne, S. B., & Tilotta, D. C. (1997). Determination of aromatic compounds in water by solid phase microextraction and ultraviolet absorption spectroscopy. 1. Methodology. *Analytical Chemistry*, *69*(6), 1197-1203.

Wongsa, P., Phatikulrungsun, P., & Prathumthong, S. (2022). FT-IR characteristics, phenolic profiles and inhibitory potential against digestive enzymes of 25 herbal infusions. Sci Rep 12: 6631. In.

Wu, J., Lan, Z., Hao, S., Li, P., Lin, J., Huang, M., & Huang, Y. (2008). Progress on the electrolytes for dye-sensitized solar cells. *Pure and Applied Chemistry*, *80*(11), 2241-2258.

Wu, J., Lan, Z., Lin, J., Huang, M., Huang, Y., Fan, L., & Luo, G. (2015). Electrolytes in dye-sensitized solar cells. *Chemical reviews*, *115*(5), 2136-2173.

Wu, X. (2021). Applications of titanium dioxide materials. *Titanium Dioxide—Advances and Applications*.

Wypych, A., Bobowska, I., Tracz, M., Opasinska, A., Kadlubowski, S., Krzywania-Kaliszewska, A.,…Wojciechowski, P. (2014). Dielectric properties and characterisation of titanium dioxide obtained by different chemistry methods. *Journal of Nanomaterials*, *2014*, 1-9.

Yan, X., Zou, C., Gao, X., & Gao, W. (2012). ZnO/TiO_2 core–brush nanostructure: processing, microstructure and enhanced photocatalytic activity. *Journal of Materials Chemistry*, *22*(12), 5629-5640.

Yang, H., Yang, B., Chen, W., & Yang, J. (2022). Preparation and photocatalytic activities of TiO2-based composite catalysts. *Catalysts*, *12*(10), 1263.

Yaqoob, A. A., Ahmad, H., Parveen, T., Ahmad, A., Oves, M., Ismail, I. M., & Mohamad Ibrahim, M. N. (2020). Recent advances in metal decorated nanomaterials and their various biological applications: a review. *Frontiers in chemistry*, *8*, 341.

Yikna, B. B., & Yehualashet, A. S. (2021). Medicinal plant extracts evaluated in vitro and in vivo for antidiabetic activities in Ethiopia: Bases for future clinical trials and related investigations. *Evidence-Based Complementary and Alternative Medicine*, *2021*.

YILDIRIM, N., Serin, T., & Serin, N. (2010). Investigation of a p-CuO/n-TiO_2 thin film heterojunction fabricated by the sol-gel process. *Journal of Optoelectronics and Advanced Materials*, *12*(May 2010), 1153-1156.

Yildiz, A., Yurduguzel, B., Kayhan, B., Calin, G., Dobromir, M., & Iacomi, F. (2012). Electrical conduction properties of Co-doped ZnO nanocrystalline thin films. *Journal of Materials Science: Materials in Electronics*, *23*, 425-430.

Yohannis, S. W., Asfaw, Z., & Kelbessa, E. (2018). Ethnobotanical study of medicinal plants used by local people in menz gera midir district, north shewa zone, amhara regional state, Ethiopia. *Journal of Medicinal Plants Research*, *12*(21), 296-314.

Zatirostami, A. (2020). Increasing the efficiency of TiO2-based DSSC by means of a double layer RF-sputtered thin film blocking layer. *Optik*, *207*, 164419. https://doi.org/10.1016/j.ijleo.2020.164419

Zhang, F., Wang, X., Liu, H., Liu, C., Wan, Y., Long, Y., & Cai, Z. (2019). Recent advances and applications of semiconductor photocatalytic technology. *Applied Sciences*, *9*(12), 2489.

Zhang, P., Chu, F., Zhou, M., Tao, B., & Miao, F. (2024). DSSC using natural dye sensitized and Ag/CdS/TiO2 composite structured light anode. *Vacuum*, *219*, 112763.

Zhang, Q., & Li, C. (2019). TiO_2 coated ZnO nanorods by mist chemical vapor deposition for application as photoanodes for dye-sensitized solar cells. *Nanomaterials*, *9*(9), 1339.

Zhang, W., Hu, X., Wang, L., & Wang, X. (2014). Reconstruction of the carotenoid biosynthetic pathway of Cronobacter sakazakii BAA894 in Escherichia coli. *PLoS One*, *9*(1), e86739.

Zhang, W., Tian, Y., He, H., Xu, L., Li, W., & Zhao, D. (2020). Recent advances in the synthesis of hierarchically mesoporous TiO2 materials for energy and environmental applications. *National Science Review*, *7*(11), 1702-1725.

Zhang, X.-x., Xiao, Y.-g., Cao, S.-s., Yin, Z.-l., & Liu, Z.-Q. (2022). Ternary TiO2@ Bi2O3@ TiO2 hollow photocatalyst drives robust visible-light photocatalytic performance and excellent recyclability. *Journal of Cleaner Production*, *352*, 131560.

Zhao, L., Cui, T., Li, Y., Wang, B., Han, J., Han, L., & Liu, Z. (2015). Efficient visible light photocatalytic activity of p–n junction CuO/TiO 2 loaded on natural zeolite. *RSC advances*, *5*(79), 64495-64502.

Zhu, K., Neale, N. R., Miedaner, A., & Frank, A. J. (2007). Enhanced charge-collection efficiencies and light scattering in dye-sensitized solar cells using oriented TiO2 nanotubes arrays. *Nano letters*, *7*(1), 69-74.

Zhu, X., Han, S., Feng, W., Kong, Q., Dong, Z., Wang, C.,…Yi, Q. (2018). The effect of heat treatment on the anatase–rutile phase transformation and photocatalytic activity of Sn-doped TiO 2 nanomaterials. *RSC advances*, *8*(26), 14249-14257.

Zyoud, A., Zyoud, A. H., Zyoud, S. H., Nassar, H., Zyoud, S. H., Qamhieh, N.,…Hilal, H. S. (2023). Photocatalytic degradation of aqueous methylene blue using ca-alginate supported ZnO nanoparticles: point of zero charge role in adsorption and photodegradation. *Environmental Science and Pollution Research*, *30*(26), 68435-68449.